MULTIDIRECTIONAL BEAM SCANNING OF A CIRCULAR WAVEGUIDE ANTENNA LOADED WITH MAGNETIC MATERIAL

BY

ABDULLAH MOHAMMED ALGARNI

A Thesis Presented to the
DEANSHIP OF GRADUATE STUDIES

KING FAHD UNIVERSITY OF PETROLEUM & MINERALS

DHAHRAN, SAUDI ARABIA

In Partial Fulfillment of the
Requirements for the Degree of

MASTER OF SCIENCE

In

ELECTRICAL ENGINEERING

May 2014

KING FAHD UNIVERSITY OF PETROLEUM & MINERALS
DHAHRAN- 31261, SAUDI ARABIA

DEANSHIP OF GRADUATE STUDIES

This thesis, written by **Abdullah Mohammed AlGarni** under the direction his thesis advisor and approved by his thesis committee, has been presented and accepted by the Dean of Graduate Studies, in partial fulfillment of the requirements for the degree of **MASTER OF SCIENCE IN ELECTRICAL ENGINEERING.**

Sheikh Sharif

Dr. SHEIKH, SHARIF I.
(Advisor)

Dr. ALI AHMAD AL-SHAIKHI
Department Chairman

H.A. Rag

Dr. RAGHEB, HASSAN A.
(Member)

Dr. Salam A. Zummo
Dean of Graduate Studies

Essam

Dr. HASSAN, ESSAM E.M.
(Member)

21/5/14

Date

Dedicated to my family

ACKNOWLEDGMENTS

At the beginning, all praises to ALLAH for helping and guiding me all through the life.

I would like to acknowledge a few people those have supported and helped me to achieve my goal. I would like to thank Dr. Sheikh Sharif Iqbal for his time, guidance and support given to me. Also, I would like to thank Dr. Hassan Ragheb for helping me to complete the theoretical part of my thesis. I would also like to thank my committee member Dr. Essam Hassan whose experiences immensely helped me tocomplete the thesis. Also, I would like to thank Dr. Ali Al-Shaikhi whogave a great help and guidance to complete the project, especially in the fabrication part.

I would also thank my family; my father, my mother, my brothers, my sister, my wife and my relatives for allsupports, assistancesand for their sincerepraying to complete my study.

At the end I would like to thank the lab engineers Mr. Khaled and Mr. Abbas from power group, andMr. Jose and Mr. Irfanfrom electromagnetic groupfor their great help in the lab.

Table of Contents

LIST OF TABLES

LIST OF FIGURES

THESIS ABSTRACT

NAME: Abdullah Mohammed AlGarni

TITLE OF STUDY: Multidirectional Beam Scanning Of a Circular Waveguide Antenna Loaded with Magnetic Material

MAJOR FIELD: Electrical Engineering

DATE OF DEGREE: May 2014

Circular waveguides are widely used to construct high power multimode horns antennas. Although beam tilting of this class of antennas can be achieved by off-centered dielectric loading, this method fails to realize antenna beam scanning properties. Externally magnetized ferrites are popular in introducing progressive phase shifts required to scan the main beam of a phased array antenna. But printed array antennas are often limited by its power handling capability.

In thisthesis, the design of a simpler and effective scanning mechanism is presented byintegrating an axially magnetized ferrite cylinder in the core of a circular waveguide antenna. The interaction of the gyromagnetic properties of magnetized ferrites and the EM fields within the waveguide is used to realize multidirectional beam scanning. Mode charts of the ferrite cylinderarecalculated to avoid the lossyferromagneticresonance regions. Professional simulator software (HFSS) is used to analyze the modal behavior of the coaxially feed ferrite loaded circular waveguide antenna. The software model is initially verified by comparing the simulated mode charts with calculated cut-off numbers. The simulated model is optimized to achieve acceptable impedance matching and radiation properties. Based on the beam-width of the antenna, the broadside radiating plane is divided into eight regions. The range of external magnetizing field needed to scan the beam within aregion or between regions are tabulated. Maximum scan angle of 35° with acceptable radiation properties is observed for a change of external magnetizing field,H_0=380 KA/m (≅ 0.4 Tesla). Finally EBG superstrate is used to enhance the directivity of the antenna.

ملخص الرسالة

الاسم: عبدالله محمد القرني

عنوان الأطروحة: شعاع ضوئي متعدد الاتجاهات باستخدام دليل موجي دائري هوائي محمول بمادة مغناطيسية

التخصص: هندسة كهربائية

تاريخ الحصول على الدرجة: مايو 2014

يسستخدم الدليل الموجي الدائري على نطاق واسع لبناء أبواق هوائية ذات طاقة عالية. على الرغم من أن الاشعاع الخاص بهذا النوع من الهوائيات يمكن تحقيقه بواسطة وضع العازل في غير محورها فقد فشلت هذه الطريقة في تحقييق خصائص المسح الضوئي للهوائي. طبقة الفريت الممغنطة خارجيا تحضى بشعبية في إدخال مرحلة التحولات التدريجية المطلوبة لمسح الشعاع الرئيسي للمصفوفه على مراحل. ولكن الهوائيات المطبوعة محدودة الطاقة.

في هذه الأطروحة ، يتم تقديم تصميم آلية أبسط وفعالة للمسح الضوئي من خلال دمج اسطوانة الفريت الممغنطة محوريا في قلب الدليل الموجي الهوائي. تفاعل الخصائص الدوارنية المغناطيسية للفريت الممغنط مع الحقول الكهرومغناطيسية لحقيق مسح شعاعي متعدد الاتجاهات. ايجاد الرسم البياني للأوضاع الفعالة لاسطوانة الفريت لتقادي العمل في المناطق الرنين الضعيفة.برنامج محاكاة محترف (محاكاة هيكل التردد العالي) يستخدم لتحليل سلوك شكل الدليل الموجي الهوائي المحملة مع الفريت المغذاة محوريا. يتم التحقق مننموذج البرمجياتفي البدايةمن خلال مقارنةوضعالمخططاتمحاكاةمعاحتسابالأرقاموقف انتاج المواد الانشطارية. تصميم النموذج المحاكا لتحقيق مقاومة مطابقة وخصائص الإشعاع الامثل. استنادا إلى العرض الشعاعي للهوائي ، يتم تقسيم مستوى الاشعاع الى ثماني مناطق. النطاق الخارجي لمجال الجذب المستخدمة لمسح الشعاع داخل المنطفة أو بين المناطق مجدولة. بتغيير مجال الجذب الخارجي الى 380 كيلوأمبير/ متر، أقصى زاوية للمسح الضوئي وصلت الى 35 درجة مع خصائص الإشعاع المقبولة. أخيرا، استخدام استراتيجية فرقة الفجوة الكهرومغناطيسية لتعزيز اتجاهية الهوائي.

CHAPTER 1

INTRODUCTION

1.1 Introduction

In modern communication systems, the need for designing directive and easily controllable antennas are of ongoing interest [1-3]. High power microwave applications, such as radars and transmitter antennas, often require beam steering capabilities [4-8]. Electronic (phased array) and mechanical techniques are widely adopted to achieve beam steering, but often require completed array feeder circuits and relative slow and inflexibility mechanical control devises [9]. In addition most existing linear and planar phased array antennasare limited by mutual coupling and limited power handling capabilities [10]. Thus, the design of a simple beam steering antenna with efficient power handling mechanism is needed. This project aims at designing a simple ferrite loaded circular waveguide antenna for efficient multidirectional beam scanning.

Circular waveguides are widely used to construct high power multimode horns antennas [11]. In the literature, researchers have demonstrate gain and directivity of the circular waveguide antenna can be improved by loading dielectric [27] or electromagnetic band gap (EBG) [12] material. The radiation patterns are also investigated by authors, where beam squint is achieved by loading off-centered dielectric rod [13] and corrugated waveguides are used for reducing the side-lobes [4,5]. But, the investigators of this proposal did not find any reference that details an externally controllable beam-forming property of a single waveguide antenna.

Magnetized ferrites are also popular, longitudinally magnetized ferrite loaded circular waveguide and junctions are widely used in high power control devices, like rotary field phase shifters [14] and junction circulators [15]. They are also popular to introduce externally controlled beam steering properties of microstrip, waveguide and phased-array antennas [7-9]. Knowledge about the gyromagnetic properties of ferrites is essential in understanding its phase control properties. Closed form methods will be used to find the modal properties of the ideal ferrite cylinder to avoid operating in lossy resonance regions.

In this research work, a conducting circular waveguide will be centrally loaded with externally magnetized ferrite rod to introduce and beam steering capability. The cutoff numbers of a circular waveguide loaded with concentric ferrite cylinder are calculated to validate the meshing properties of the related software model. Professional software HFSS ("Appendix B") is used to model the designed coaxially feed ferrite loaded circular waveguide antenna. HFSS is a finite element solver with user defined geometry, boundary condition and material properties. It is used here to optimize the location, position and dimension of the coaxial input and the ferrite cylinder to produce multidirectional beam steering. Based on the beam-width of the antenna, the broadside radiating plane is divided into eight regions. The range of external magnetizing field needed to scan the beam within a region or between regions are tabulated. Maximum scan angle of 35° with acceptable radiation properties is observed for a change of external magnetizing field, H_0=380 KA/m ($\cong$ 0.48 Tesla). An experimental prototype of the designed antenna is fabricated to verify the antenna radiation patterns. To increase the directivity of the antenna, a EBG partial reflector is placed at some distance from the open end of the waveguide to from a cavity resonator. With optimum design, this resonator enhanced antenna directivity but at the cost of reduced scan angle.

1.2 Literature Review

High power multimode horn antennas are constructed using circular waveguides [11]. Researchers have shown thatdielectric loading can improve the gain and directivity of a waveguide antenna. **Figure 1.1** shows a circular waveguide antenna with a composite superstrate made of dielectric material and electromagnetic band gap (EBG) structures [12]. The directivity improvement is due to the formation of a cavity between the superstrate and reflective ground plane, which behaves like a Fabry-Perot cavity excited by the circular waveguide.

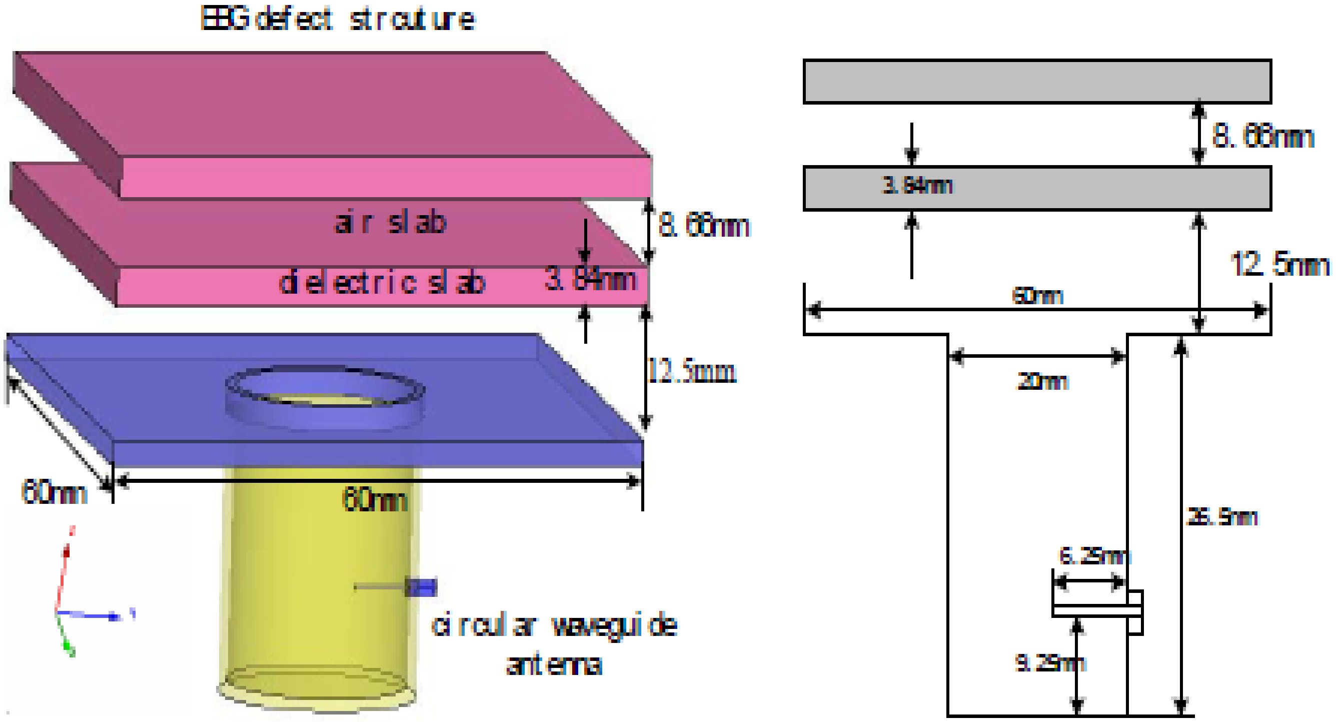

Figure 1.1: Circular waveguide antenna with EBG superstrate

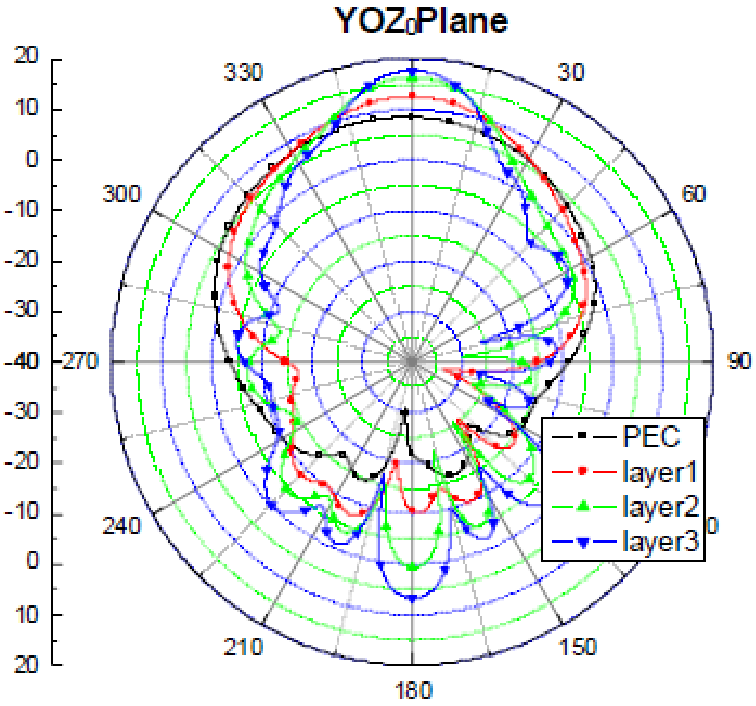

Figure 1.2: Directivity enhancement of the antenna due to EBG superstrate.

The authors of this reference [12] have reported that this method can increase the directivity of the antenna by 7dB. The radiation pattern and reflection property of the antenna is plotted in **Figure1.2**.

In literature [13], the beam steering mechanism of an off centrically loaded circular waveguide antenna is discussed. The designed waveguide is shown in **Figure 1.3**. The author of this paper derived the TE field distribution and the cutoff-chart of the waveguide to demonstrate the modal behavior of the antenna. The calculated radiation pattern of the antenna is shown in **Figure 1.4**, which demonstrates a beam squint of around 20 degrees.

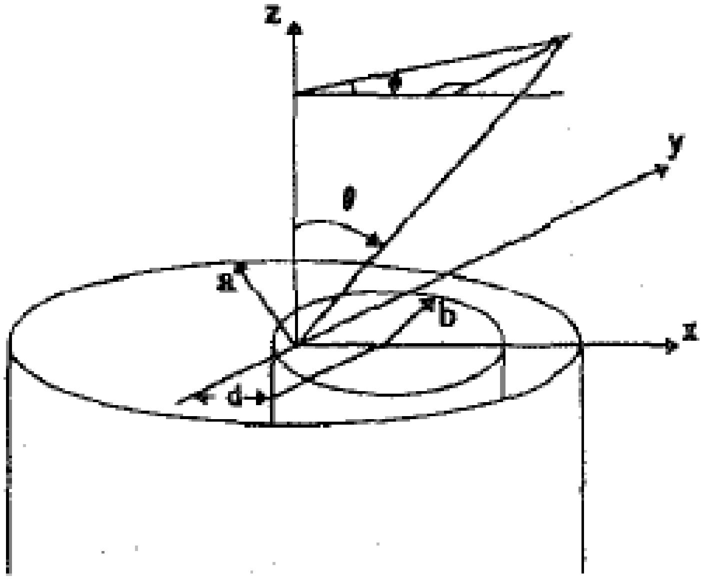

Figure 1.3: Circular waveguide antenna loaded with off-centered dielectric rod

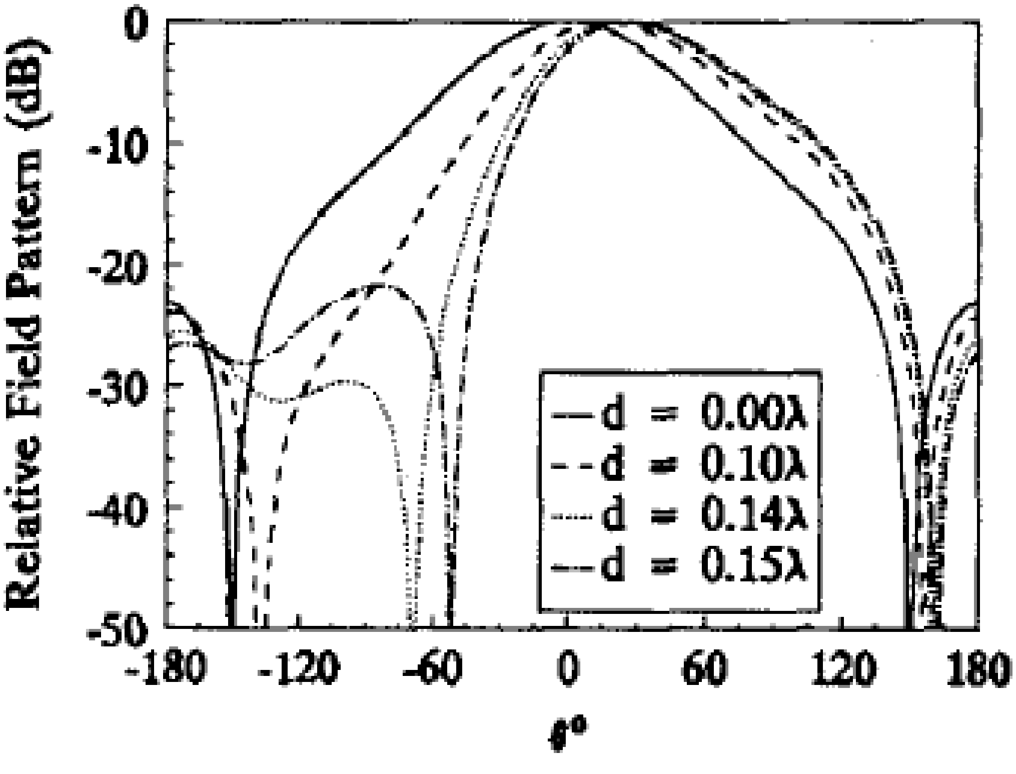

Figure 1.4 Beam squint of the antenna due to off-centered dielectric loading

In the literature, high impedance ground plane (HIGP) is a popular technique used to reduce the side-lobes of a circular waveguide antenna. **Figure 1.5** shows this class of antenna designed in reference [4,5, 6], where the substrate of the HIGP has a dialectic constant of 4.8 and the thickness of 1.5 mm. The size of the HIGP is 200mm x 200 mm with size of each element is 7 mm x 7 mm and the gap between the elements is 0.3 mm. The authors of this article demonstrated a side lobe reduction of 10 dB, as shown in **Figure 1.6**.

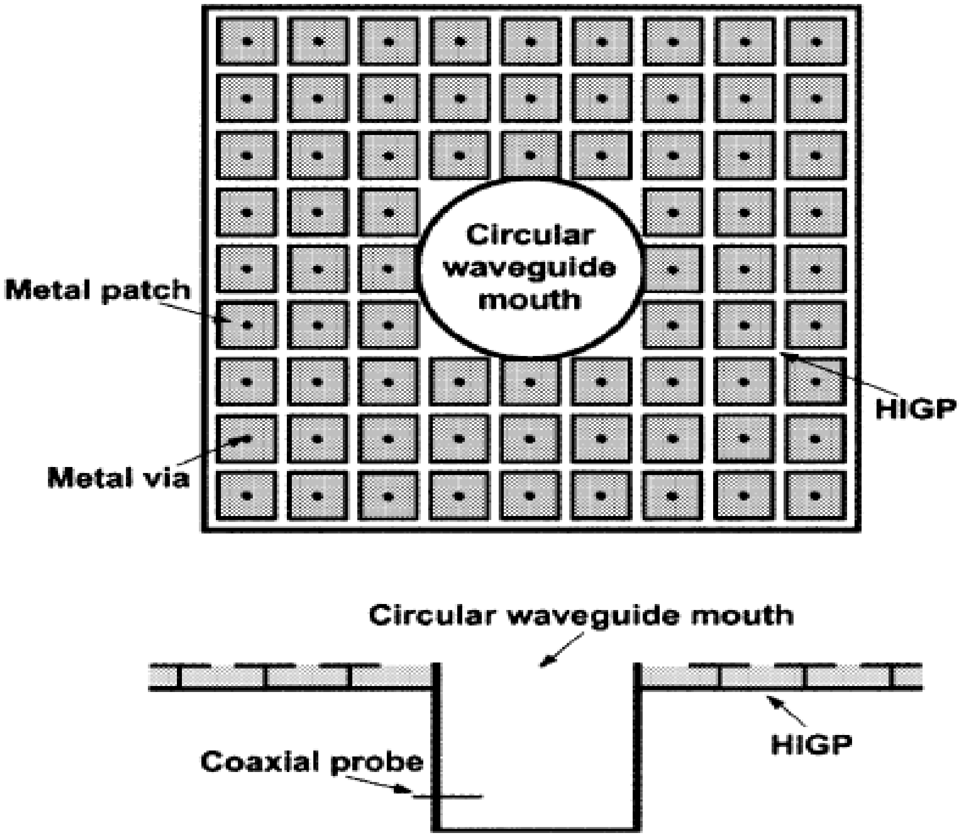

Figure 1.5: Circular waveguide antenna structure with high impedance ground plane.

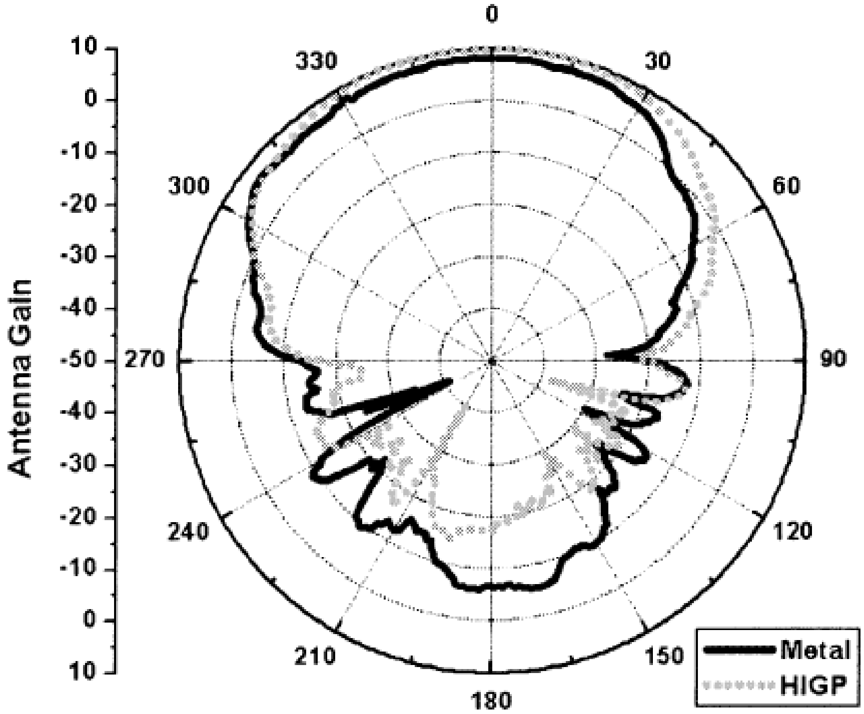

Figure 1.6: Side-lobe reduction due to introducing high impedance ground plane

In literature [25], the aperture efficiency and the cross polarization of a circular waveguide antenna is improved by dielectric loading. The designed waveguide wall with strip loaded dielectric coating is shown in **Figure 1.7**.Notes that the thickness of the dielectric material coating is “b – a”, where ‘b’ is the radius of the waveguide and ‘a’ is the radius of the empty central part. The inner surface of the dielectric is loaded with metal with zero thickness. The conductor is assumed to be perfectly conducting because of the spacing of the geometry is much smaller than the operating wavelength.In reference [26], meta-material superstrate is used to increase the gain of a circular waveguide array antenna **to 8.3 dB**, as shown in **Figure 1.8**, [26]. The meta-material superstrate consisted of zero thickness and size of 68.4 mm x 68.4 mm. The size of the each is cell 6.5 mm x 6.5 mm and the spacing between the cells is 0.55 mm. The reported spacing between the layers is 9.5 mm and each layer has 9 x 9 cells.

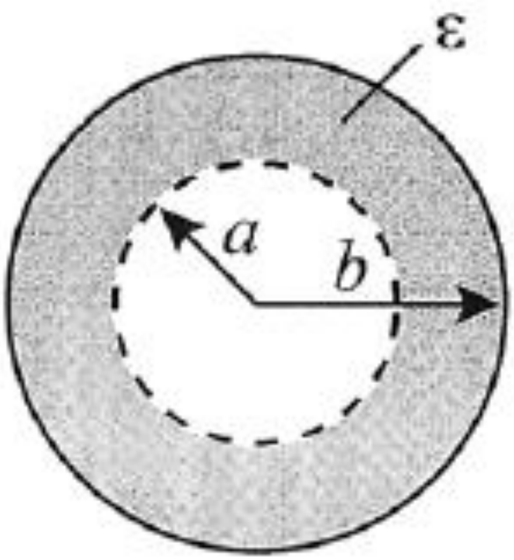

Figure 1.7: Circular waveguide with strip-loaded dielectric side wall[25]

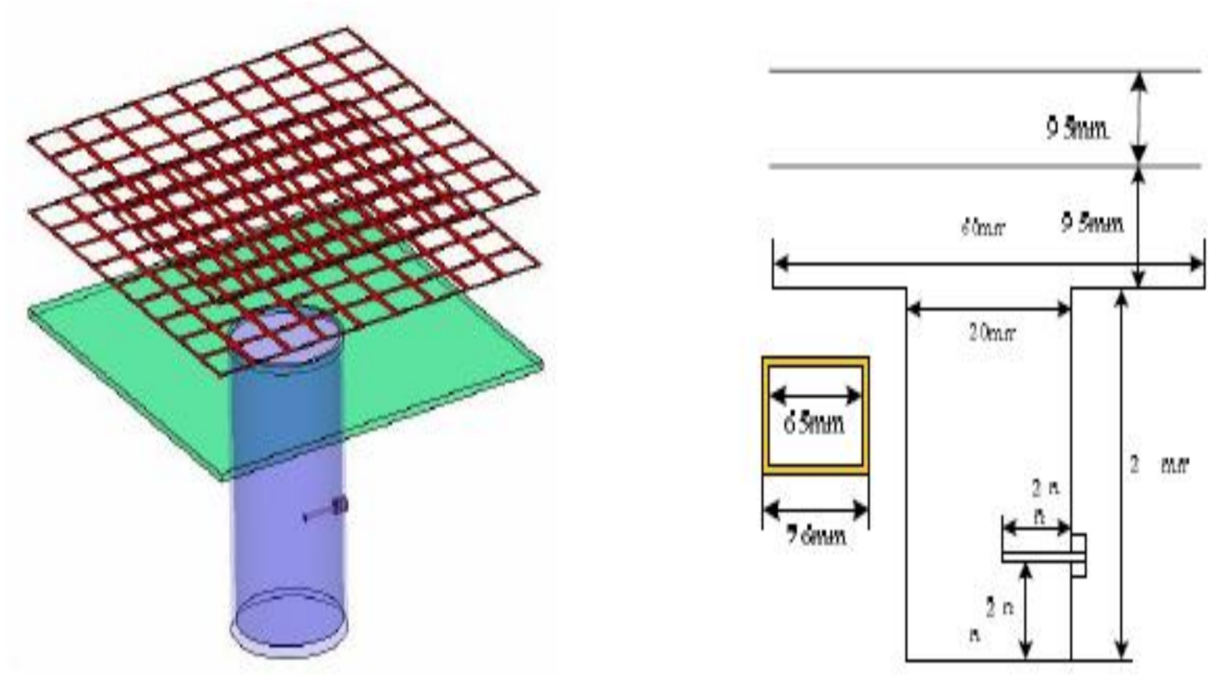

Figure 1.8: Gain enhancement of Circular waveguide antenna with meta-material superstrate

Although above techniques can be used to control and shape the radiation pattern of a loaded circular waveguide antenna, they lack the ability to scan the main beam in a continuous manner. In high power control devices, magnetized ferrite cylinders and disks are widely used to achievephase shifters [14,15].In a phased array antenna, phase shifters are essential to introduce beam scanning [7-9]. Externally magnetized ferrites substrate and superstrate are also popular to realize beam scanning of a microstripantenna [16], slotted waveguide antenna [17] and all class of array antennas [18]. But before embarking on the design process of a beam scan-able ferrite loaded circular waveguide antenna, understanding the basic properties of waveguide antenna is essential. Basic properties essential for antenna design are briefly discussed below [22]:

- Radiation pattern is defined as "a mathematical function or a graphical representation of the radiation properties of the antenna as a function of space coordinates. In most cases the radiation pattern is determined by the electric field distribution in the far-field region of the antenna, as a function of directional coordinates".

- Directivity of an antenna is defined as "the ratio of the radiation intensity in a given direction to the radiation intensity averaged over all directions. The average radiation intensity is equal to the total power radiation by the antenna divided by4π. If the direction is not specified, the direction of the maximum radiation intensity is implied".

- Efficiency of an antenna is defined as "the ratio of the total power radiated by an antenna over the net power accepted by the antenna". Total antenna efficiency is used to take into account losses at the input terminals and within the structure of the antenna, which may be due referring to reflections caused by the mismatch between the transmission line and the antenna and other losses caused by the conduction and dielectric".

- Gain of an antenna is defined as “the ratio of the intensity, in a given direction, to the radiation intensity that would be obtained from an isotropic antenna. It is a important performance figure that combines antenna directivity and electrical efficiency of the antenna.

- Half-power beam-width is defined as “a plane containing the direction of the maximum of a beam and the angle between the two directions in which the radiation intensity is one-half the maximum value of the beam”.

- Impedance bandwidth of an antenna is defined as “the range of frequencies within which the reflection response of the antenna is less than 10 dB”. The lower reflection relates to the impedance matching characteristic of the antenna for a range of frequencies on either side of the center frequency.

In this research work, an axially magnetized ferrite cylinder will be optimally placed within a coaxially feed circular waveguide antenna to introduce beam scanning properties. To optimize the radiation properties and minimize the lossy resonance regions, a thorough analysis of the external magnetizing properties of a ferrite loaded circular waveguide is essential.

1.3 Thesis Objectives

The objectives of this thesis work are as follows:

1. Investigate the excitation of the circular waveguide to achieve maximum power transfer from the coaxial probe.
2. Formulate the design equations for a circular waveguide with centrally loaded ferrite cylinder. The calculated mode charts will be used to verify the HFSS model of the ferrite loaded antenna.
3. Using professional software (HFSS), design and optimize the axially magnetized ferrite loaded circular waveguide antenna excited by a coaxial probe.
4. Using simulator software, demonstrate the multidirectional beam steering properties of the antenna with respect to external magnetizing field (H_0). The expected characteristics of the antenna with no external biasing should be:
   a. Impedance B/W= 360 MHz,
   b. Antenna HPBW= 70° and
   c. Antenna Gain= 8.5 dB.
   d. A multidirectional beam scan of 35° with changing external biasing field (H_0).
5. Fabricate the prototype of the designed antenna and verify the reflection response (S_{11}) using network analyzer. Also, verify the antenna radiation pattern for certain biasing values.
6. Finally, use the simulator software to investigate the directivity enhancement through introducing EBG superstrate.

CHAPTER 2

CIRCULAR WAVEGUIDE AND FERRITES

2.1 Introduction

The theoretical background of our antenna is presented in this chapter. Our antenna mainly composed of a circular conducting waveguide loaded with concentric ferrite rode. In order to illustrate the modes that propagated inside the structure before it radiates from the open end theoretical development will be presented. First, an empty circular waveguide is considered to show the modes before it is loaded with the ferrite. In the second section in this chapter a theoretical development of a circular waveguide loaded with the ferrite is going to be introduced. It is important to show the modes which will propagate in our structure and compute a mode chart based on our theoretical development and compare them with the modes obtained using a commercial software package. Results for the mentioned mode charts are going to be illustrated at the end of this chapter.

2.2 Mode Charts in Circular Waveguide.

A circular conducting waveguide of inner radius “a” is shown in **Figure 2.1** and **Figure 2.2** where the propagation is in the +z axis.

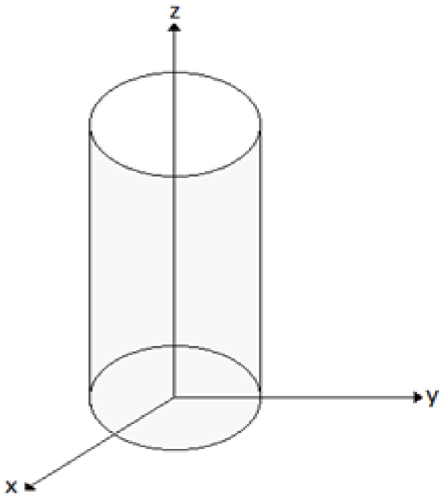

Figure 2.1 Circular waveguide (CWG)

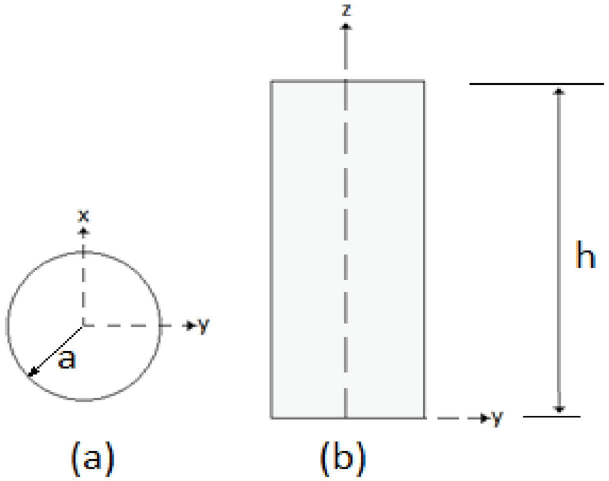

Figure 2.2 (a) Top view, (b) side view of CWG

Maxwell’s equation with proper boundary conditions are typically used to mathematically describes the electromagnetic behavior of a circular waveguide, Using cylindrical coordinates, the Helmholtz equation obtained from Maxwell’s equation is given by [23]:

$$\frac{1}{\rho}\frac{\partial\psi}{\partial\theta}\left(\rho\frac{\partial\psi}{\partial\rho}\right)+\frac{\partial^2\psi}{\partial\varphi^2}\frac{1}{\rho}+\frac{\partial^2\psi}{\partial z^2}= 0 \quad (2.1)$$

For circular waveguide, the solution of equation (2.1) is:

$$\psi(\rho,\varphi,z)=\left[A\,J_n\left(\beta_\rho\rho\right)+B\,Y_n\left(\beta_\rho\rho\right)\right]xe^{-jm\varphi}xe^{-j\beta_z z} \quad (2.2)$$

and$\beta_\rho^2 + \beta_z^2 = \beta^2$(2.3)

Where J_m and Y_m are, respectively, the Bessel functions of the first and second kind of order *m* and $\beta_\rho = \frac{x'_{mn}}{a}$ or $\frac{x_{mn}}{a}$. Circular waveguide with copper wall, as shown in **Figure 2.1** normally supports transverse electric (TE) and the transverse magnetic (TM) modes. By using equation (2.2) and applying the boundary conditions, the expression of the cutoff-frequency and the wavelength of a circular waveguide can be written as [23]:

$$(f_c)_{\mathrm{mn}} = \frac{\beta_\rho}{2\pi\sqrt{\mu\varepsilon}} \qquad (2.4)$$

From equations (2.3) and (2.4):

$$(\beta_z)_{\mathrm{mn}} = \beta\sqrt{1 - (\frac{f_c}{f})^2_{\mathrm{mn}}} \qquad (2.5)$$

The wavelength of the waveguide is expressed as:

$$(\lambda_g)_{\mathrm{mn}} = \frac{\lambda}{\sqrt{1 - \left(\frac{f_c}{f}\right)^2}} \qquad (2.6)$$

where,x'_{mn} is the nth zero of the derivative of the Bessel function of the first kind of order '*m*', '*a'* is the radius of the waveguide, 'μ' is the permeability and 'ε' is the permittivity of the medium inside the waveguide. By definition $\mu = \mu_0\mu_r$, where the magnetic properties of the material inside the waveguide is given by μ_r and the relative permeability in air is expressed by '$\mu_0 = 4\pi\times10^{-7}$ H·m^{-1}'. Similarly the dielectric properties of waveguide filling is expressed by '$\varepsilon = \varepsilon_0\varepsilon_r$', where '$\varepsilon_r$' is the relative permittivity of the filling material compared to permittivity in air/vacuum '$\varepsilon_0 = 8.854187817 \times 10^{-12}$ F·m^{-1}'.

Table 2.1 shows same of the cutoff frequencies of the first five zeroes of TE and TM modes.

Table 2.1: Cutoff frequencies of different modes inside circular waveguide.

$\mathbf{x'_{mn}}$ **or** $\mathbf{x_{mn}}$	**Transverse E or M**	**Cutoff Frequency (GHz)**
1.8412	TE_{11}	8.7911
2.4049	TM_{01}	11.483
3.8318	TE_{01} and TM_{11}	18.296
4.2012	TE_{31}	20.059
5.1357	TM_{21}	24.521

If we consider the dielectric inside the waveguide to be air and the radius of the waveguide is 10 mm, the mode charts of the first five modes inside this circular waveguide are shown in **Figure 2.1** and the wavelength waveguide in **Figure 2.2**. The mode charts obtained in the following figures are computed using equations (2.5) and (2.6), respectively.

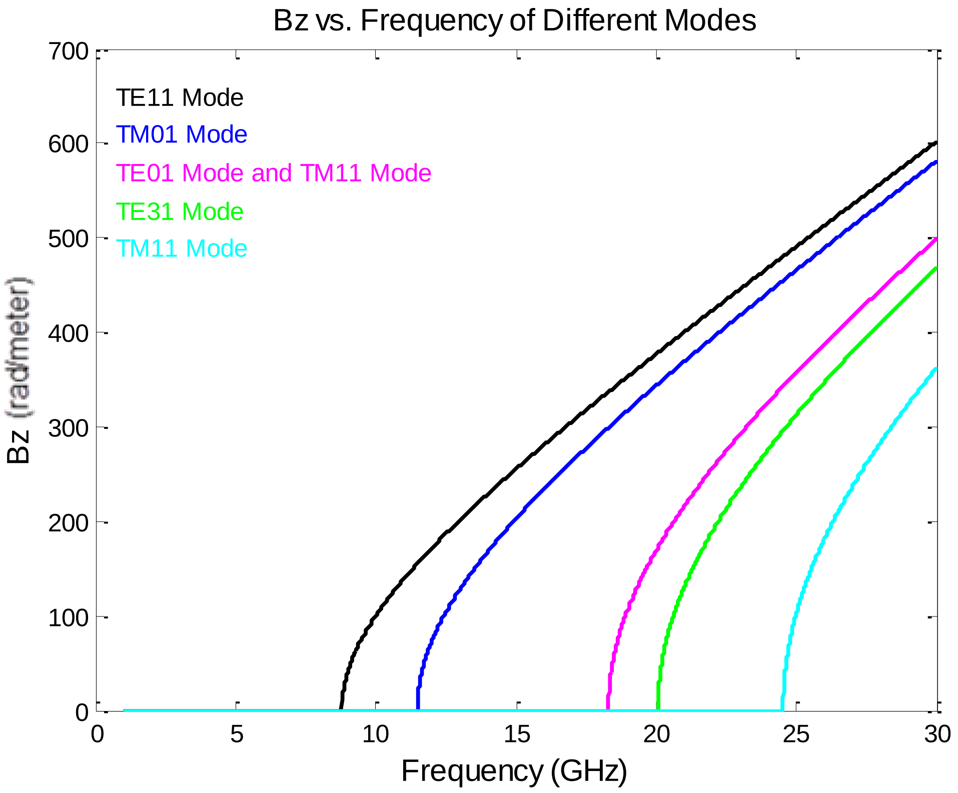

Figure 2.3: Modes chart of circular waveguide.

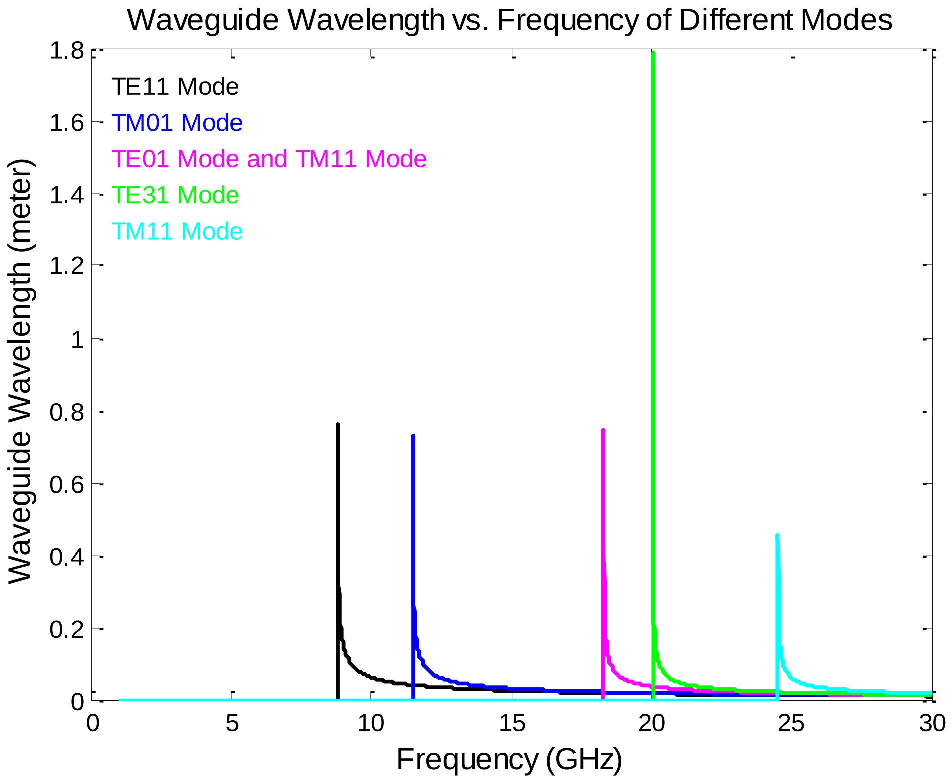

Figure 2.4: waveguide wavelength of circular waveguide

From the **Figure 2.1,** if we select the operating frequency to be 10 GHz, the modes propagate at this frequency is only the dominant mode (TE_{11}) with waveguide wavelength 'λ_g' is 62.9 mm and phase constant 'β' is around 100 rad/meter.

2.3 Mode Charts in Axially Magnetized Ferrite Cylinder.

When magnetized, the gyromagnetic properties of ferrite material interact with the electromagnetic (EM) signal and can affect their magnitude and the phase distribution [20]. In the resonance region, the interaction is very strong and the EM wave is absorbed by ferrites. In literature [21], ferrites substrates are used to introduce 90° beam scan for a microstrip array when biased by an external DC field of 7.9 kA/m [21].

At microwave frequencies, the gyromagnetic properties of an axially magnetized ferrite cylinder is expressed by the tensor permeability [μ_r] of the from [24];

$$[\mu_r] = \begin{bmatrix} \mu & -j\kappa & 0 \\ j\kappa & \mu & 0 \\ 0 & 0 & \mu_z \end{bmatrix} \qquad (2.7)$$

$$\text{where,} \quad \mu = 1 + \frac{\gamma^2 . H_0 . M}{(\gamma H_0)^2 - f^2}, \quad \kappa = \frac{\gamma . M . f}{(\gamma H_0)^2 - f^2}$$

'γ' is the gyromagnetic ratio, 'H_0' is applied magnetizing field 'M' is the magnetization, and '*f*' is the operating frequency of the propagating microwave signal.

In order to find the relationships between the different components of the fields inside the ferrite cylinder it is necessary to go to Maxwell's equations. The derivation of the fields is shown in details in **APPENDIX A**. The field components inside the ferrite are

$$E_z = A_1 J_n(s_1\rho) + A_2 J_n(s_2\rho) \qquad (2.8)$$

$$H_z = A_1 r_1 J_n(s_1\rho) + A_2 r_2 J_n(s_2\rho) \qquad (2.9)$$

$$\begin{aligned}\overline{E}_\rho &= \frac{A_1 s_1 J'_n(s_1\rho)}{(\Omega^4 - k'^4)}(-\Omega^2\Gamma + r_1\Gamma^2\omega K) + \frac{A_1 n J_n(s_1\rho)}{\rho(\Omega^4 - k'^4)}(\Gamma k'^2 + r_1\omega(\mu\Omega^2 - k'^2 K)) \\ &+ \frac{A_2 s_2 J'_n(s_2\rho)}{(\Omega^4 - k'^4)}\{-\Omega^2\Gamma + r_2\Gamma^2\omega K\} + \frac{A_2 n J_n(s_2\rho)}{\rho(\Omega^4 - k'^4)}(\Gamma k'^2 + r_2\omega(\mu\Omega^2 - k'^2 K))\end{aligned} \tag{2.10}$$

$$\begin{aligned}\overline{H}_\rho &= \frac{A_1 s_1 J'_n(s_1\rho)}{(\Omega^4 - k'^4)}(-r_1\Omega^2\Gamma + k'^2\omega\varepsilon) + \frac{A_1 n J_n(s_1\rho)}{\rho(\Omega^4 - k'^4)}(-\omega\varepsilon\Omega^2 + r_1 k'^2\Gamma) \\ &+ \frac{A_2 s_2 J'_n(s_2\rho)}{(\Omega^4 - k'^4)}(-r_2\Omega^2\Gamma + k'^2\omega\varepsilon) + \frac{A_2 n J_n(s_2\rho)}{\rho(\Omega^4 - k'^4)}(-\omega\varepsilon\Omega^2 + r_2 k'^2\Gamma)\end{aligned} \tag{2.11}$$

$$\begin{aligned}\overline{E}_\phi &= \frac{jA_1 n J_n(s_1\rho)}{\rho(\Omega^4 - k'^4)}(-\Omega^2\Gamma + r_1\Gamma^2\omega K) + \frac{jA_1 s_1 J'_n(s_1\rho)}{(\Omega^4 - k'^4)}(r_1\omega(\mu\Omega^2 - k'^2 K) + k'^2\Gamma) \\ &+ \frac{jA_2 n J_n(s_2\rho)}{\rho(\Omega^4 - k'^4)}(-\Omega^2\Gamma + r_2\Gamma^2\omega K) + \frac{jA_2 s_2 J'_n(s_2\rho)}{(\Omega^4 - k'^4)}(r_2\omega(\mu\Omega^2 - k'^2 K) + k'^2\Gamma)\end{aligned} \tag{2.12}$$

$$\begin{aligned}\overline{H}_\phi &= -\frac{jA_1 s_1 J'_n(s_1\rho)}{(\Omega^4 - k'^4)}(\omega\varepsilon\Omega^2 - r_1 k'^2\Gamma) - \frac{jA_1 n J_n(s_1\rho)}{\rho(\Omega^4 - k'^4)}(\Omega^2\Gamma r_1 - k'^2\omega\varepsilon) \\ &- \frac{jA_2 s_2 J'_n(s_2\rho)}{(\Omega^4 - k'^4)}(\omega\varepsilon\Omega^2 - r_2 k'^2\Gamma) - \frac{jA_2 n J_n(s_2\rho)}{\rho(\Omega^4 - k'^4)}(\Omega^2\Gamma r_2 - k'^2\omega\varepsilon)\end{aligned} \tag{2.13}$$

The magnetic side wall boundaries will be applied to calculate the modes chart of the ferrite cylinder, where at the radius of ferrite ‘b’, H_ϕ = 0 and H_z = 0. The derived characteristic equation for an axially magnetized ferrite cylinder with radius b is given by;

$$\begin{aligned}&\frac{A_1 s_1 J_n'(s_1 b)}{(\Omega^4 - k'^4)}(\omega\varepsilon\Omega^2 - r_1 k'^2\Gamma) + \frac{A_1 n J_n(s_1 b)}{b(\Omega^4 - k'^4)}(\Omega^2\Gamma r_1 - k'^2\omega\varepsilon)\\ &+ \frac{A_2 s_2 J_n'(s_2 b)}{(\Omega^4 - k'^4)}(\omega\varepsilon\Omega^2 - r_2 k'^2\Gamma) + \frac{A_2 n J_n(s_2 b)}{b(\Omega^4 - k'^4)}(\Omega^2\Gamma r_2 - k'^2\omega\varepsilon) = 0 \qquad (2.14)\end{aligned}$$

and

$$s_{1,2}{}^{2} = \frac{(a+c) \pm \sqrt{(a-c)^2 + 4bd}}{2}$$

where, all variables are defined in **Appendix A**.

Note that in above equations, the field-frequency cut-off chart for a ferrite cylinder can be derived by substituting Γ= 0. The related cut-off chart is plotted in **Figure 2.3** for n = 0 and the range of the frequency is from 0-12 GHz while **Figure 2.4** for n = 0 to n = 5 and the range of the frequency is from 8-12 GHz. Note that the lossy resonance region is shaded (yellow) in the graph and is avoided to minimize losses. From equation (2.14) and for the operating frequency of 10 GHz, the β_H_{dc} chart is plotted in **Figure 2.5**. Note that operating close to resonance regions can give maximum changes of β for certain changes external biasing field (H_0).

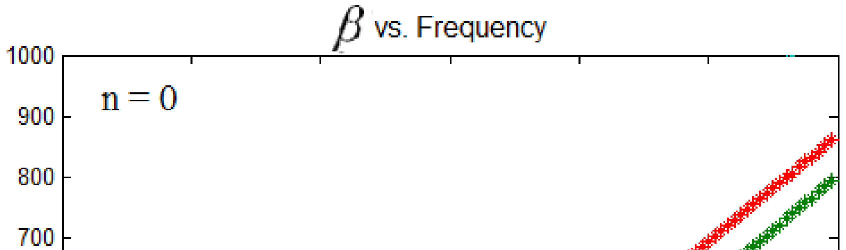

Figure 2.5: Modes chart of ferrite cylinder with n = 0.

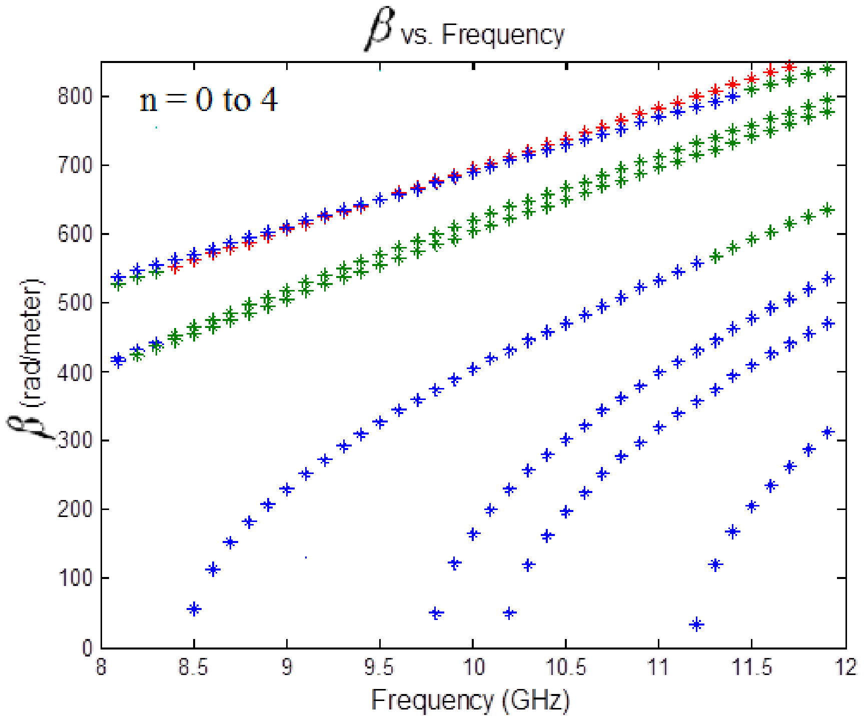

Figure 2.6: Modes chart of ferrite cylinder with n = 0 to n = 4.

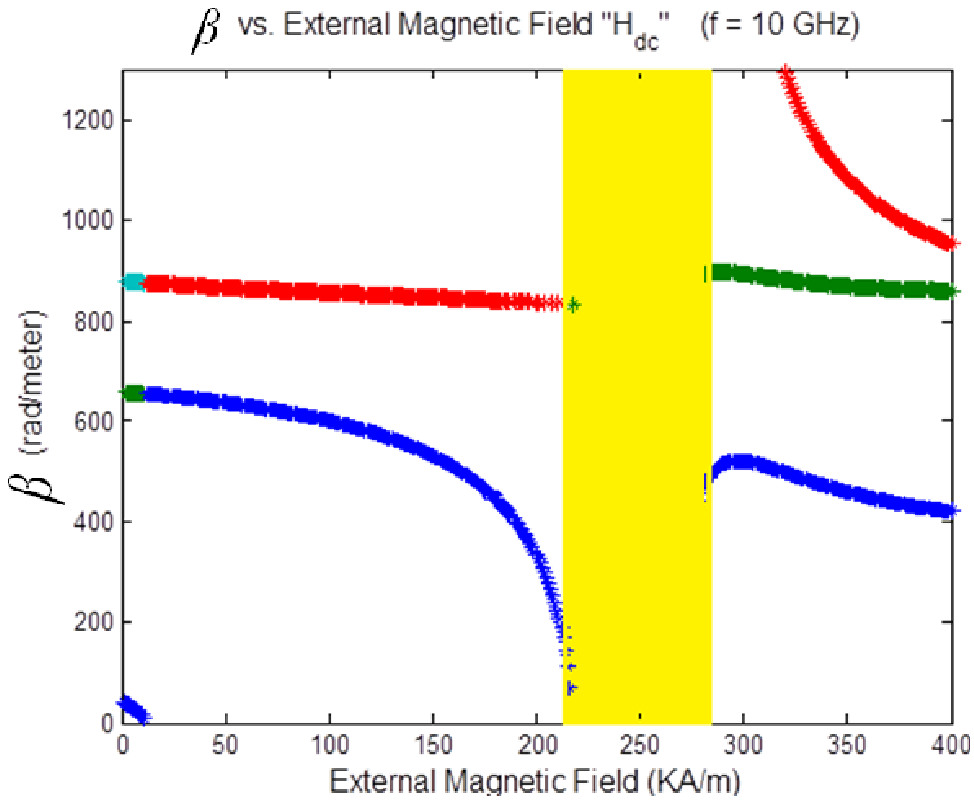

Figure 2.7: Resonance region of ferrite cylinder with operating frequency f = 10 GHz.

2.4 Mode Charts in Circular Waveguide Concentrically Loaded with Ferrite Cylinder.

In this section, the ferrite loaded waveguide as shown in **Figure 2.6** is considered with propagation is in the z – axis. The conducting waveguide has a radius of “a” and the concentrically ferrite cylinder has a radius of “b”. There are two region, region I which is the region inside the ferrite cylinder with radius equals “b” and region II which is the free space “dielectric” between ferrite and conducting waveguide. The modes are considered to be hybrid modes.

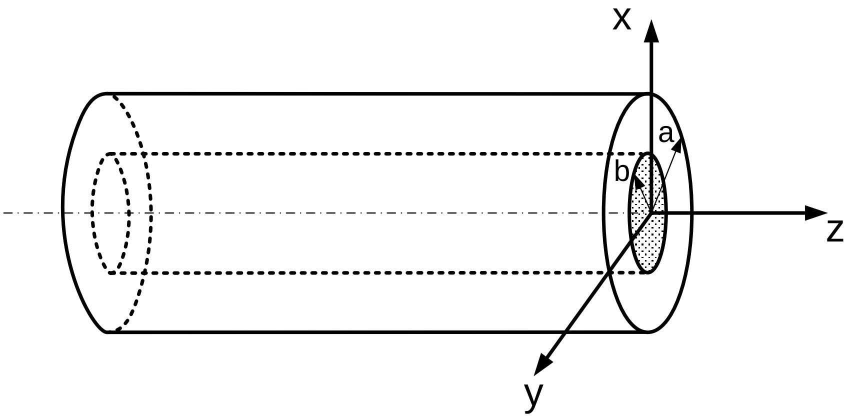

Figure2.8: Concentrically ferrite loaded waveguide.

The filed components in ‘region I’ are found in the previous section in equations 2.8 to 2.13. For ‘region II’, the derivation of the fields components in this region is shown in details in APPENDIX A and the field components are

$$E_z = A_3 J_n(k_d\rho) + A_4 Y_n(k_d\rho) \quad (2.14)$$

$$H_z = A_5 J_n(k_d\rho) + A_6 Y_n(k_d\rho) \quad (2.15)$$

$$E_\rho = -A_3\frac{\Gamma}{k_d}J_n'(k_d\rho) - A_4\frac{\Gamma}{k_d}Y_n'(k_d\rho) + A_5\frac{n\omega\mu}{\rho k_d^2}J_n(k_d\rho) + A_6\frac{n\omega\mu}{\rho k_d^2}Y_n(k_d\rho) \quad (2.16)$$

$$H_\rho = -A_3 \frac{n\omega\varepsilon}{\rho k_d^2} J_n(k_d\rho) - A_4 \frac{n\omega\varepsilon}{\rho k_d^2} Y_n'(k_d\rho) - A_5 \frac{\Gamma}{k_d} J_n'(k_d\rho) - A_6 \frac{\Gamma}{k_d} Y_n'(k_d\rho) \quad (2.17)$$

$$E_\phi = -jA_3 \frac{n\Gamma}{\rho k_d^2} J_n(k_d\rho) - jA_4 \frac{n\Gamma}{\rho k_d^2} Y_n(k_d\rho) + jA_5 \frac{\omega\mu}{k_d} J_n'(k_d\rho) + jA_6 \frac{\omega\mu}{k_d} Y_n'(k_d\rho) \quad (2.18)$$

$$H_\phi = -jA_3 \frac{\omega\varepsilon}{k_d} J_n'(k_d\rho) - jA_4 \frac{\omega\varepsilon}{k_d} Y_n'(k_d\rho) - jA_5 \frac{n\Gamma}{\rho k_d^2} J_n(k_d\rho) - jA_6 \frac{n\Gamma}{\rho k_d^2} Y_n(k_d\rho) \quad (2.19)$$

After finding all components in the two regions, the boundary conditions will be applied to find the characteristic equation of the ferrite loaded waveguide. The boundary conditions are at ρ equals to *b ‘radius of ferrite’* and ρ equals to *a ‘radius of waveguide’* where at ‘$\rho = b$’ the tangential components which are “E_z, H_z, E_ϕ and H_ϕ” in ‘region I’ equal the tangential components in ‘region II’ and at ‘$\rho = a$’ the tangential components in ‘region II’ equal zero. The characteristic equation is derived in APPENDIX A and is given by:

$$A_3 J_n(k_d a) + A_4 Y_n(k_d a) = 0$$

$$A_5 J'_n(k_d a) + A_6 Y'_n(k_d a) = 0$$

$$A_1 J_n(s_1 b) + A_2 J_n(s_2 b) - A_3 J_n(k_d b) - A_4 Y_n(k_d b) = 0$$

$$A_1 r_1 J_n(s_1 b) + A_2 r_2 J_n(s_2 b) - A_5 J_n(k_d b) - A_6 Y_n(k_d b) = 0$$

$$\begin{aligned}
&\frac{A_1 n J_n(s_1 b)}{b(\Omega^4 - k'^4)}(-\Omega^2\Gamma + r_1\Gamma^2\omega K) + \frac{A_1 s_1 J'_n(s_1 b)}{(\Omega^4 - k'^4)}(r_1\omega(\mu\Omega^2 - k'^2K) + k'^2\Gamma) \\
&+ \frac{A_2 n J_n(s_2 b)}{b(\Omega^4 - k'^4)}(-\Omega^2\Gamma + r_2\Gamma^2\omega K) + \frac{A_2 s_2 J'_n(s_2 b)}{(\Omega^4 - k'^4)}(r_2\omega(\mu\Omega^2 - k'^2K) + k'^2\Gamma) \\
&+ A_3\frac{n\Gamma}{bk_d^2}J_n(k_d b) + A_4\frac{n\Gamma}{bk_d^2}Y_n(k_d b) - A_5\frac{\omega\mu}{k_d}J'_n(k_d b) - A_6\frac{\omega\mu}{k_d}Y'_n(k_d b) = 0
\end{aligned}$$

$$\begin{aligned}
&\frac{A_1 s_1 J'_n(s_1 b)}{(\Omega^4 - k'^4)}(\omega\varepsilon\Omega^2 - r_1 k'^2\Gamma) + \frac{A_1 n J_n(s_1 b)}{b(\Omega^4 - k'^4)}(\Omega^2\Gamma r_1 - k'^2\omega\varepsilon) \\
&+ \frac{A_2 s_2 J'_n(s_2 b)}{(\Omega^4 - k'^4)}(\omega\varepsilon\Omega^2 - r_2 k'^2\Gamma) + \frac{A_2 n J_n(s_2 b)}{b(\Omega^4 - k'^4)}(\Omega^2\Gamma r_2 - k'^2\omega\varepsilon) \\
&- A_3\frac{\omega\varepsilon}{k_d}J'_n(k_d b) - A_4\frac{\omega\varepsilon}{k_d}Y'_n(k_d b) - A_5\frac{n\Gamma}{bk_d^2}J_n(k_d b) - A_6\frac{n\Gamma}{bk_d^2}Y_n(k_d b) = 0
\end{aligned}$$

Matlab code is used to find the determinant of the above matrix ‘6 unknown by 6 equations’, the modes chart can be found. **Figure 2.7** present the modes chart of Bessel’s order n = 0 and the range of the frequency is from 0 to 12 GHz. **Figure 2.8** present the

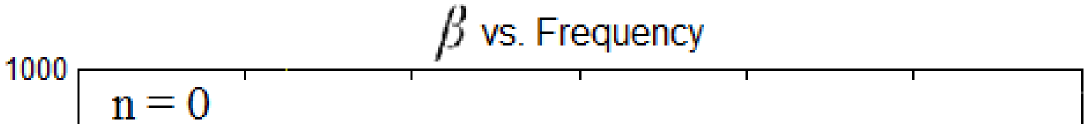

modes chart of Bessel's order n = 0 to n = 4 and the range of the frequency is from 8 to 12 GHz.

Figure 2.9: Modes chart of loaded ferrite waveguide with n = 0.

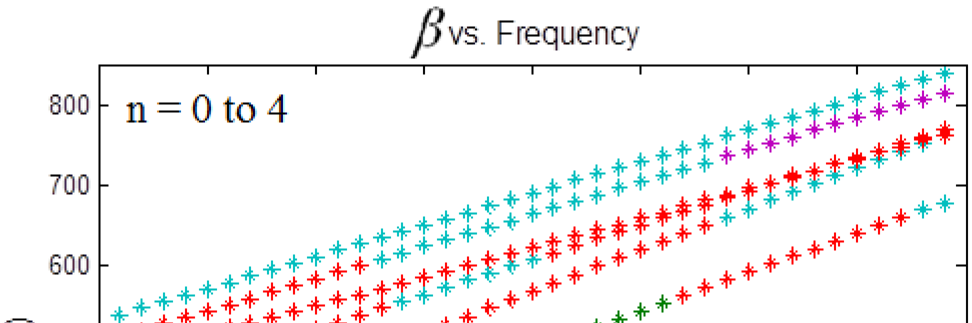

Figure 2.10: Modes chart of loaded ferrite waveguide with n = 0 to n = 4.

From the **Figure 2.8,** the propagation constant at 10 GHz for the dominant mode is 655 rad/meter. From the **Figure 2.7,** the cutoff frequency of one the modes is around 4 GHz. These results will be compared with the simulated results.

2.5 Validation of Simulated Model Waveguide

By using HFSS, the model of the waveguide has been designed. The radius of the waveguide is 10 mm. The excitations are assigned from the ends of the waveguide ‘ideal excitation’ by defining 5 modes in HFSS as shown in**Figure 2.9.**

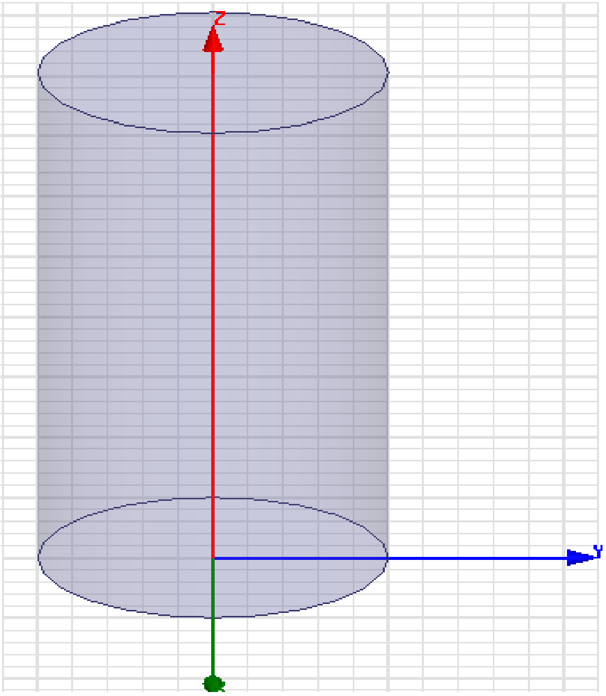

Figure 2.11: The waveguide in the HFSS.

The purpose from doing this step is to find the mode charts ‘phase constant (β vs. frequency)’ shown in**Figure 2.10** and waveguide wavelength ‘λ $_g$’ vs. frequency shown in **Figure 2.11**’. The collected information from this plot shows that there is only one mode propagating in the waveguide with cutoff frequency equals to 8.7 GHz, phase constant equals to around 100 rad/meter and the waveguide wavelength equals to around 62.8 mm . These results from HFSS identify the theoretical results found in section 2.2.

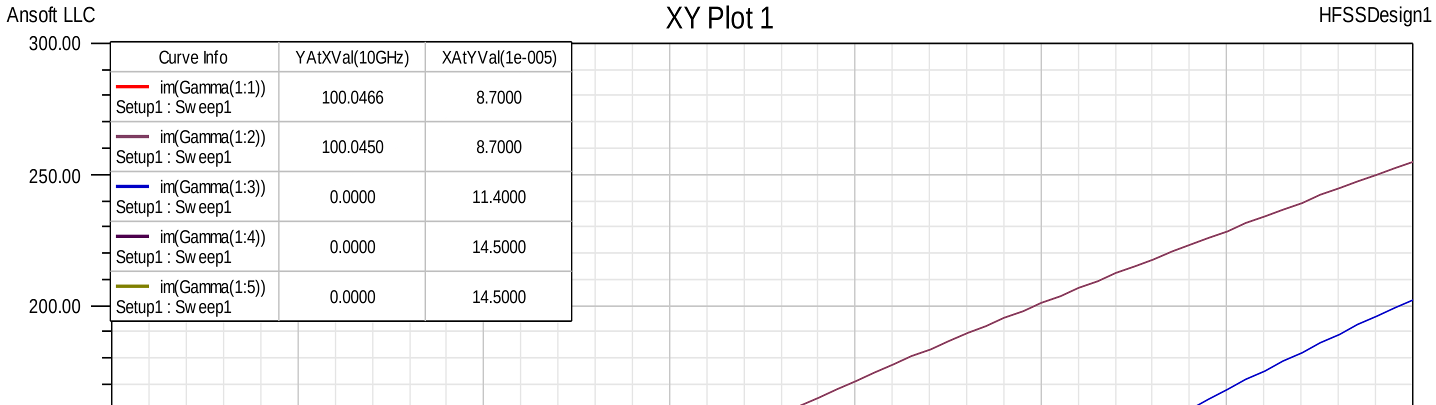

Figure 2.12:β vs frequency for different modes for cuiclar waveguide using HFSS

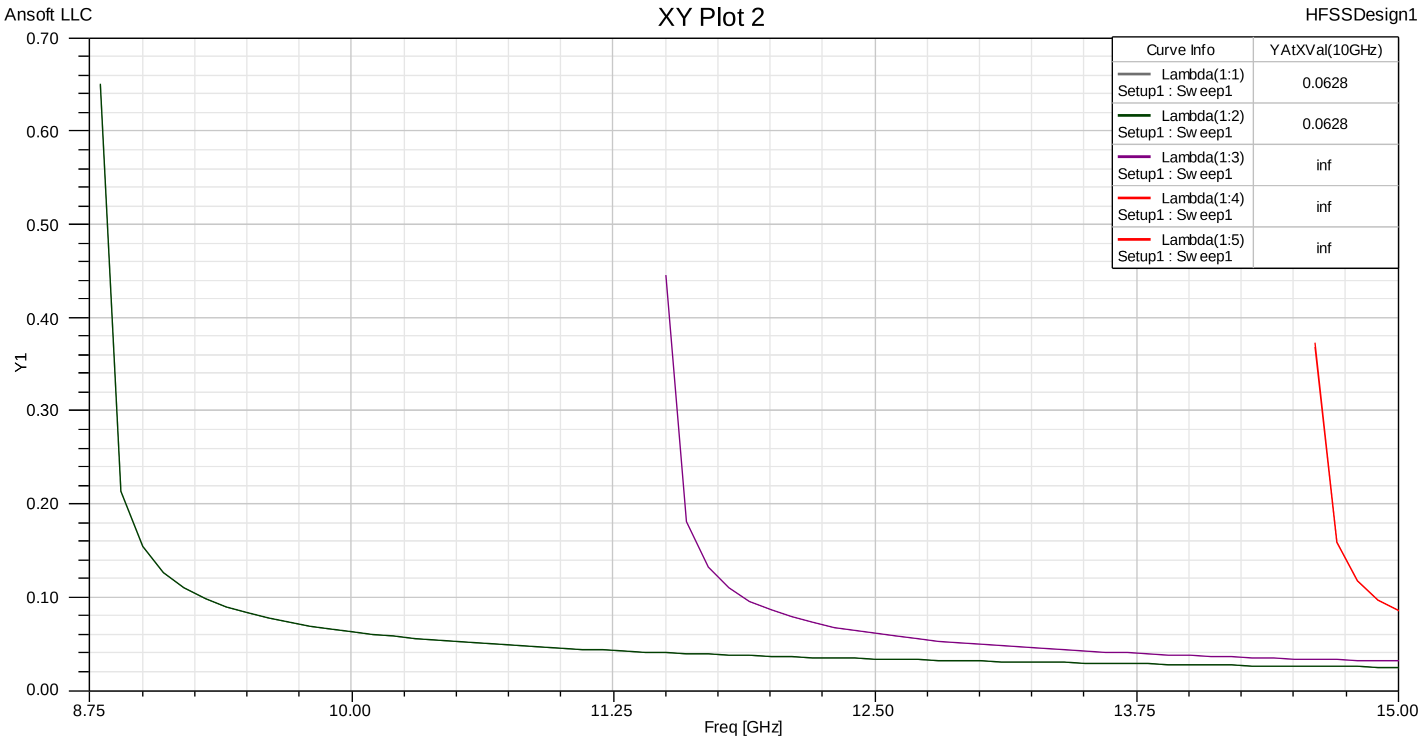

Figure 2.13:$\lambda_g$vs frequency for different modes

Now, the loaded ferrite waveguide will be designed in the HFSS to find the waveguide wavelength ‘which is needed to design the antenna later’ and the modes that will propagate inside the loaded waveguide with the cutoff frequencies for each mode. **Figure 2.12**shows the loaded ferrite waveguide in HFSS with ideal excitation by defining 8 modes.

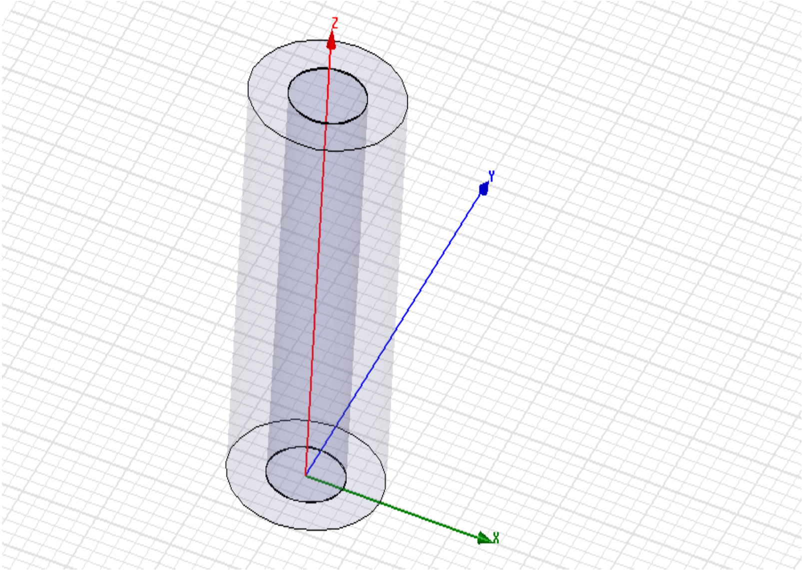

Figure 2.14: The loaded waveguide in the HFSS.

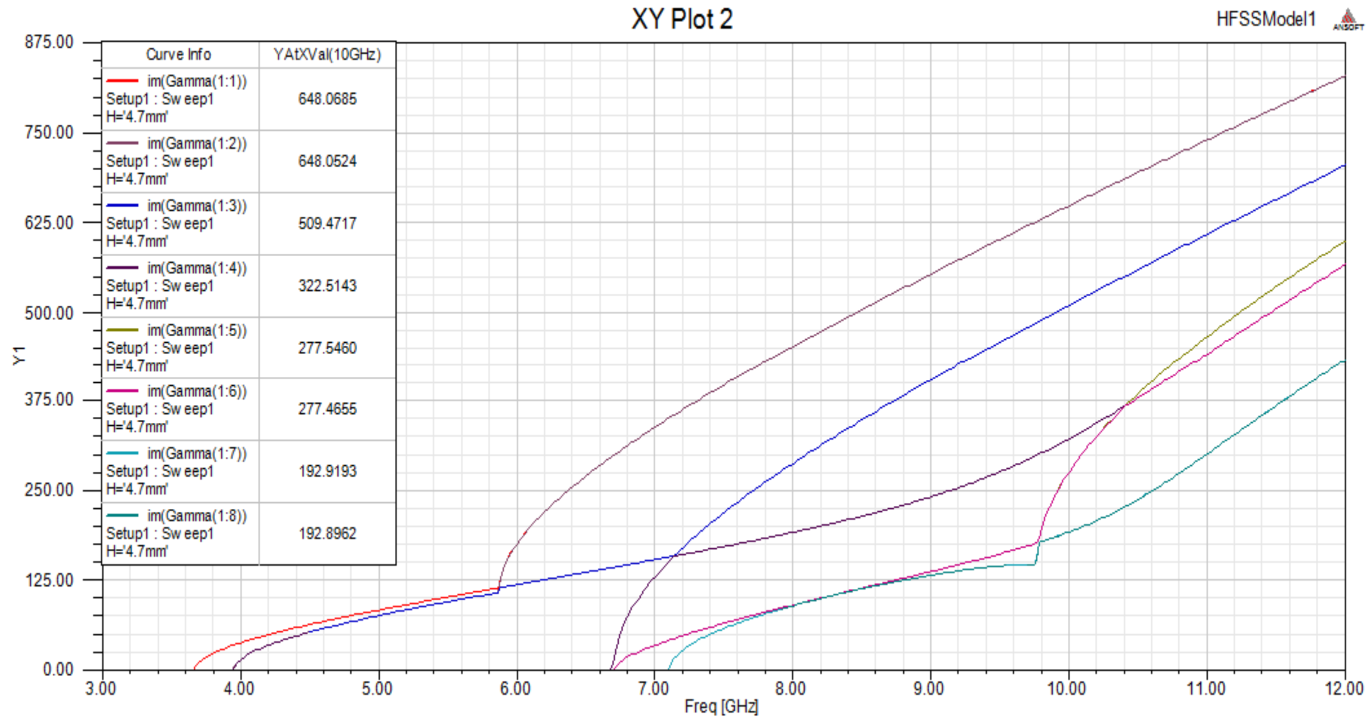

Figure 2.15:β vs frequency for different modes for loaded waveguide in the HFSS

The collected information from this plot shows that there are five modes propagating in the waveguide with cutoff frequency shown in the **Figure 2.13**. Phase constant for the dominant mode equals to around 648 rad/meter and from the relationship between the waveguide wavelength and the phase constant [23] ‘ $\beta * \lambda_g = 2\pi$ ’ the waveguide wavelength equals to around 9.7 mm. The theoretical results are, the phase constant at 10 GHz of the dominant mode is 655 rad/meter **Figure 2.7** and the cutoff frequency of one of the modes is around 4 GHz **Figure 2.8**. These results match the results found in HFSS **Figure 2.13**.

For each mode, S11 ‘reflection’ and S21 ‘transmission’ parameters **Figure 2.14** to **Figure 2.18**is calculatedin HFSS of two ports loaded waveguide of **Figure 2.12**. The cutoff frequencies points can be noticed in the figures.

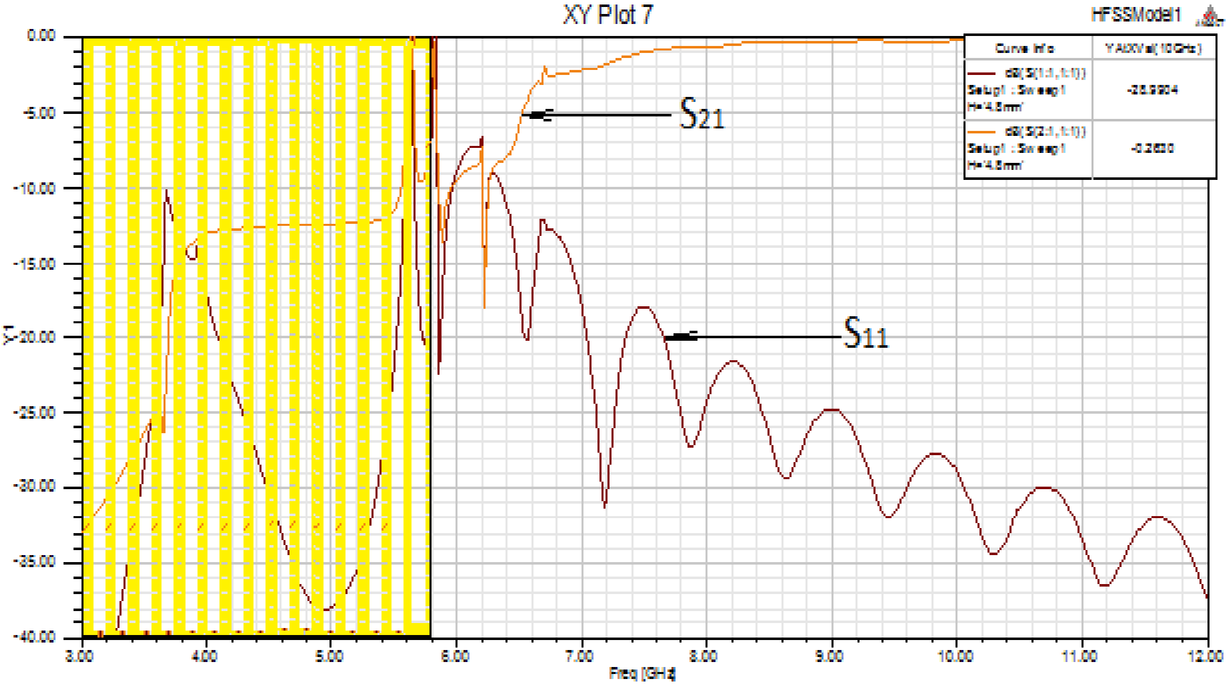

Figure 2.16: Only first mode, S_{11} and S_{21} vs. frequency.

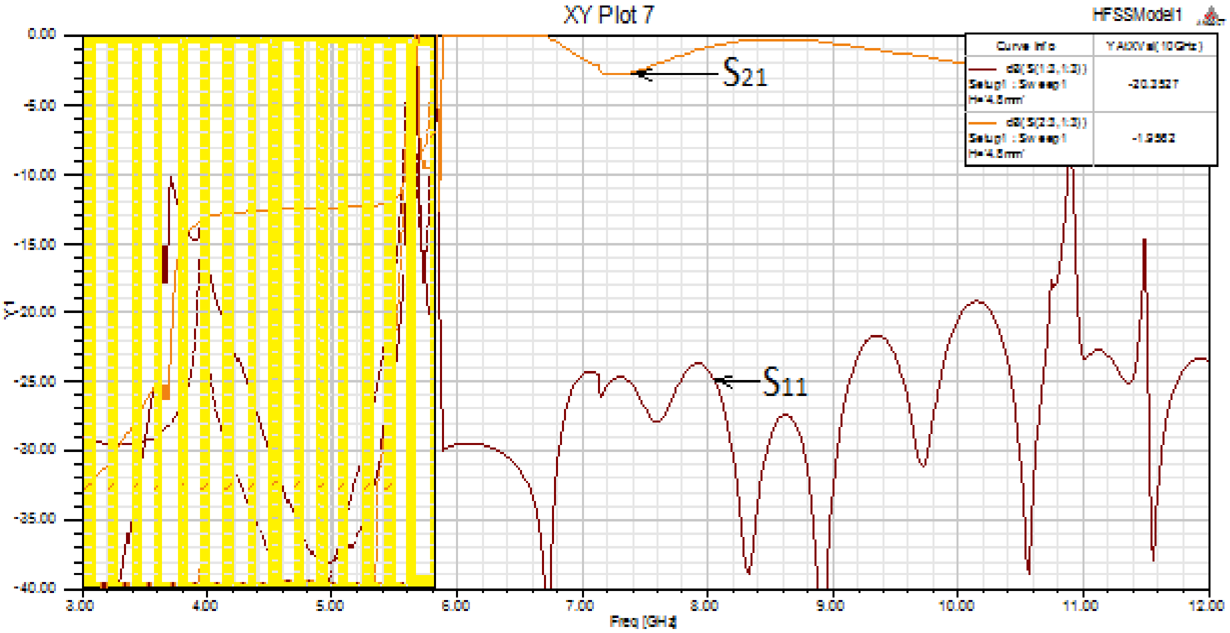

Figure 2.17: Only second mode, S_{11} and S_{21} vs. frequency.

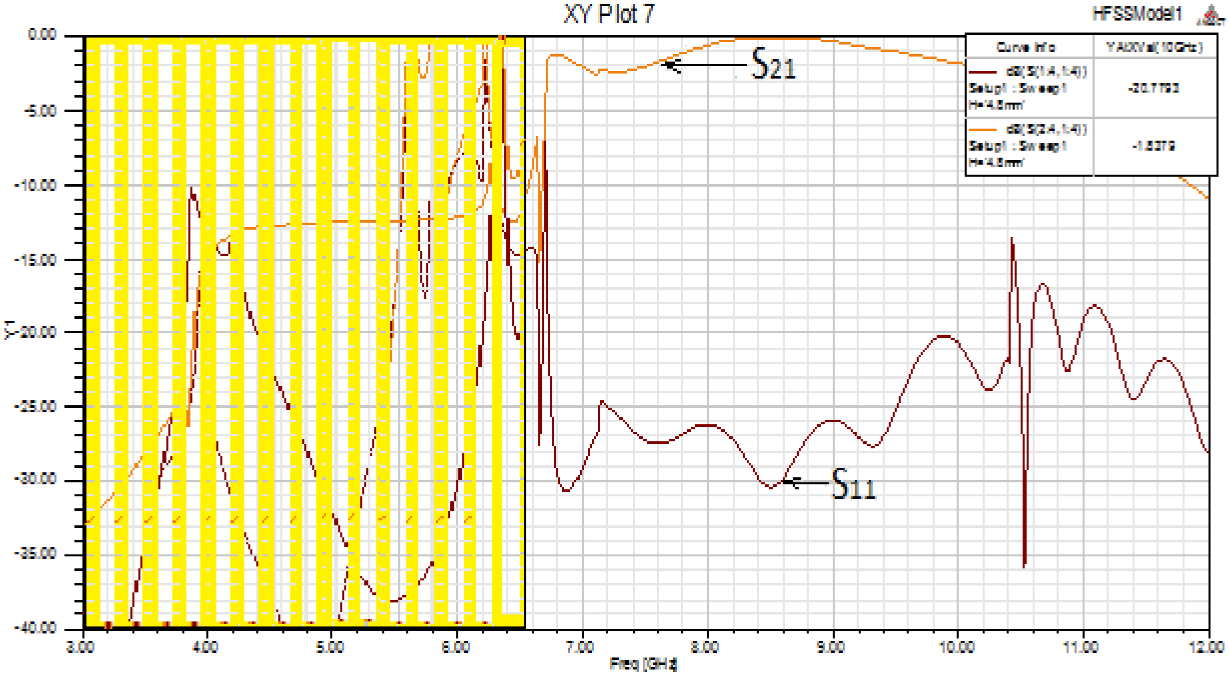

Figure 2.18: Only third mode, S_{11} and S_{21} vs. frequency.

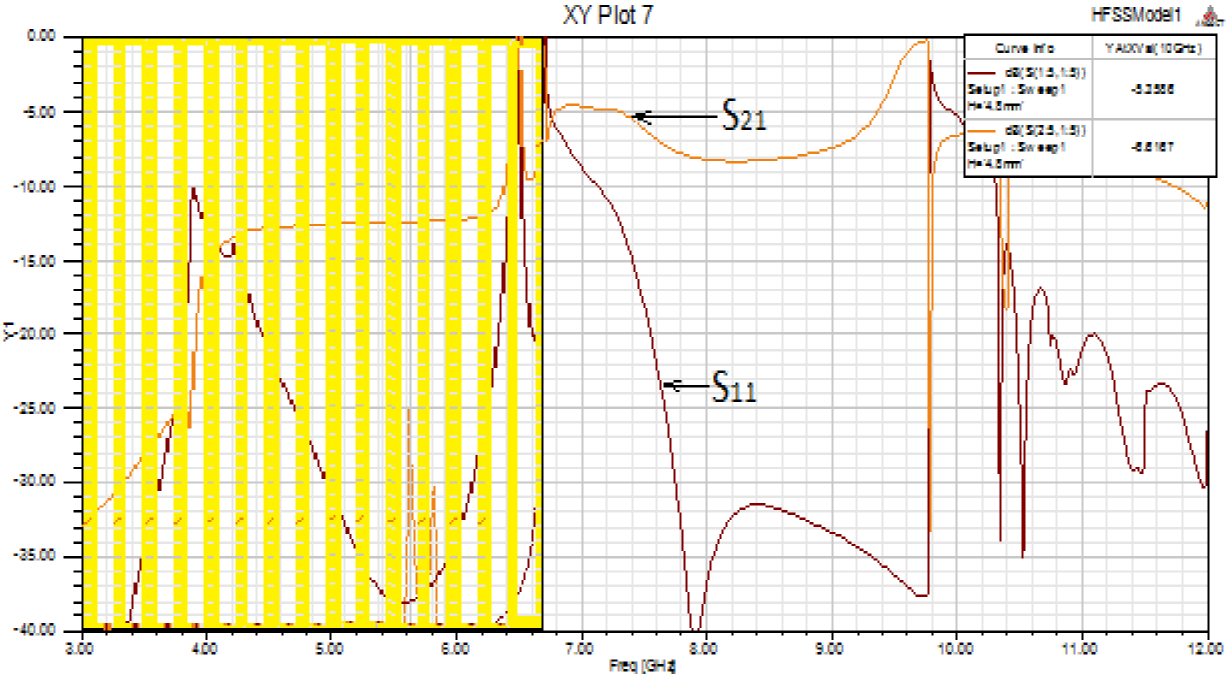

Figure 2.19: Only fourth mode, S_{11} and S_{21} vs. frequency.

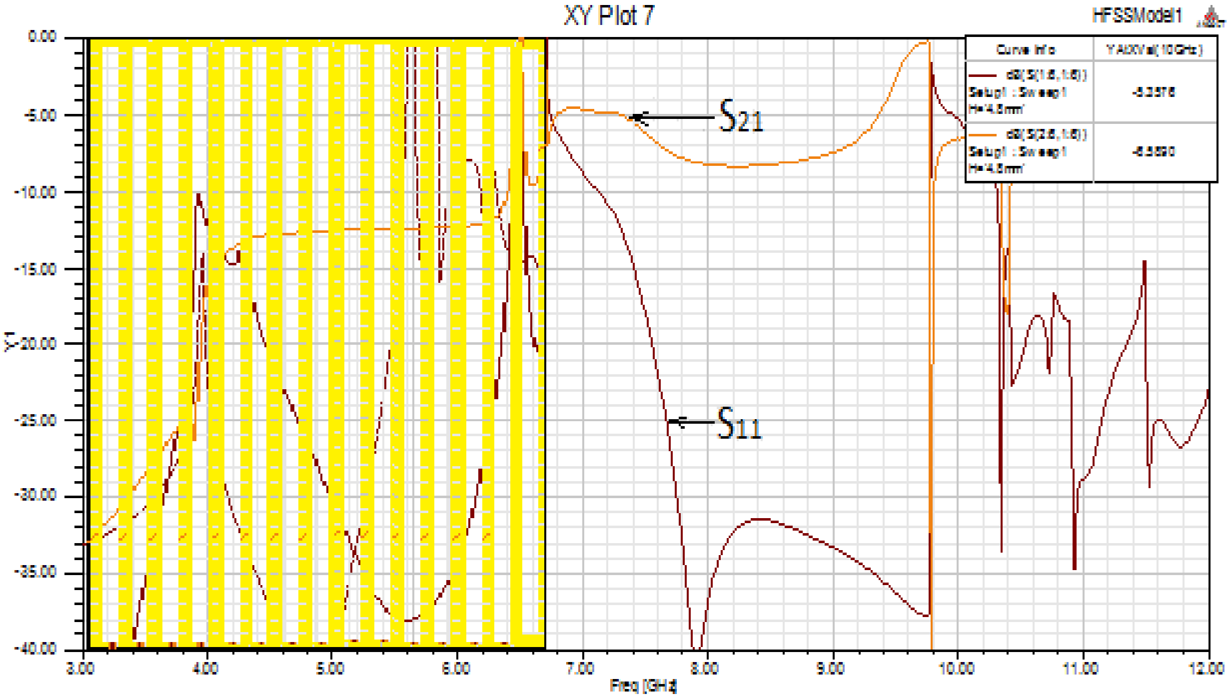

Figure 2.20: Only fifth mode, S_{11} and S_{21} vs. frequency.

CHAPTER 3

DESIGN OF CIRCULAR WAVEGUIDE ANTENNA CONCENTRICALLY LOADED WITH BISAED FERRITE CYLINDER

3.1 Introduction

This chapter presents steps to design the circular waveguide antenna concentrically loaded with ferrite cylinder. Section 3.2 discusses the available excitation techniques of a waveguide at an operating frequency. Section 3.3 presents the design of ferrite loaded waveguide antenna. The effects of feed location, ferrite and waveguide dimensions and magnetizing the ferrite cylinder are discussed in this section. Section 3.4 presents the results of the beam scanning properties of the ferrite loaded waveguide antenna.

3.2 Excitation Technique of Waveguide Antennas

There are several methods to couple the wave into the circular waveguide antenna. The most common methods are [19]:

1- Using a ‘coaxial’ probe, where the position of this probe inside the waveguide is selected according to coupling required **Figure 3.1**.

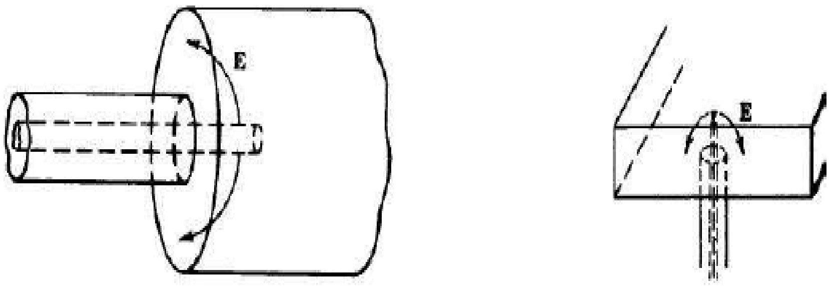

Figure. 3.1: A probe used to excite the waveguide through coupling the E-fields.

2- Using loop oriented to carry a current into in the plane normal to the magnetic field as shown **Figure 3.2**.

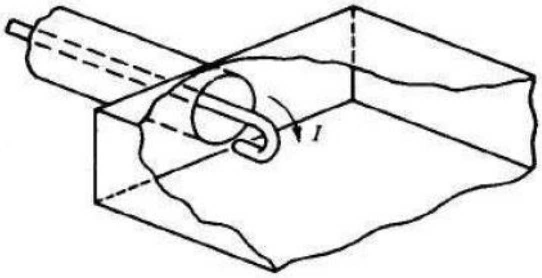

Figure 3.2: A loop used to excite waveguide through coupling the E-fields.

3- Using a small slit in the waveguide as shown in **Figure 3.3** where the slit in the transverse plane acts as inductive impedance and the slit in the broadside will act as capacitive impedance. The slit size and shape will determine the impedance.

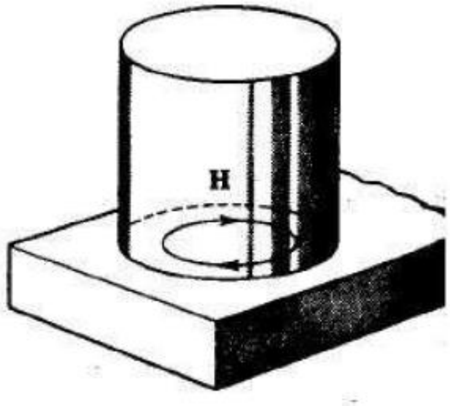

Figure 3.3: A loop used to excite waveguides.

In this research work, the circular waveguide antenna is excited with a probe using E-field coupling mechanism. The size, position and penetration depth of the probe needs to be optimized using HFSS.

3.3 Design of the Ferrite Loaded Waveguide Antenna

The schematic diagram of the software model, designed using “High Frequency Structural Simulator (HFSS)”, is shown in **Figure 3.4**. To select proper meshing for the software model, the simulated mode charts of the loaded waveguide (with ideal excitation) is compared to the analytically calculated mode charts. This comparison is presented in section 2.5 of the earlier chapter. The parameters of the ferrite loaded waveguide, excited with coaxial probe, are as follows:

1- Selected operating frequency of 10 GHz.
2- Waveguide wavelength “λ_g= 9.7 mm”.
3- Radius of the waveguide “a = 10 mm”.
4- Length of the waveguide “$H = 4\lambda_g = 38.8$ mm”.
5- Radius of the ferrite cylinder “b = 5 mm”.
6- Length of the ferrite cylinder= 38.8 mm”.

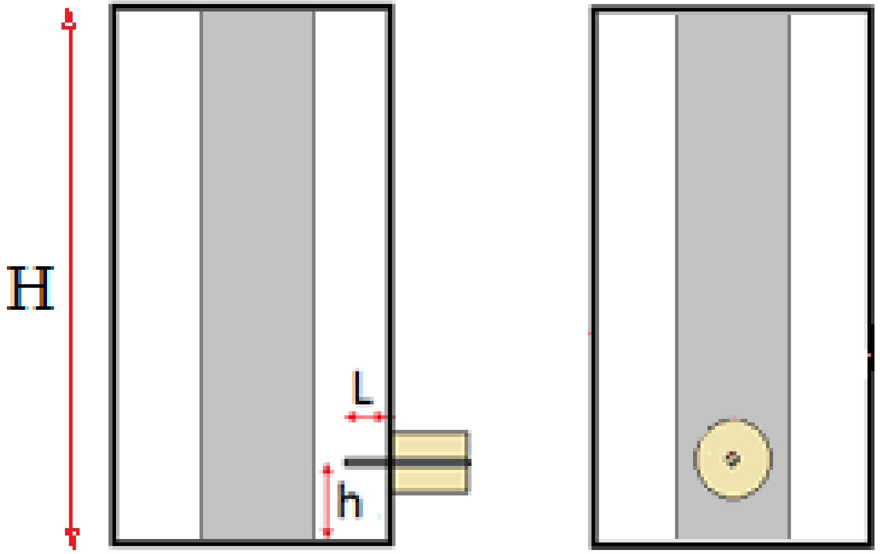

Figure 3.4: Schematic diagram of the coaxially feed circular waveguide antenna, concentrically loaded with axially magnetized ferrite cylinders

The coaxial probe, inserted through one the side of the waveguide, is optimally positioned to achieve best impedance response at the design frequency of 10 GHz. The maximum coupling between the coaxial feeder and the waveguide is achieved by selecting the proper values of “L” and “H”, as labelled in **Figure 3.4**. Using the Parametric analysis of the simulated model, discussed in the following sub-section, the optimum penetration of the probe inside the waveguide antenna (L) and the height of the probe from the ground end of the waveguide (H) is determined. The air box of the simulated model, shown in **Figure 3.5**, has perfectly matched (or radiation) boundaries and is needed to calculate the radiation properties of the antenna. The basic antenna parameters, like gain, efficiency, beamwidth are also be obtained from the simulated results.

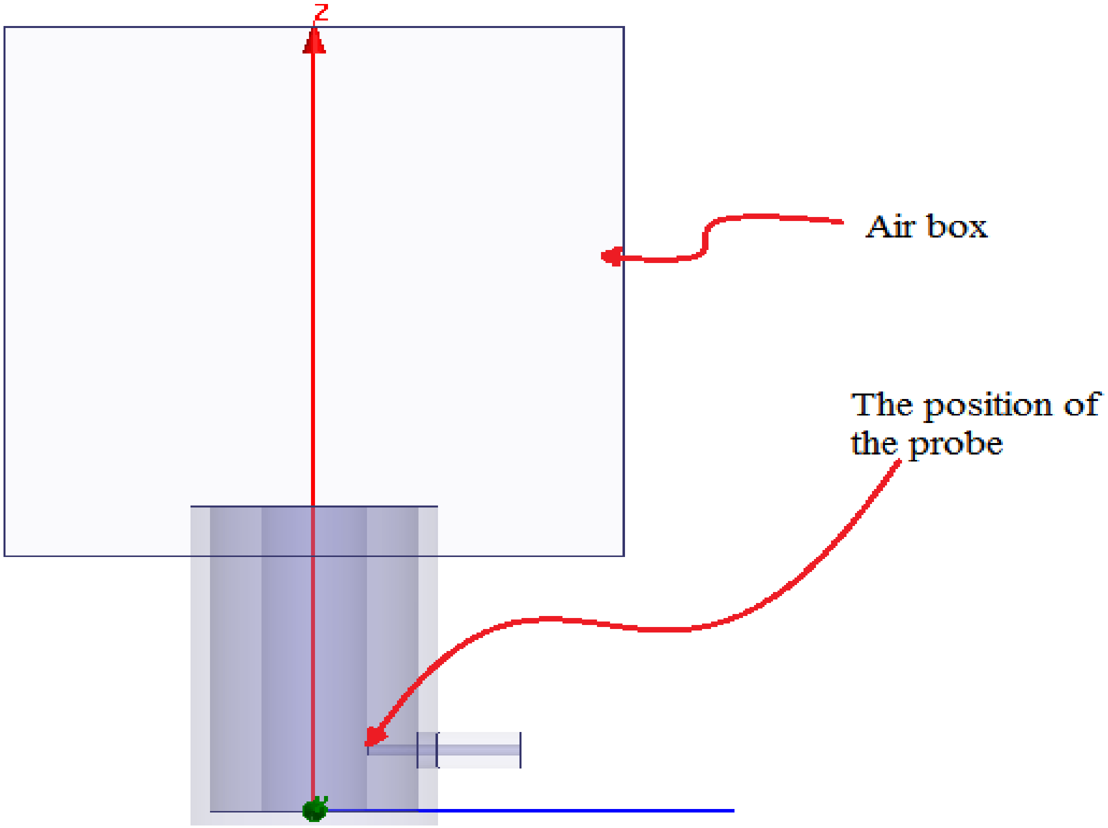

Figure 3.5: The simulated (HFSS) model of the coaxially feed ferrite loaded waveguide antenna.

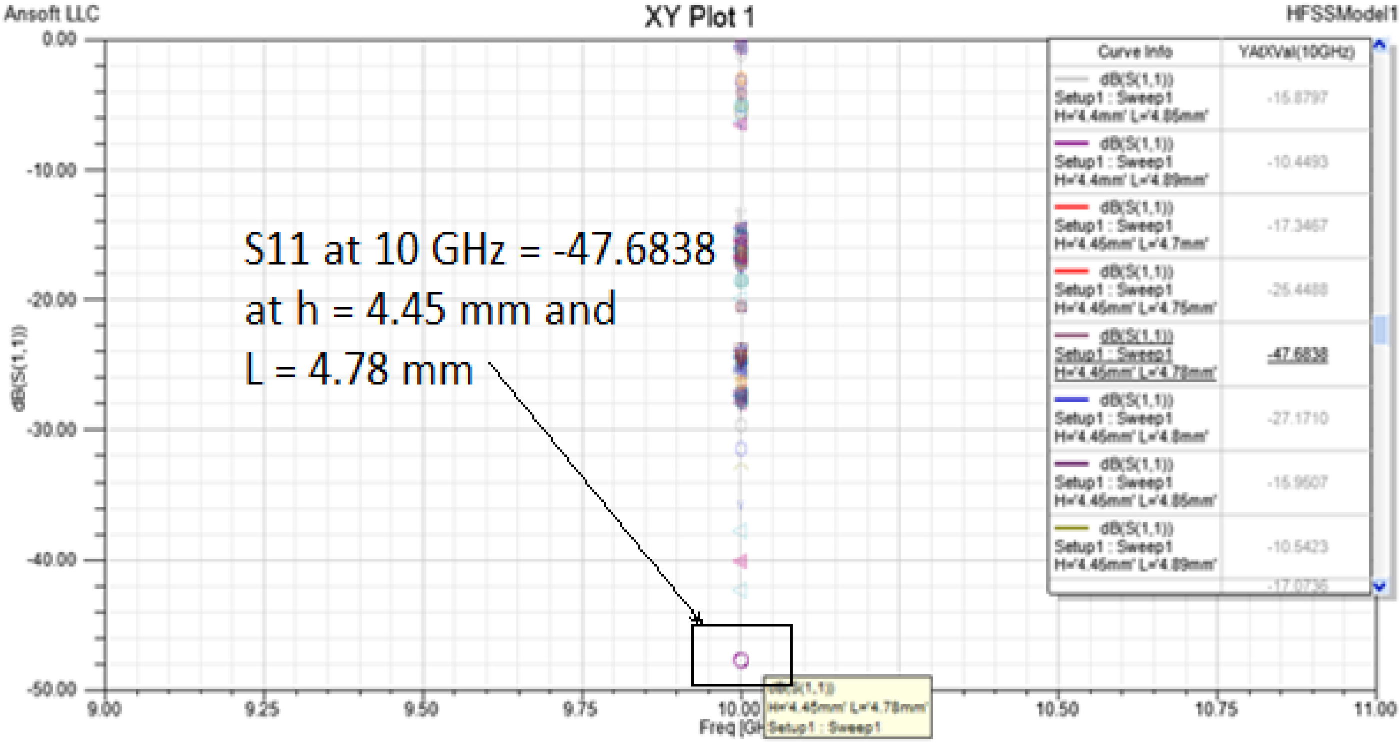

Figure 3.6: The results of S_{11} for different point where L and h_1 are varying inside antenna.

One of the best combination of "L" and "H" values that resulted lowest reflection response (S_{11}) of the coaxial feed waveguide antenna is shown in **Figure3.6**. Note that at the design frequency of *10 GHz*, the optimum values of L = 4.78 mm = $0.493\lambda_g$ and H = 4.45 mm = $0.459\lambda_g$, which results in S_{11} = -47.6838 dB. But since the available sample of the ferrite cylinders had L = 4.8 mm and H = 4.7 mm, the related S11 response for X-band (8-12 GHz) frequencies are plotted in **Figure 3.7**. It is clear from this figure that S_{11} = -24.3742 dB at 10 GHz and the -10dB impedance bandwidth of the antenna is approximately 360 MHz. The 3D radiation pattern of the 10 GHz waveguide antenna with unbiased ferrite cylinder (H_{dc} = 0 KA/m) is shown in **Figure 3.8**. The related E and H-plane radiation patterns are plotted in **Figure 3.9.**

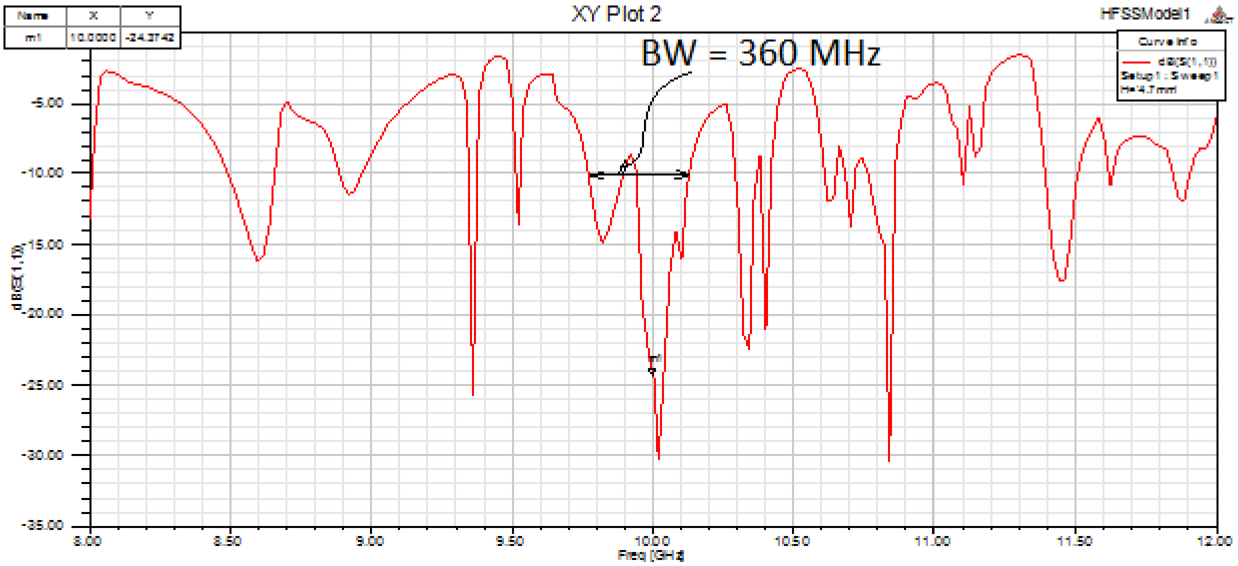

Figure 3.7: The X-band reflection response (S_{11}) of the waveguide antenna.

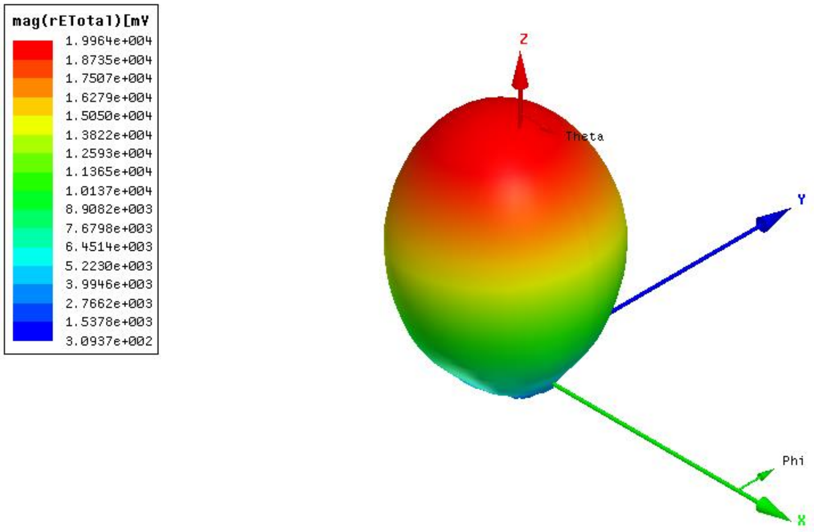

Figure 3.8: The 10 GHz radiation pattern of the antenna with unbiased ferrite cylinders.

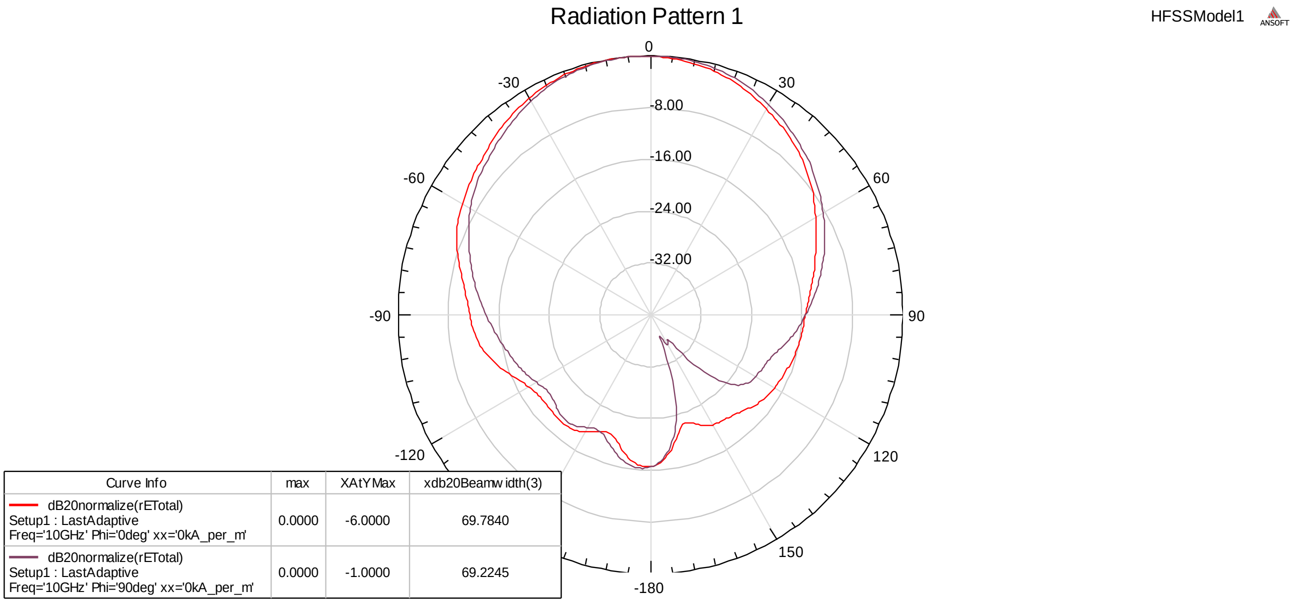

Figure 3.9: The E and H-plane radiation patterns of the antenna unbiased ferrite cylinders.

3.3.1. The effect of the feed location

Initially the probe location (h) was selected to be λ/4 away from the grounded end of the ferrite cylinder loaded circular waveguide. Then for a set probe length of L=4.8 mm, the probe height (h) is varied to observed the S11 response of the antenna. For a a=10mm waveguide loaded with b=5mm ferrite cylinder, the S11 response of the antenna for two different probe heights are plotted in **Figure 3.10**. Note that the impedance bandwidth of 360 MHz is observed for h=4.7 mm.

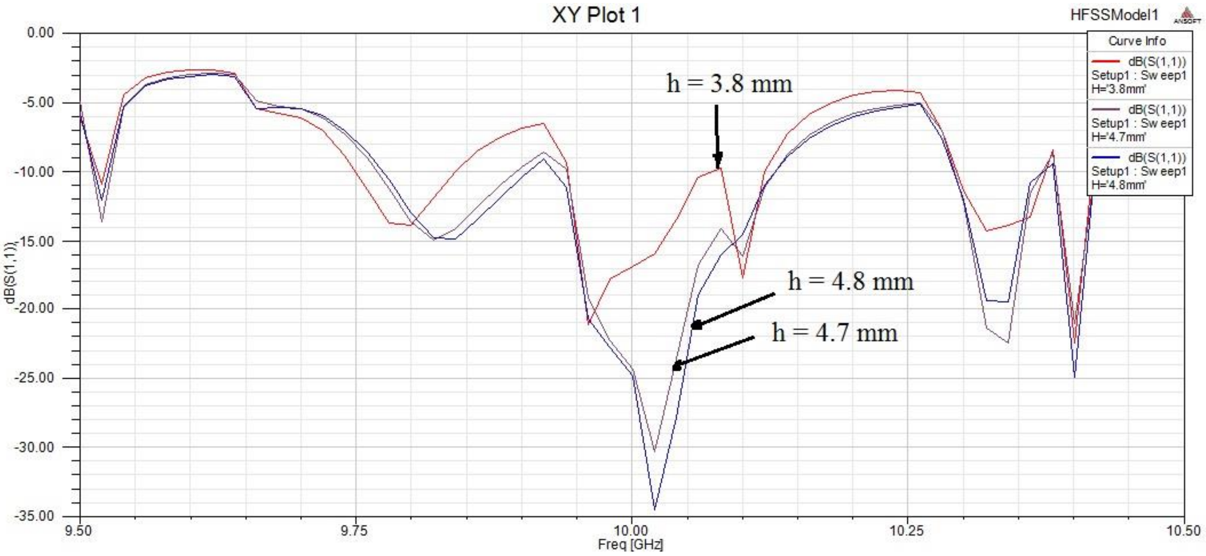

Figure 3.10: The effect of the antenna S_{11} response for changing probe location (height).

The second observation on how the S_{11} response of the antenna changes with changing probe length (L) shown in **Figure 3.11**. For a fixed probe location (height) of h=4.7 mm, it is clear from this figure that the L=4.8mm gives the best reflection response. Note that the by reducing the penetration length of the probe, the antenna impedance bandwidth can be improved at the cost of lower coupling.

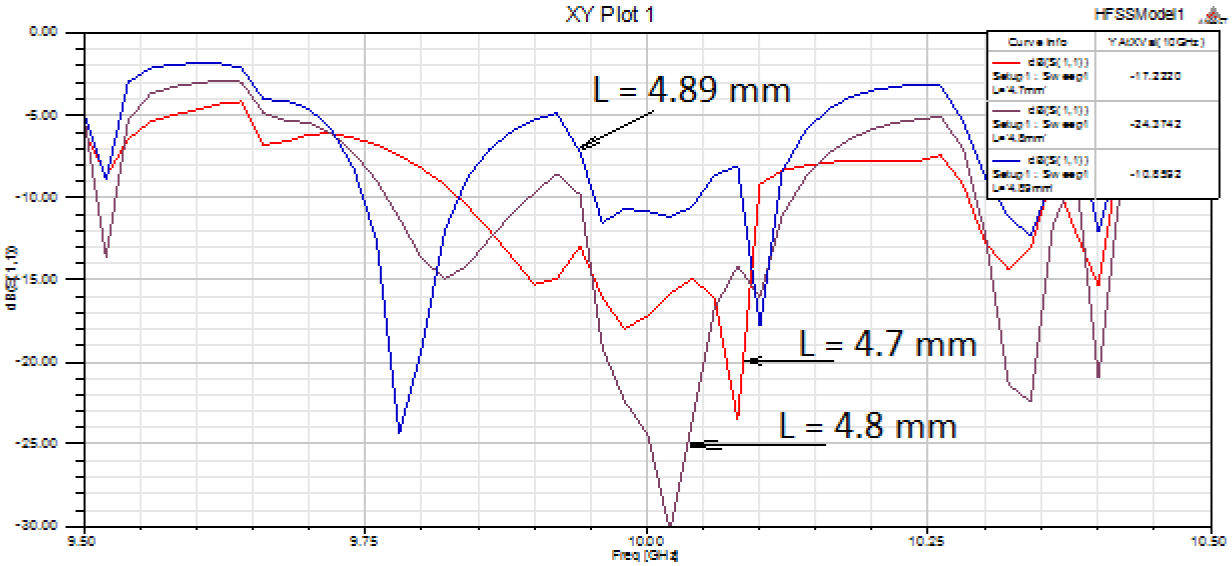

Figure 3.11: The effect of the antenna S_{11} response for changing probe penetration length (L).

3.3.2. The effect of ferrite and waveguide dimension.

Although the dimensions of the circular waveguide and ferrite cylinder is selected at the beginning of the design process, this section investigates the change in reflection response with changing dimensions waveguide or ferrite sample. This can very easily happen during in house fabrication process, as local fabrication facilities will be used to produce the prototype of the antenna. For a fixed ferrite sample with b = 5 mm, coaxial probe penetration length L = 4.8 mm and probe location h = 4.7 mm, the changes of S11 response with changing waveguide length is plotted in **Figure 3.12**. Note that impedance bandwidth of the antenna is drastically affected by changes in waveguide length (H). As expected, this changes require the probe penetration and location to be re-optimized to get best response.

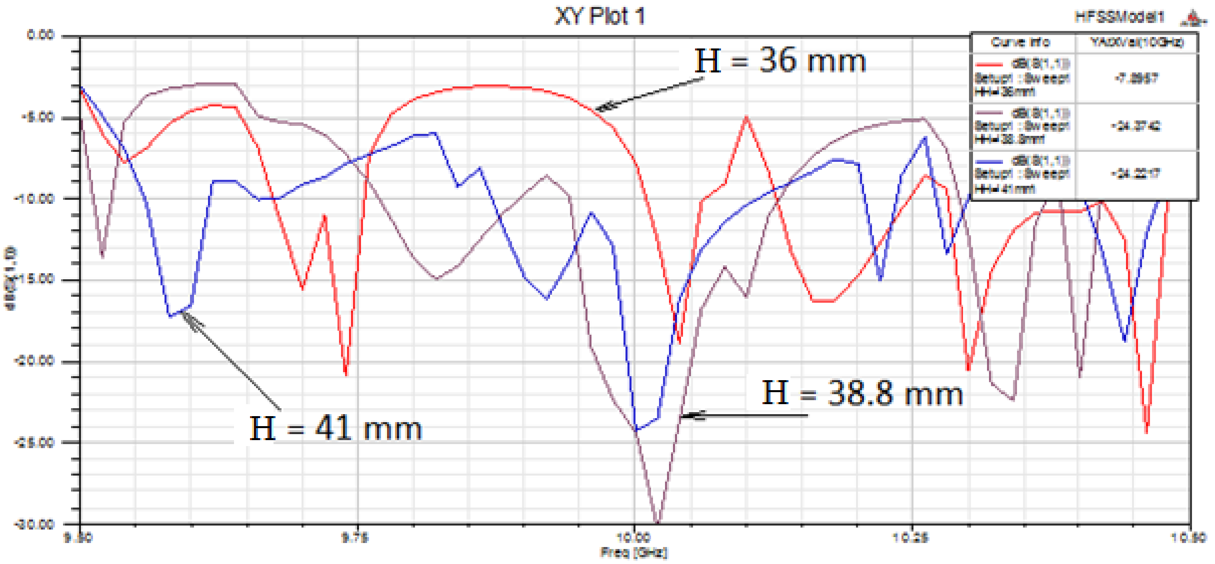

Figure 3.12: The S_{11} response of the antenna for changing waveguide length (H).

For a designed antenna with probe penetration length L = 4.8 mm, probe height h = 4.7 mm and ferrite radius b = 5 mm, the change in reflection response (S_{11}) with changing waveguide radius (a) is plotted in **Figure 3.13**. It is clear from this figure that changing waveguide radius can have a huge effect on the S_{11} response of the antenna. Note that during fabrication process, waveguide radius should be carefully monitored as this can considerably change the performance of the designed antenna. If we look to the phase constant β of the dominant mode versus radius of the waveguide, the phase constant is same for different waveguide radius as shown in **Figure 3.14** but the number of modes will propagates at 10 GHz will increase as the radius increase as shown in **Figure 3.15, Figure 3.16**and **Figure 3.17**.

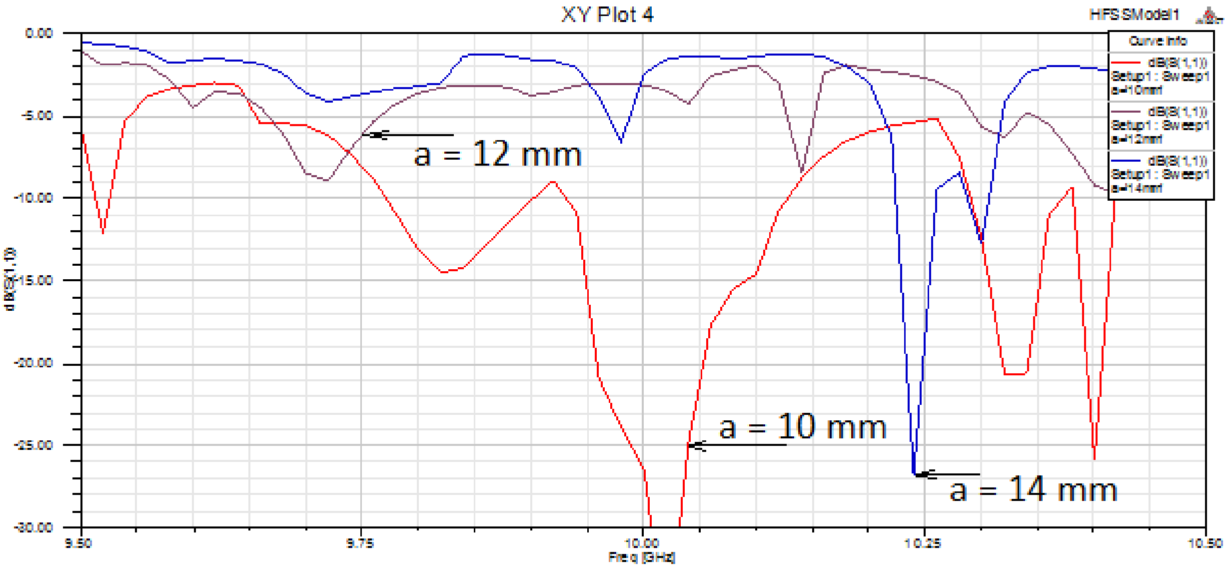

Figure 3.13: The results of S_{11} for different radius of waveguide (a) vs. frequency.

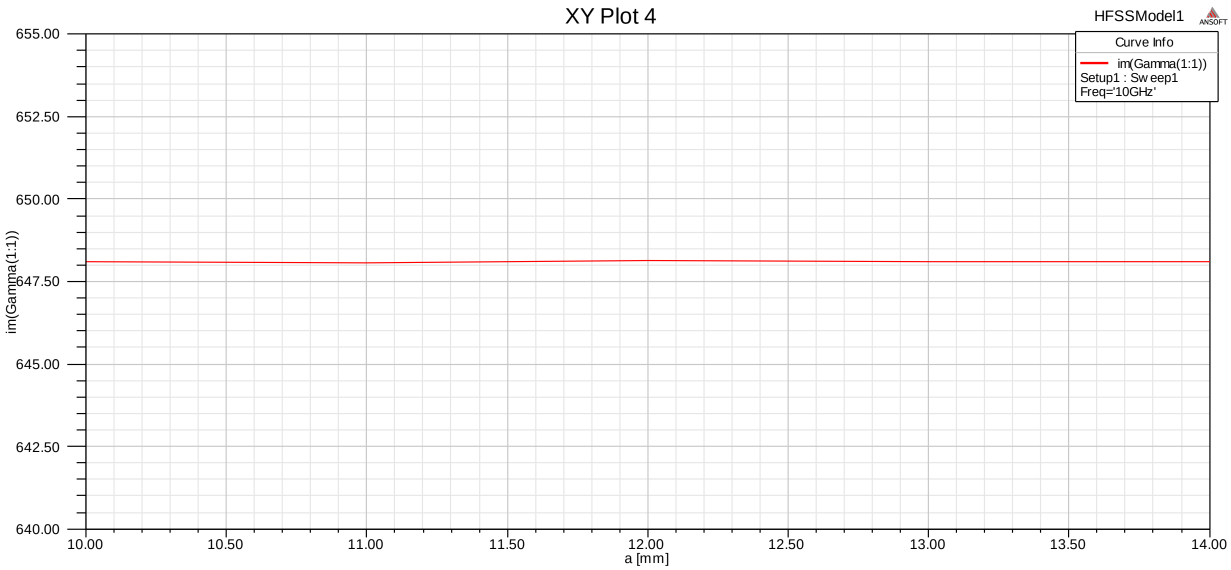

Figure 3.14: The results of β at 10 GHz vs. radius of waveguide (a).

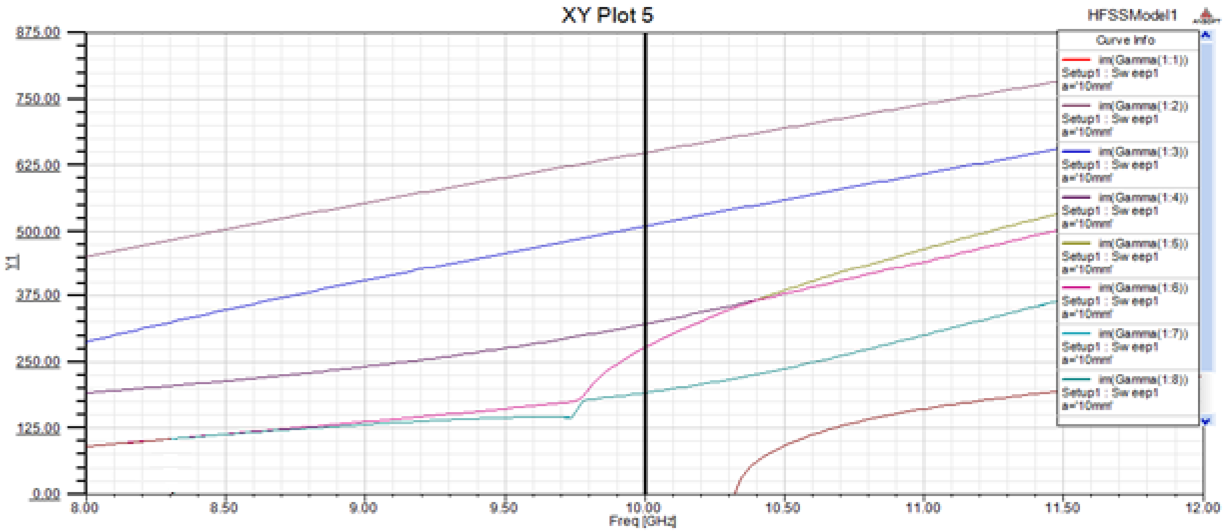

Figure 3.15: The results of β vs. frequency for radius of waveguide (a) = 10 mm.

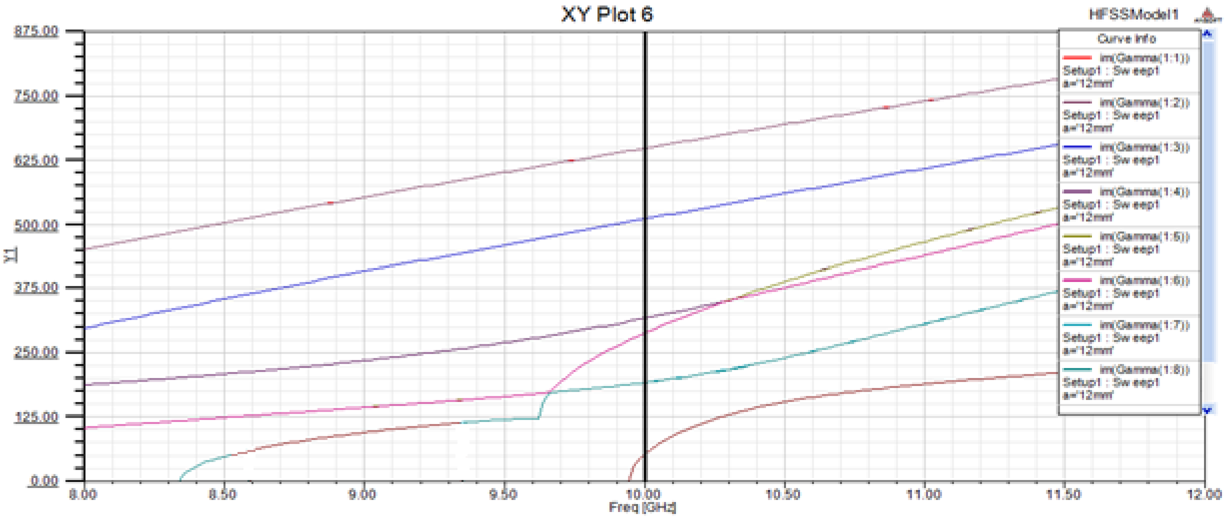

Figure 3.16: The results of β vs. frequency for radius of waveguide (a) = 12 mm.

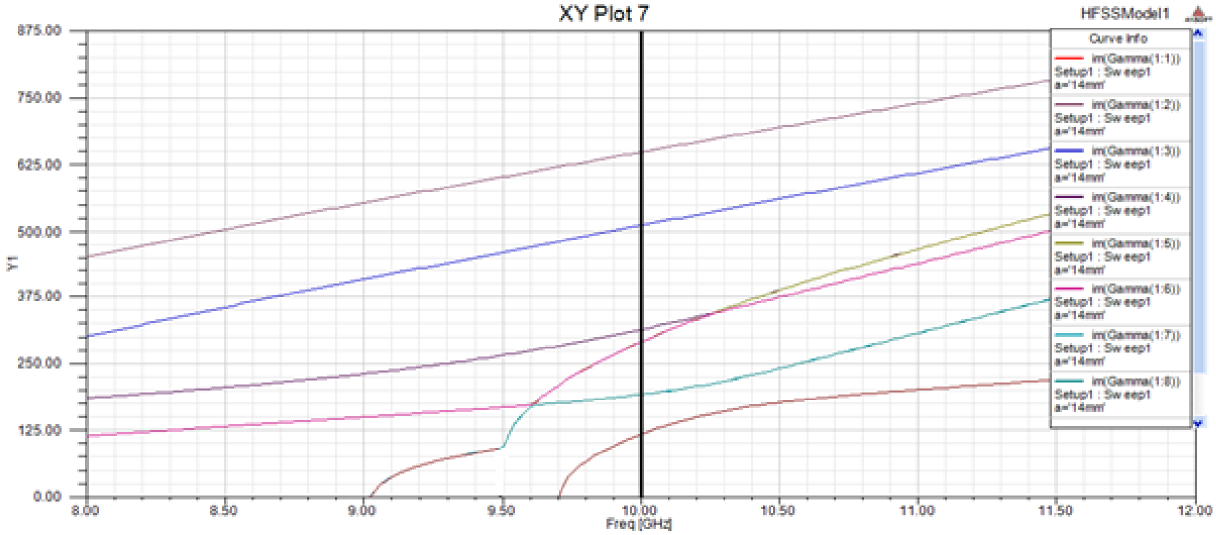

Figure 3.17: The results of β vs. frequency for radius of waveguide (a) = 14 mm.

The fifth observation is changing radius of ferrite (b), the probe is located at length L = 4.8 mm and height h = 4.7 mm and the radius of the waveguide is 10 mm. It is clear from **Figure 3.18**there is a big different by changing the radius of the ferrite (b). If we look to the phase constant β of the dominant mode versus radius of the ferrite, the phase constant will increase as the ferrite radius increase as shown in **Figure 3.19**. If we look to the wavelength $\lambda_g$of the dominant mode versus radius of the ferrite, the wavelength will decrease as the ferrite radius increase as shown in **Figure 3.20**. Theoretically, the effect of the radius of the waveguide and the radius of the ferrite has been calculated and they have the same effect found in the HFSS calculation.**Figure 3.21**shows the effect of the ferrite radius theoretically and **Figure 3.22**shows the effect of the waveguide radius theoretically.

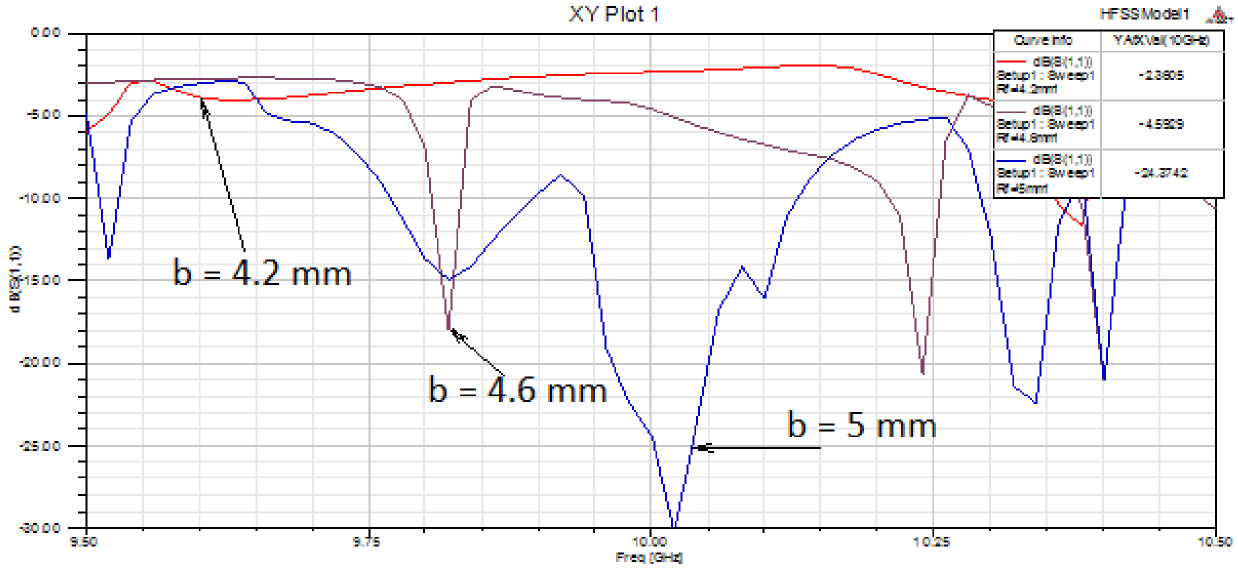

Figure 3.18: The results of S_{11} for different radius of ferrite (b) vs. frequency

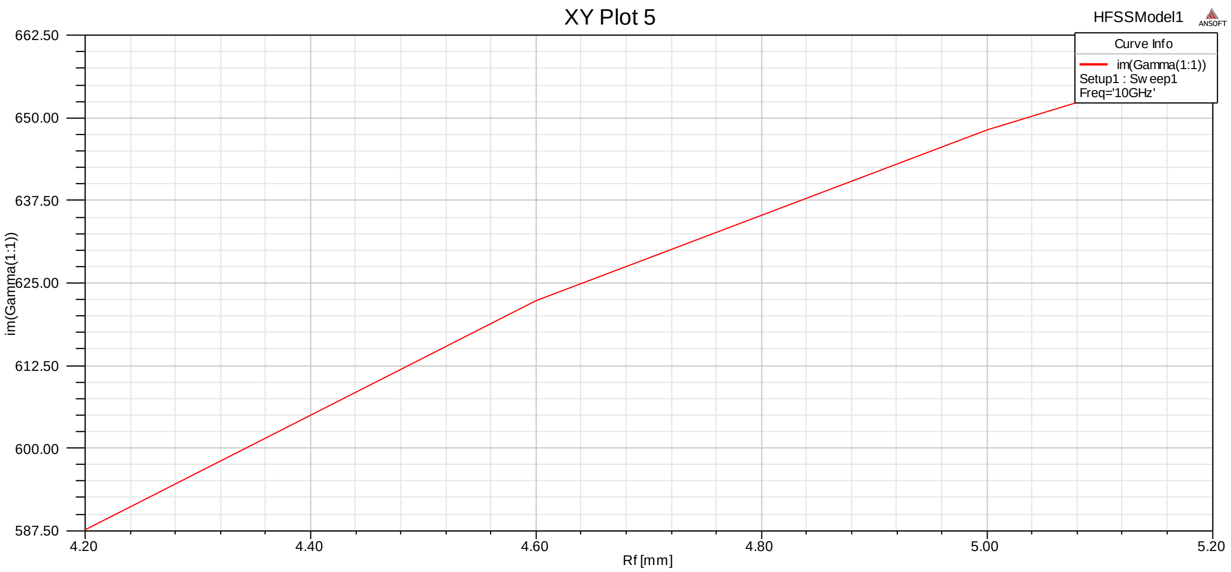

Figure 3.19: The phase constant of the dominant mode at 10 GHz vs. ferrite radius

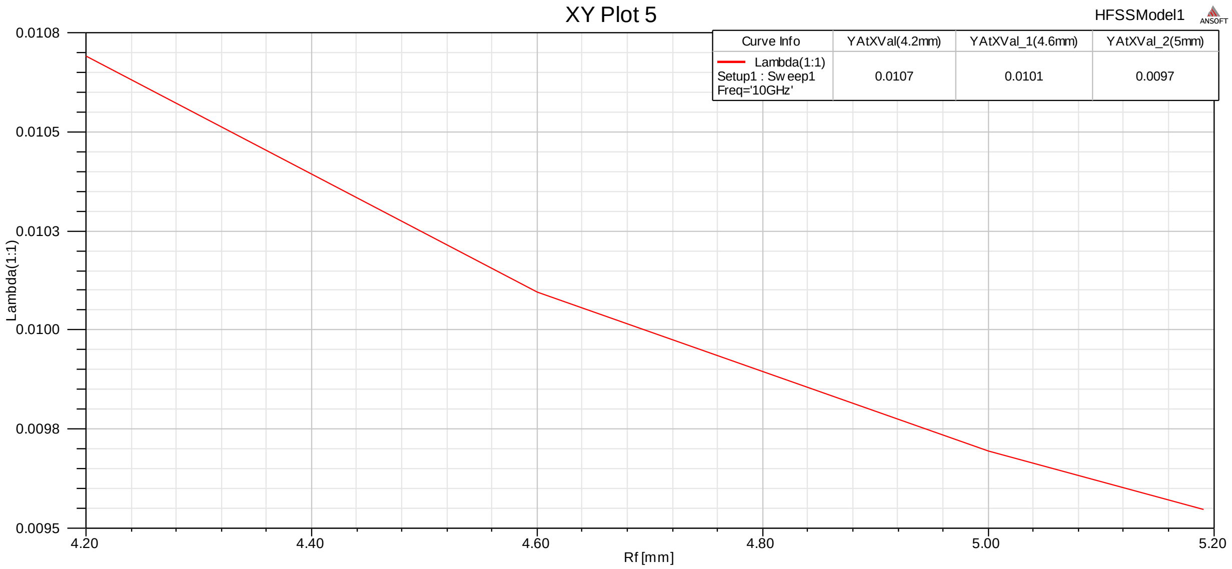

Figure 3.20: The wavelength of the waveguide of the dominant mode at 10 GHz vs. ferrite radius

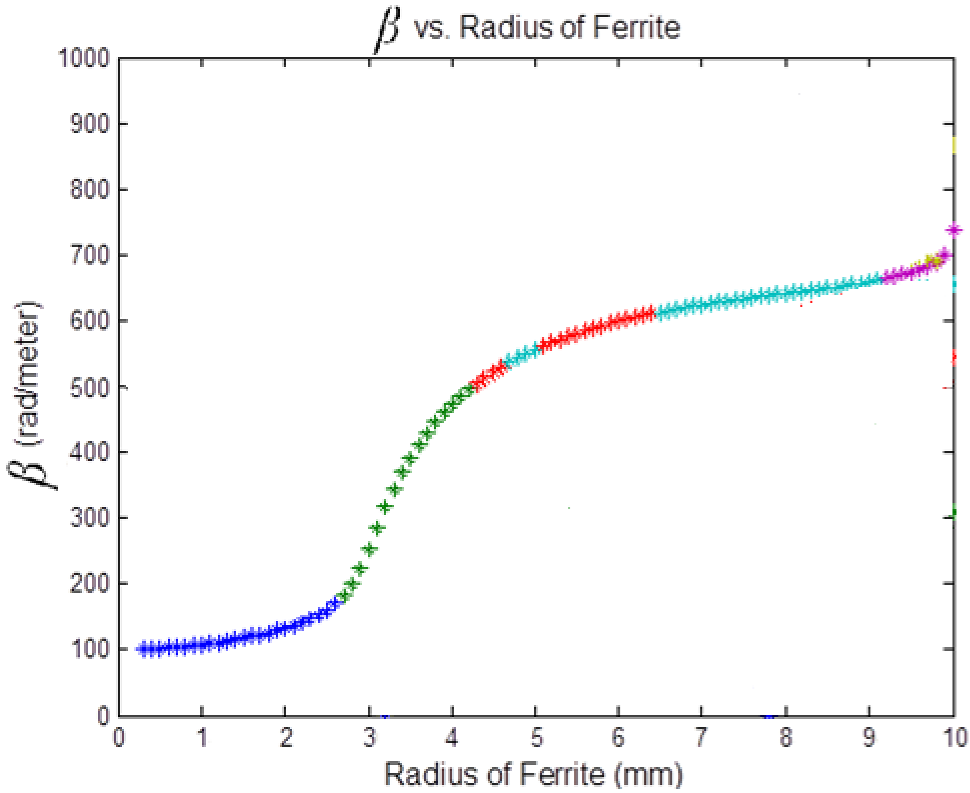

Figure 3.21: The results of β at 10 GHz vs. radius of ferrite (b).Theatrically.

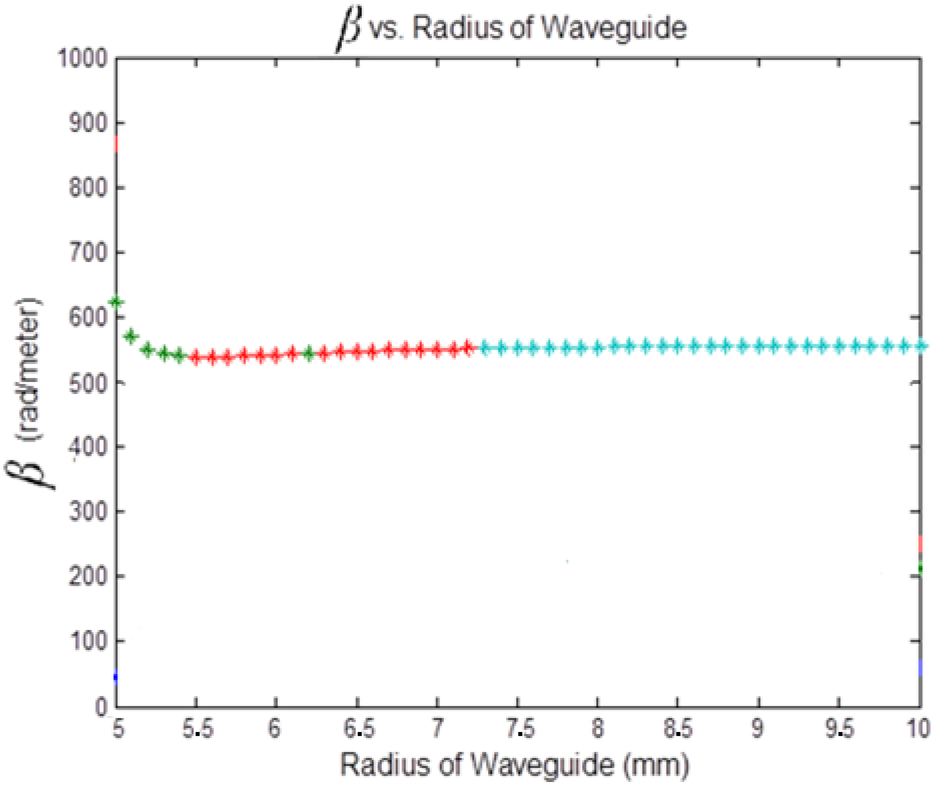

Figure 3.22: The results of β at 10 GHz vs. radius of waveguide (a).Theatrically.

3.3.3. The effect of magnetizing the ferrite cylinder

In this section, how the antenna properties are affected through biasing the ferrite cylinders are discussed. The centrally loaded ferrite cylinder within the circular waveguide is axially magnetized in "+" and "-" directions of the Z-axis, as shown in **Figure 3.23**. The range of the variation of the external biasing field is from 0 KA/m (unbiased) to 380 KA/m (0.478 **Tesla)** with steps of 10 KA/m (0.126 **mTesla)**. The optimum dimensions of the designed antenna with unbiased ferrite cylinder, obtained in the previous section are as follows:

1- The height of the antenna "H" is 38.8 mm.
2- The radius of the antenna "a" is 10 mm.
3- The radius of the ferrite "b" is 5 mm.
4- The operating frequency "f" is 10 GHz.
5- The coaxial feed length "L" is 4.8 mm.
6- The coaxial feel height "h" is 4.7 mm.

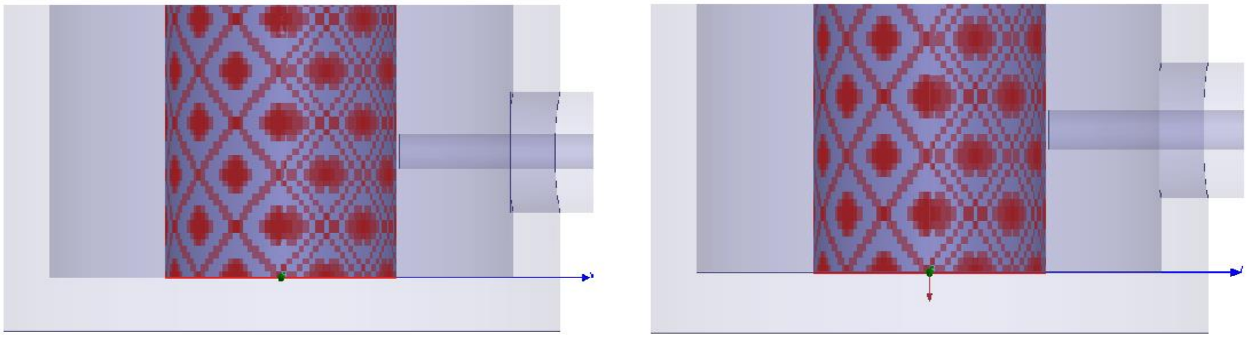

(a) (b)

Figure 3.23: Arrow in 'z-axis' shows the direction of the biasing (a) '+z-axis' (b) '-z-axis'.

The efficiency of the optimized circular waveguide antenna loaded with axially magnetized ferrite cylinder is plotted in **Figure 3.24**. This simulated figure shows that external biasing needed for beam scanning is also associated with lossy regions. These losses are mainly due to ferromagnetic resonance of the ferrite cylinder that occurs between external biasing field of 250 to 330 KA/m. In addition other lossy regions related to external magnetizing of the ferrite loaded waveguide antenna is also shown in this figure.

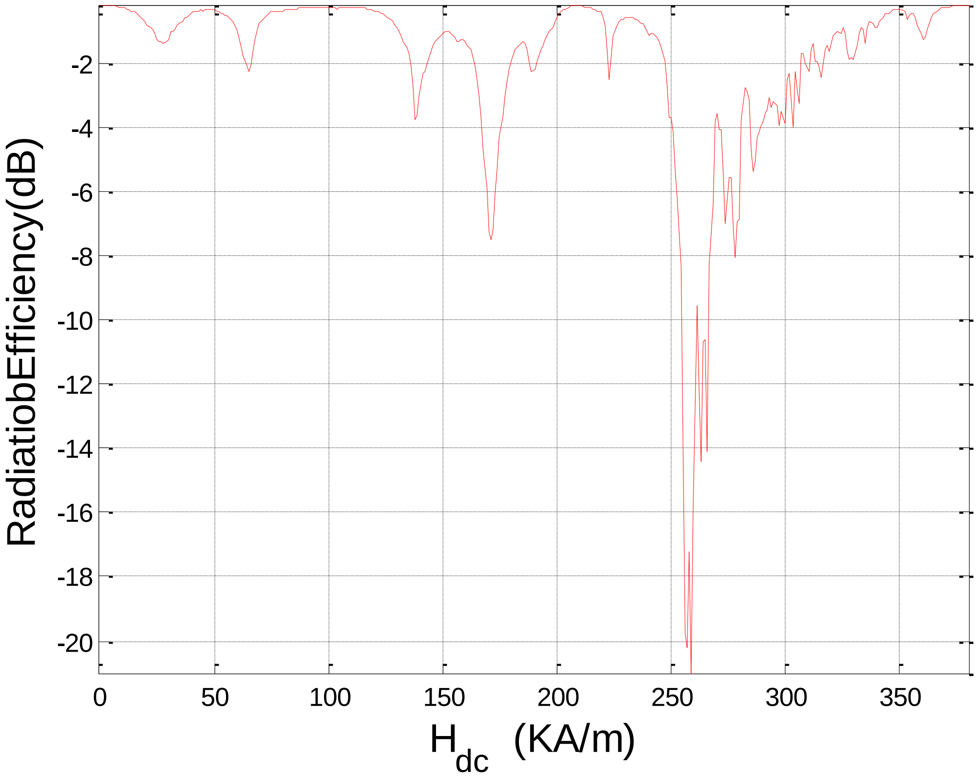

Figure 3.24: The efficiency of the antenna vs. the external magnetic field H $_{dc}$.

The gain and the directivity of an antenna are also important parameters to measure its performance. The gain of the ferrite loaded waveguide antenna versus changing magnetizing field is shown in **Figure 3.25**. Since the antenna gain varies with external biasing field, care should be taken in selecting magnetizing field required to achieve external biasing. The directivity of the designed antenna versus external biasing field of the ferrite cylinder is plotted in **Figure 3.26**.

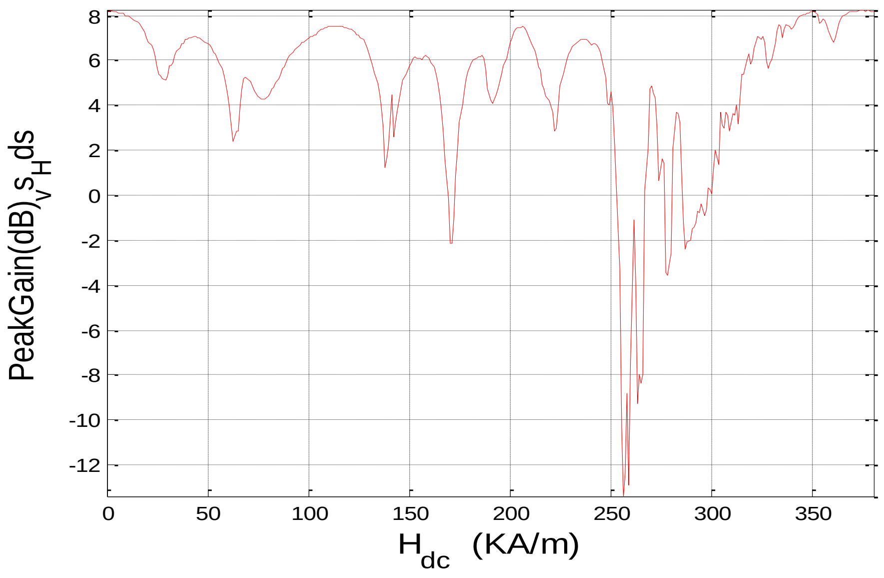

Figure 3.25: The gain of the antenna vs. the external magnetic field H $_{dc}$.

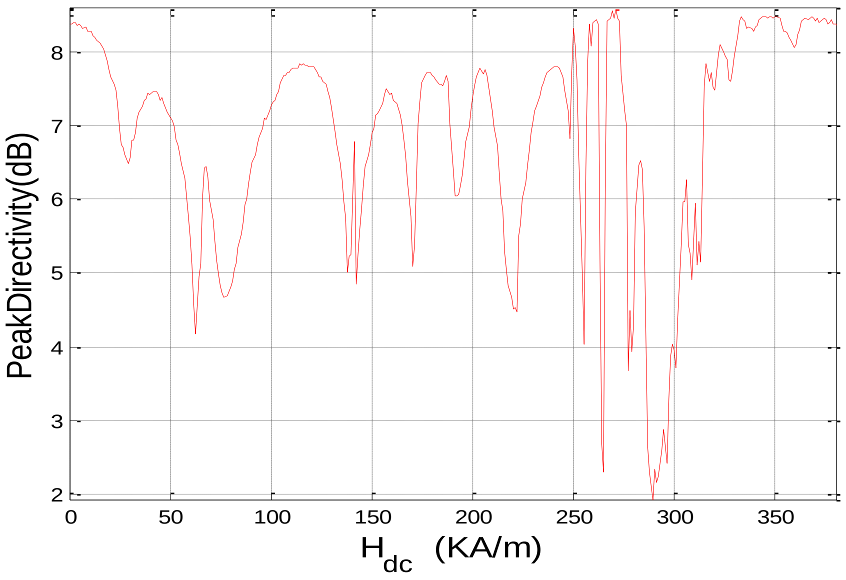

Figure 3.26: The directivity of the antenna vs. the external magnetic field H $_{dc}$.

3.4 Beam Scanning Properties of the Ferrite Loaded Waveguide Antenna

After investigating the effects of external magnetizing field on the gain, directivity and efficiency of the ferrite loaded waveguide antenna, how external magnetizing can be used in scanning the main beam is demonstrated here. The region in from of the radiating end of the waveguide is divided into two parts. The first part discusses the scanning mechanism in the directions towards ‘x’ and ‘y’ axis and the second part discuss scanning in other directions of the x-y plane. **Figure 3.27** illustrates the scanning axis towards ‘x’ and ‘y’, which also represents φ = 0° and 90° directions, respectively. For a magnetizing field (Hdc) applied in ‘+z-axis’, **Figure 3.28** shows the beam direction in the φ = 0° plane and θ = -30°, 0° and 34° for Hdc = 142 KA/m, 219 KA/m and 355 KA/m, respectively.

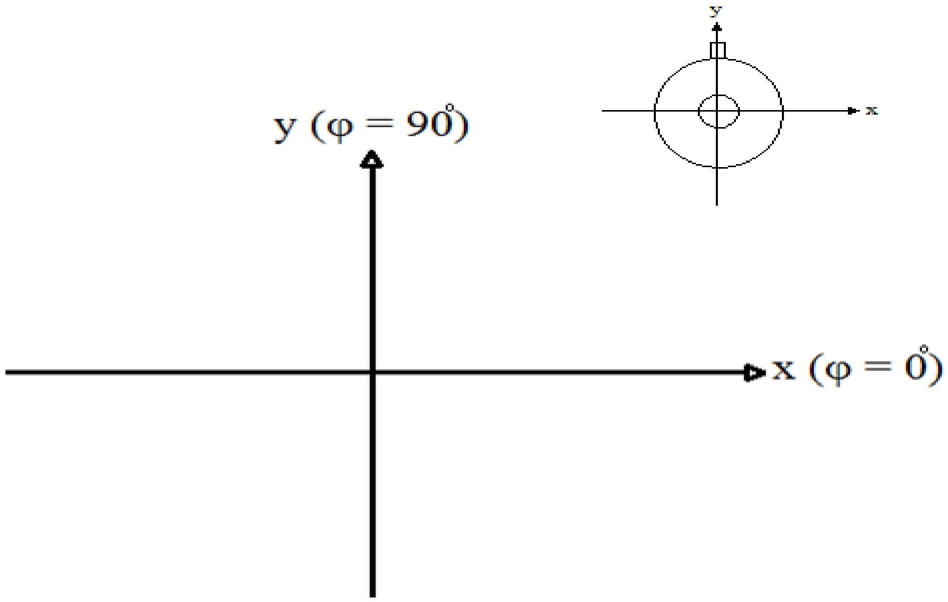

Figure 3.27: The transverse radiating plane of the waveguide antenna (also shown in figure).

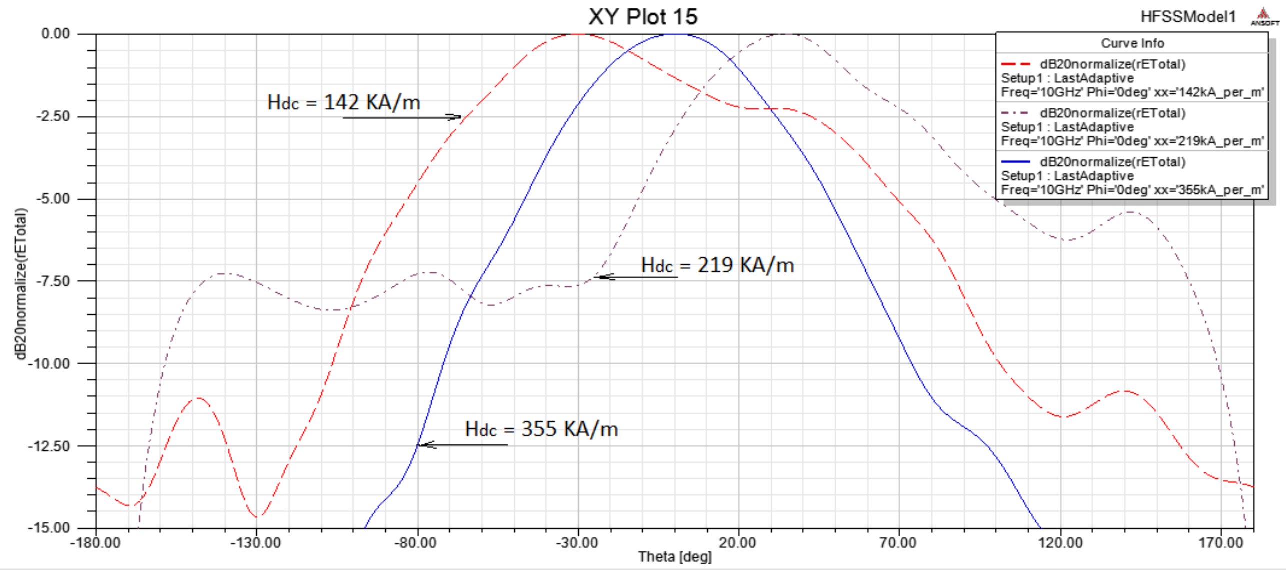

Figure 3.28: Scanning the antenna beam in φ=0° plane with changing magnetizing field (H_{dc}).

For the beam scanning in the φ = 90° plane with variable magnetizing field in '+z-axis', **Figure 3.29** illustrates that the main beam directions of θ = -35°, 0° and 37° are achieved using Hdc = <u>63</u> KA/m, <u>355</u> KA/m and <u>171</u> KA/m, respectively.

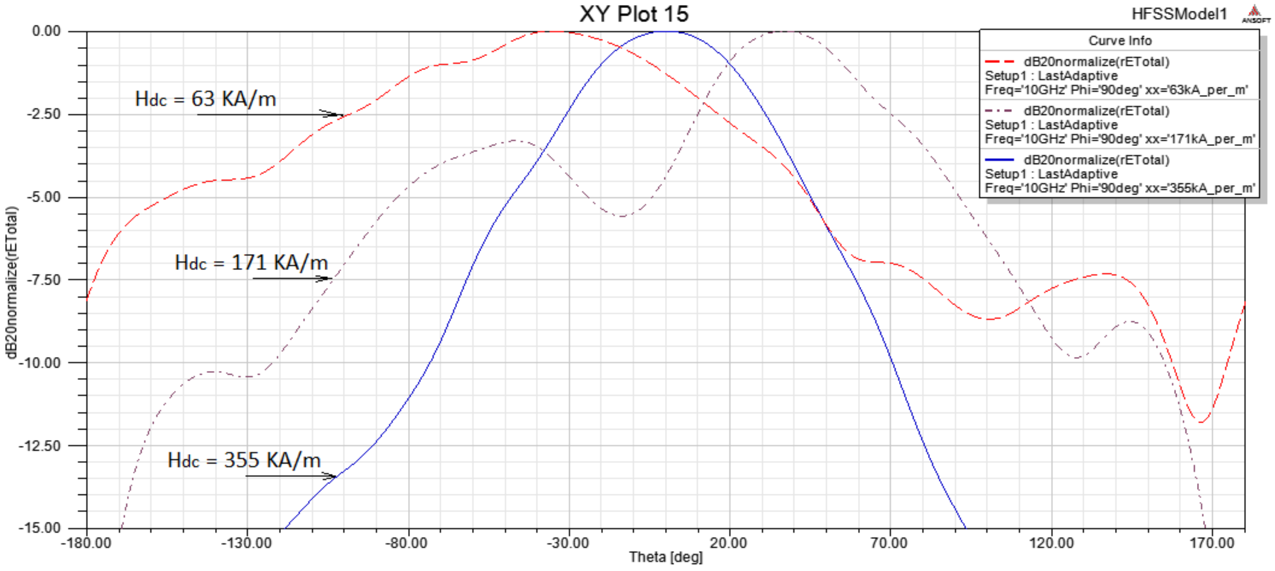

Figure 3.29: Scanning the antenna beam in φ=90° plane with changing magnetizing field (H_{dc})

In the second part of this section, the beam scanning for all planes in the transverse plane is represented for the biasing in the '+z - axis'. Based on the beam-width of the main radiating lobe, which is around 65°, the transverse plane is divided into 9 regions. **Figure 3.30** shows these regions, where region 1 to 8 is limited by a range of phi angle in XY- plane, as tabulated in **Table 3.1**.

Table 3.1: The 360 ^{o} angle phi (φ) is divided into 8 regions.

Region (R)	1	2	3	4	5	6	7	8
Phi angle in (degree)	330 - 30	30 - 60	60 - 120	120 - 150	150 - 210	210 - 240	240 - 300	300-330

.

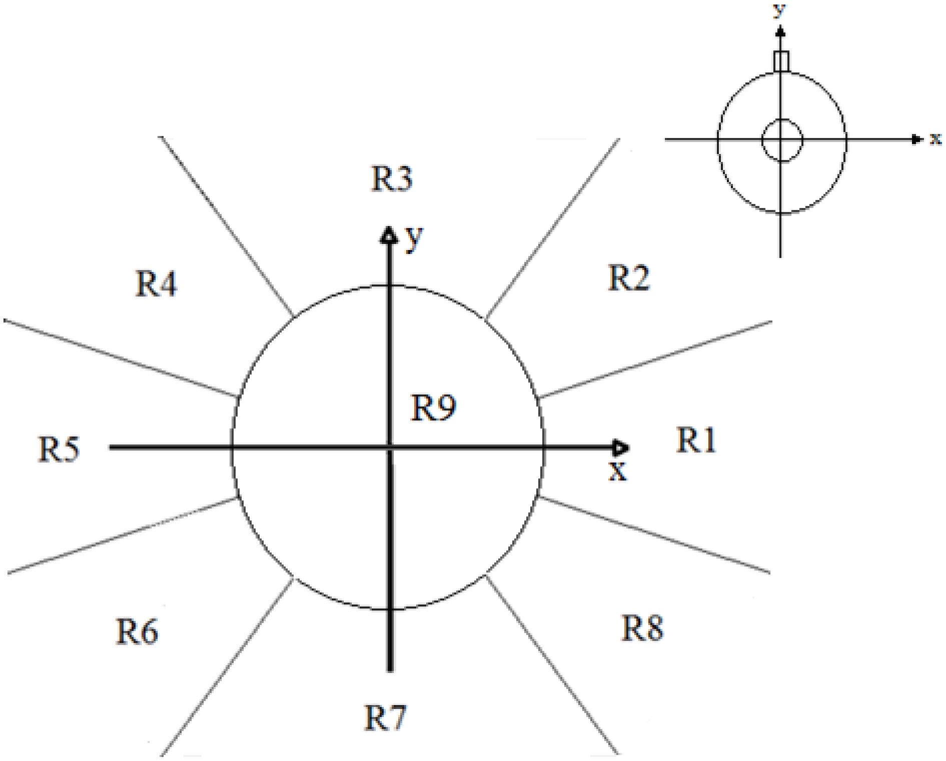

Figure 3.30: The far field radiating regions in the transverse plane.

For each region, the direction of the radiated beam (θ) can be scanned through changing the externally applied magnetizing field (Hdc). But for a selected values of magnetizing field, the direction of the radiation (θ) can be scanned within the same region. For example, for changing H_{dc} from 200 KA/m to 208 KA/m, the radiation stays within region1. **Table 3.2** to **Table 3.10** shows the range of the applied external magnetic fields need to scan the main beam within the region 1 to region 8, respectively.

Table 3.2: The radiation angle (Theta) for the external bias (H_{dc}) in the +z_ direction and the magnitude in dB within the region (R1).

Biasing in +z (R=1)		
H_{dc} (KA/m)	θ (°)	mag. (dB)
135	15	21.66065
217	31	21.96774

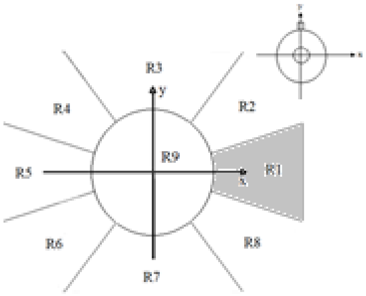

Table 3.3: The radiation angle (Theta) for the external bias (H_{dc}) in the +z_ direction and the magnitude in dB within the region (R2).

Biasing in +z (R=2)		
H_{dc} (KA/m)	θ (°)	mag. (dB)
116	11	24.41605
174	20	15.64097
216	28	22.39005

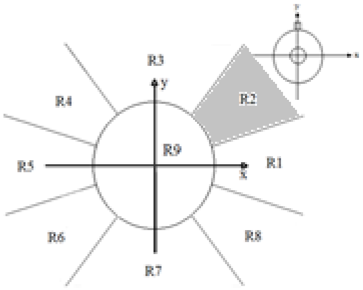

Table 3.4: The radiation angle (Theta) for the external bias (H_{dc}) in the +z_ direction and the magnitude in dB within the region (R3).

Biasing in +z (R=3)		
H dc (KA/m)	θ (°)	mag. (dB)
83	23	20.27066
115	11	24.36874
172	29	13.29531
178	13	18.65702
185	9	21.29766

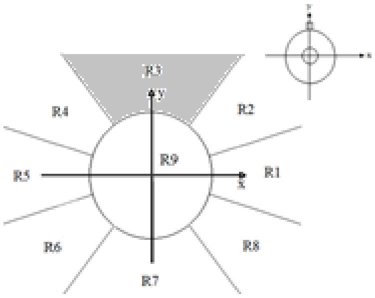

Table 3.5: The radiation angle (Theta) for the external bias (H_{dc}) in the +z_ direction and the magnitude in dB within the region (R4).

Biasing in +z (R=4)		
H dc (KA/m)	θ (°)	mag. (dB)
24	11	23.59351
64	17	18.41512
76	27	20.0398

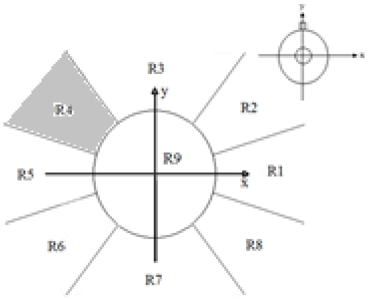

Table 3.6 The radiation angle (Theta) for the external bias (H_{dc}) in the +z_ direction and the magnitude in dB within the region (R5).

Biasing in +z (R=5)		
H dc (KA/m)	θ (°)	mag. (dB)
0	6	25.96356
68	13	20.91566
73	23	20.56661
142	30	17.68139

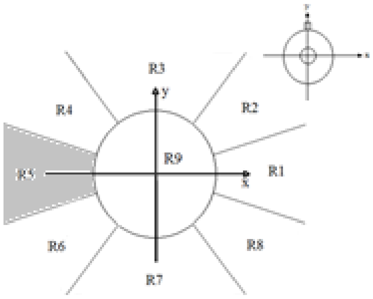

Table 3.7: The radiation angle (Theta) for the external bias (H_{dc}) in the +z_ direction and the magnitude in dB within the region (R6).

Biasing in +z (R=6)		
H dc (KA/m)	θ (°)	mag. (dB)
188	5	21.73476
249	13	18.17157

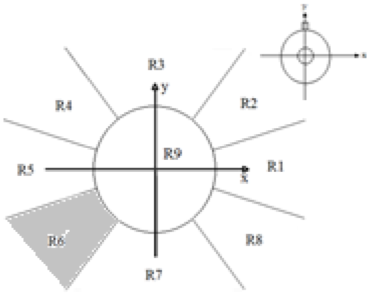

Table 3.8: The radiation angle (Theta) for the external bias (H_{dc}) in the +z_ direction and the magnitude in dB within the region (R7).

Biasing in +z (R=7)		
H dc (KA/m)	θ (°)	mag. (dB)
38	8	24.41783
54	17	23.79501
63	35	18.36586

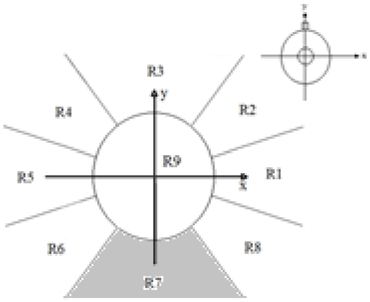

Table 3.9: The radiation angle (Theta) for the external bias (H_{dc}) in the +z_ direction and the magnitude in dB within the region (R8).

Biasing in +z (R=8)		
H dc (KA/m)	θ (°)	mag. (dB)
140	45	17.36638
222	24	19.32519
225	15	19.39336
237	9	20.67014

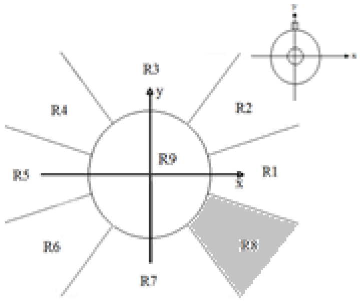

Table 3.10: The radiation angle (Theta) for the external bias (H_{dc}) in the +z direction and the magnitude in dB within the region (R9).

Biasing in +z (R=9)		
H_{dc} (KA/m)	θ (°)	mag. (dB)
31	1	23.12593
33	4	23.3635
355	0	25.32311
358	3	24.40497

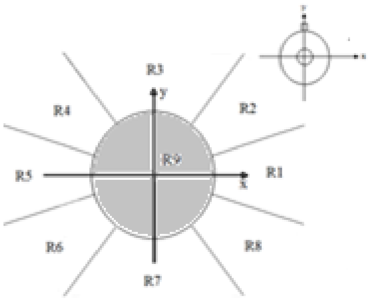

Based on the selected direction of the target in each region, the main beam can be focused with required external biasing fields, as mentioned in above tables. Note that

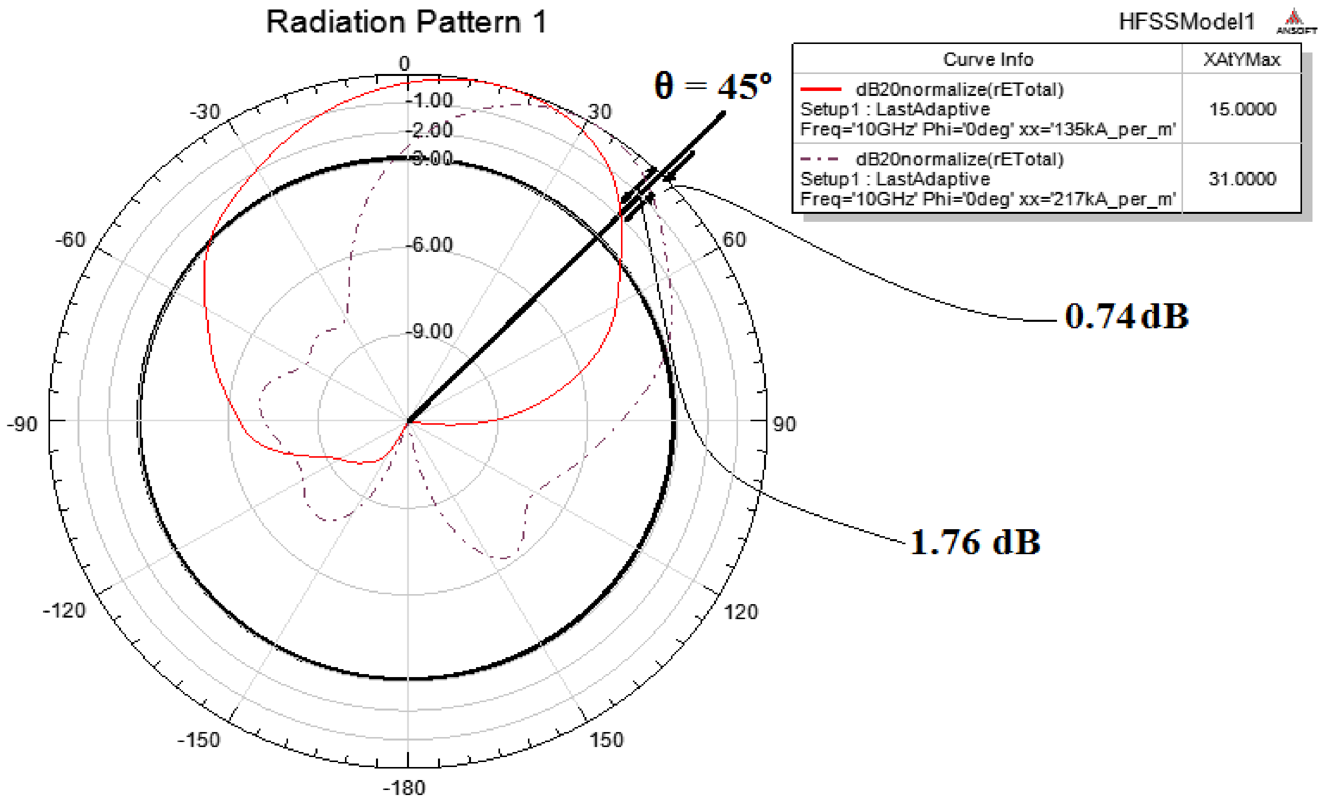

Figure 3.31: The different between two external magnetic fields in same region (R1).

although the main beam-width is 70°, by pointing the main beam in small angle steps will allow us to direct more power in the designed direction. For example, **Figure 3.31** shows two radiations for two different external magnetic fields in region 1 (R1). Note that in the selected direction of θ = 45°, both of the radiated beams can establish communication as it is within the beamwidth of both radiated beams. But the radiated beam for H_{dc} = 217 KA/m can transmit/receive more power (≅1 dB) in that desired direction compared to the radiation resulted for external biasing of H_{dc} = 135 KA/m.

In the third part of this section, the beam scanning for all directions of the transverse x-y plane are represented for the biasing in the '-z – axis'. **Table 3.11** to **Table 3.19** show same of the applied external magnetic field with the direction of the radiation for the region 1 to region 8, respectively.

Table 3.11: The radiation angle (Theta) for the external bias (H_{dc}) in the -z_ direction and the magnitude in dB within the region (R1).

Biasing in -z (R=1)		
H_{dc} (KA/m)	**θ (°)**	**mag. (dB)**
68	12	20.78549
73	24	20.53324
143	30	18.23279

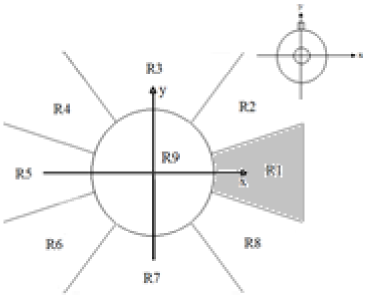

Table 3.12: The radiation angle (Theta) for the external bias (H_{dc}) in the -z_ direction and the magnitude in dB within the region (R2).

Biasing in -z (R=2)		
H dc (KA/m)	θ (°)	mag. (dB)
25	11	23.16287
65	14	18.5216
76	29	19.97433

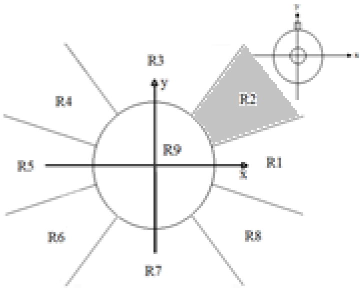

Table 3.13: The radiation angle (Theta) for the external bias (H_{dc}) in the -z_ direction and the magnitude in dB within the region (R3).

Biasing in -z (R=3)		
H dc (KA/m)	θ (°)	mag. (dB)
84	21	20.434
89	17	21.46765
115	10	24.36457
172	33	13.26284
178	12	18.68665
185	9	21.37751

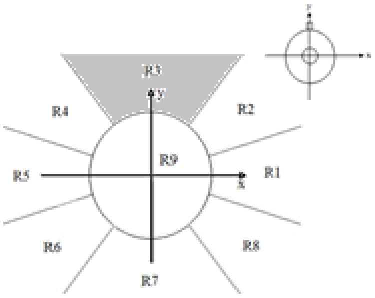

Table 3.14: The radiation angle (Theta) for the external bias (H_{dc}) in the -z_ direction and the magnitude in dB within the region (R4).

Biasing in -z (R=4)		
H dc (KA/m)	**θ (°)**	**mag. (dB)**
119	9	24.55065
174	20	15.672
217	30	21.7846

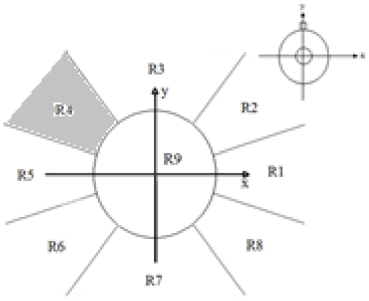

Table 3.15: The radiation angle (Theta) for the external bias (H_{dc}) in the -z_ direction and the magnitude in dB within the region (R5).

Biasing in -z (R=5)		
H dc (KA/m)	**θ (°)**	**mag. (dB)**
133	14	22.8765
219	32	20.8056

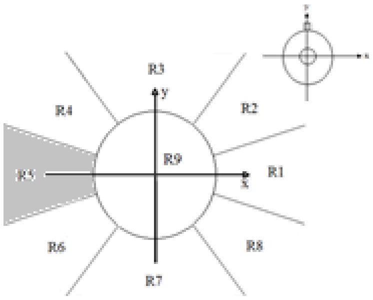

Table 3.16: The radiation angle (Theta) for the external bias (H_{dc}) in the -z_ direction and the magnitude in dB within the region (R6).

Biasing in -z (R=6)		
H_{dc} (KA/m)	θ (°)	mag. (dB)
139	46	16.39679
221	33	19.81222
225	15	19.38563
237	9	20.68306

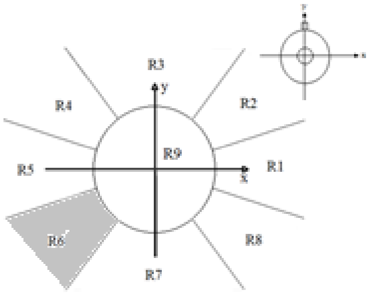

Table 3.17: The radiation angle (Theta) for the external bias (H_{dc}) in the -z_ direction and the magnitude in dB within the region (R7).

Biasing in -z (R=7)		
H_{dc} (KA/m)	θ (°)	mag. (dB)
38	8	24.47925
54	16	23.76011
61	31	20.34328
63	42	18.16126

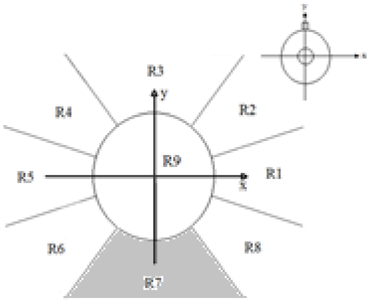

Table 3.18: The radiation angle (Theta) for the external bias (H_{dc}) in the -z_ direction and the magnitude in dB within the region (R8).

Biasing in -z (R=8)		
H_{dc} (KA/m)	θ (°)	mag. (dB)
45	10	24.72441
60	22	21.18072
249	14	18.27203
320	10	22.9095

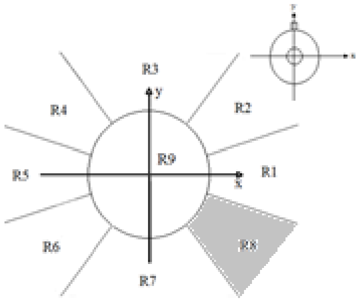

Table 3.19: The radiation angle (Theta) for the external bias (H_{dc}) in the -z_ direction and the magnitude in dB within the region (R9).

Biasing in -z (R=9)		
H_{dc} (KA/m)	θ (°)	mag. (dB)
31	2	22.88661
33	5	23.55162
355	1	25.30057
358	3	24.35368

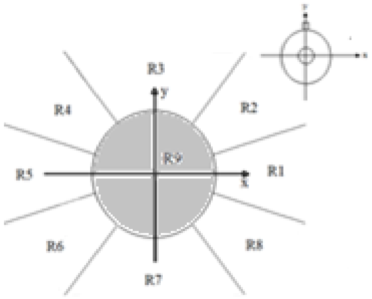

From the above tables, there is a relationship between the positive biasing and the negative biasing for a specific applied external magnetic field. For example, for a given H_{dc}, if the region of the radiation was region 'A' for the positive biasing, by change the direction of the biasing "negative biasing" for the same H_{dc}, the radiation will be in region 'B'. **Table 3.20** shows the relation between the radiation regions of the positive biasing and the negative biasing where each region has a fixed applied external magnetic felid. **Figure 3.32**shows one of these relations. The selected external biasing is H_{dc} = 142 KA/m where by applying the positive biasing the direction of the beam is at R.1 and just by change the direction of the biasing to in the negative direction the beam will be in R.5.

Table 3.20: The relationship between positive and negative biasing.

Positive biasing	R1	R2	R3	R4	R5	R6	R7	R8	R9
Negative biasing	R5	R4	R3	R2	R1	R8	R7	R6	R9

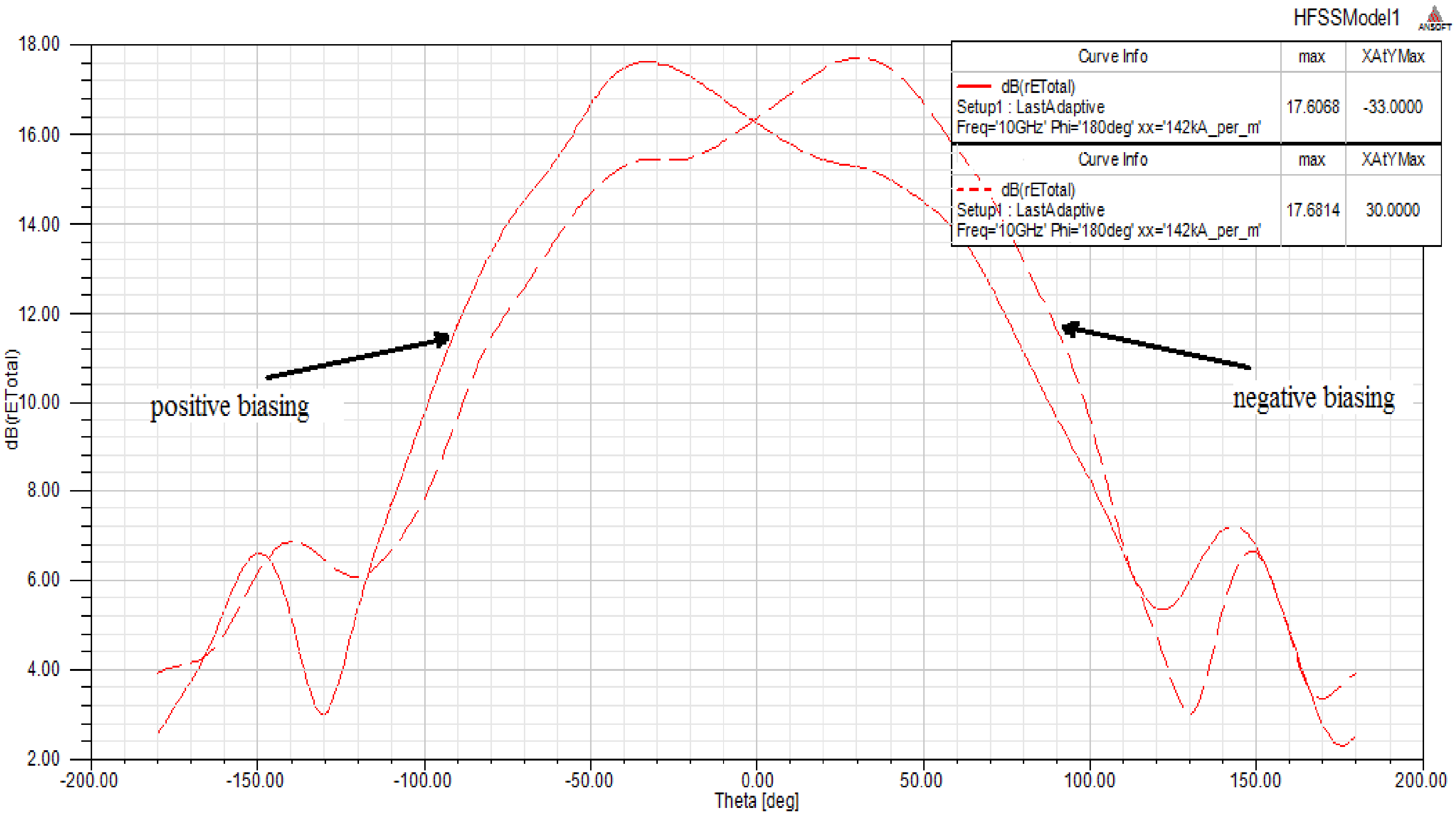

Figure 3.32: The relationship between positive and negative biasing for H_{dc} = 142 KA/m.

3.5 Directivity Enhancement using Meta-material superstrate

By using consept of the cavity respnance, a meta material inspired structure can be used as a superstrate to increase the directivity of the designed antenna. According to a structure in reference [26], the meta material superstrate is designed and used for directivity increase for an operating frequency of 12 GHz and guide wavelength 'λ = 24.98 mm'. By scaling the designed superstrate for an operating frequency of 10 GHz and for the waveguide dimensions of R=10mm, a modified superstrate can be designed for enhancing the directivity of the designed waveguide antenna of our work. **Figure 3.33** and **Figure 3.34** show the software model of the ferrite loaded waveguide antenna with meta-material superstrate. Note that the designed superstrate is made of square grids including the thickness of the copper (y) is 0.3042λ, the thickness of the copper (x) is 0.022λ, the space between layers (t) is 0.3803λ and the side of the square (b) is 2.402λ.

In **Figure 3.35**, the radiation pattern of the antenna without superstrate is reproduced for zero magnetic biasing ($H_{dc} = 0$), which demonstrates a directivity of around 8.3 dB and a beam-width of 70°. Now after introducing the meta-material

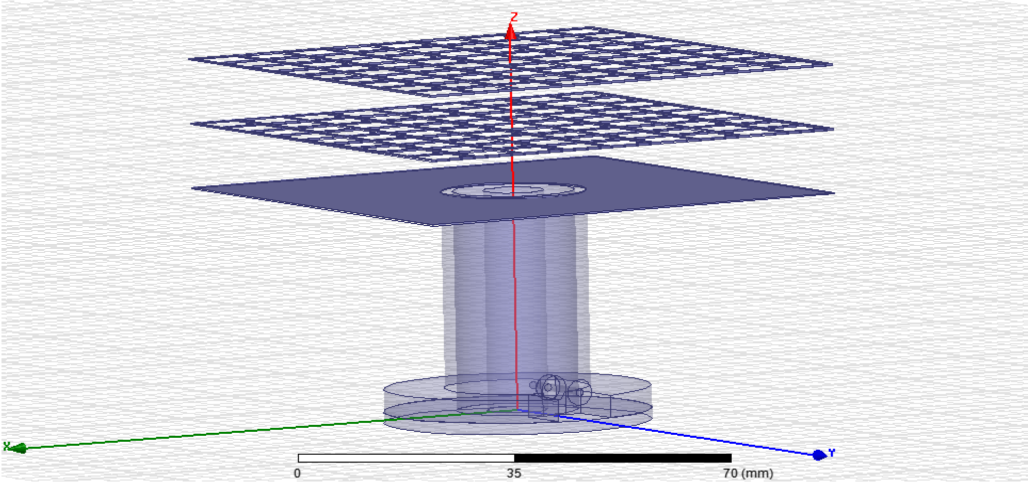

Figure 3.33: Ferrite loaded antenna with meta-material superstrate.

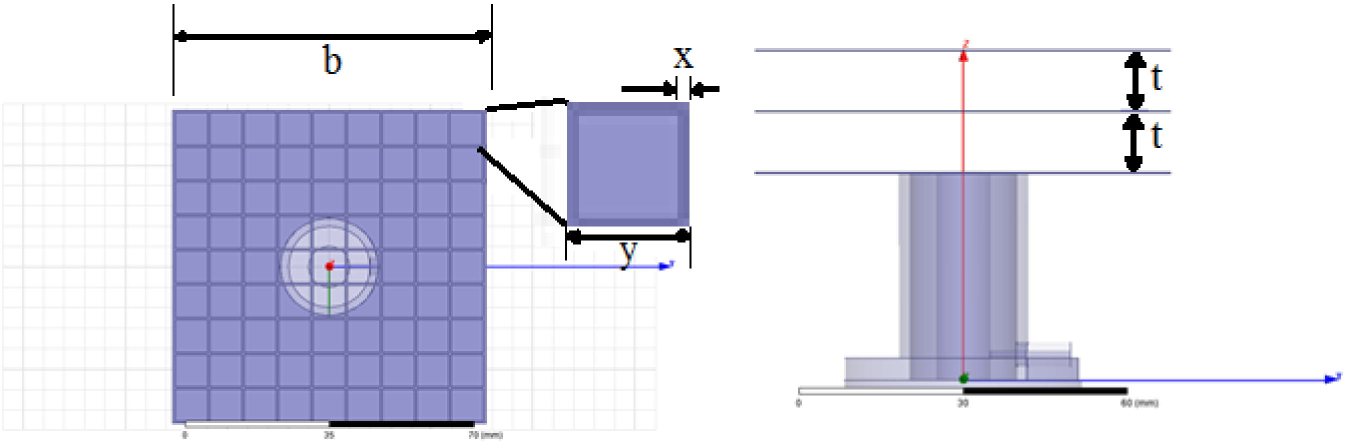

Figure 3.34: Top and side view of ferrite loaded antenna with meta-material structure.

superstrate, the simulated radiation pattern of the antenna demonstrated an increase in directivity to 33 dB and a reduced beam-width is 27.5°, as shown in **Figure 3.36**. But when the ferrite loaed antenna structure with superstrate is simulated for an external magnetizing field of Hdc= 140 KA/m”, it is observed that directivity increase comes at the cost of reduced scan capability of the antenna. In **Figure 3.37**, it is clear that for Hdc= 140 KA/m, the antenna without superstrate demonstrates a directivity of 5.2 dB and a scan angle of 45°. After using the meta-material superstrate, the directivity of the antenna

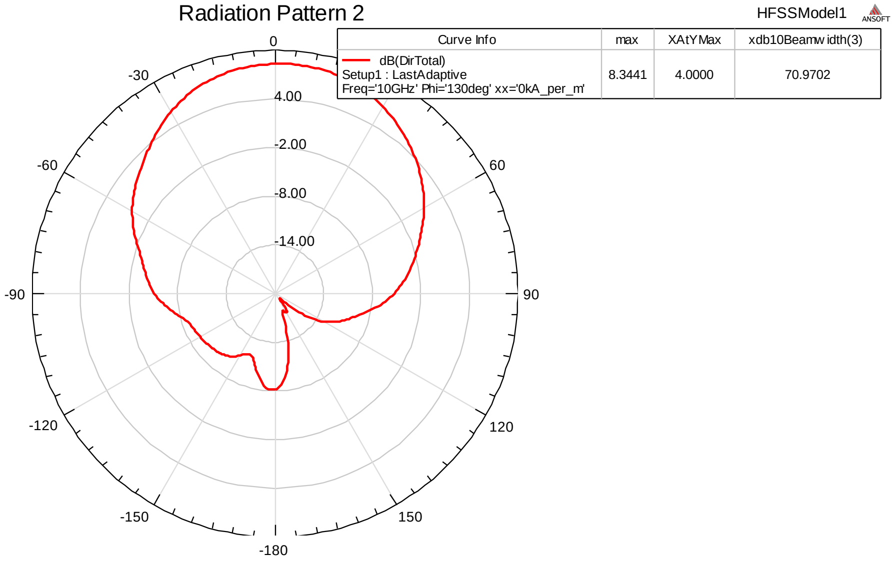

Figure 3.35: Radiation pattern of the antenna without meta-material at Hdc = 0 KA/m.

is observed to increase to 21.4 dB with a reduced scan angle of 5°, as shown in **Figure 3.38**. Thus the directivity increases by using such superstrate are not suitable for the designed antennas due to reducing the novel scanning mechanism.

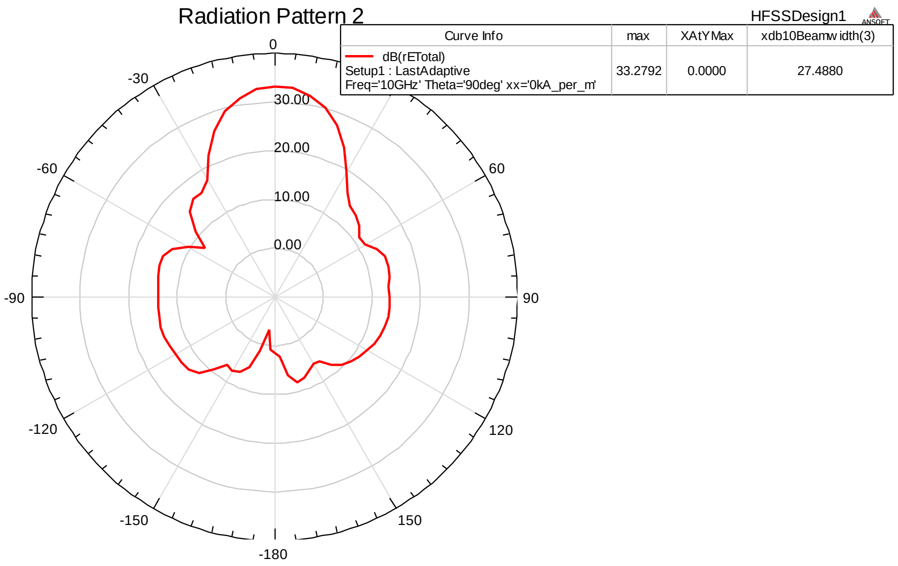

Figure 3.36: Radiation pattern of antenna with superstrate at Hdc = 0 KA/m.

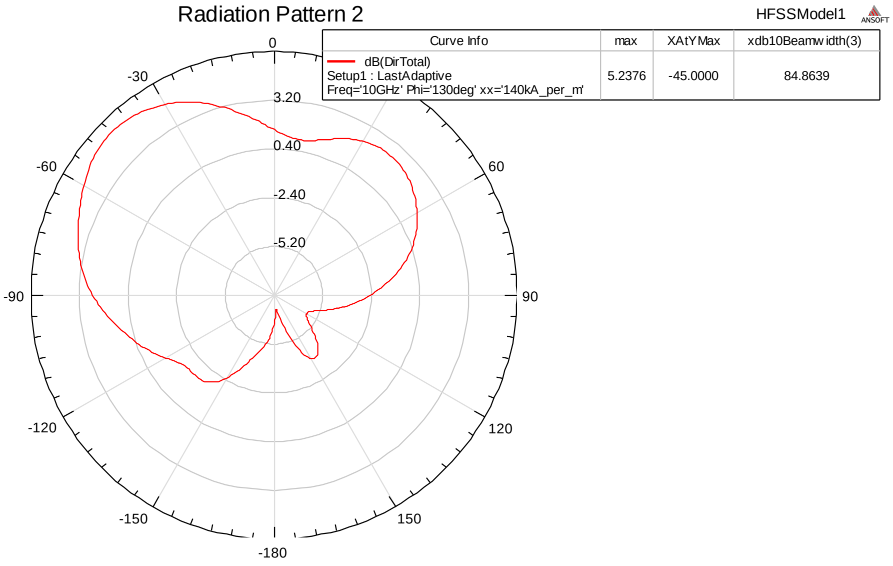

Figure 3.37: Radiation pattern of the antenna without superstrate at Hdc = 140 KA/m.

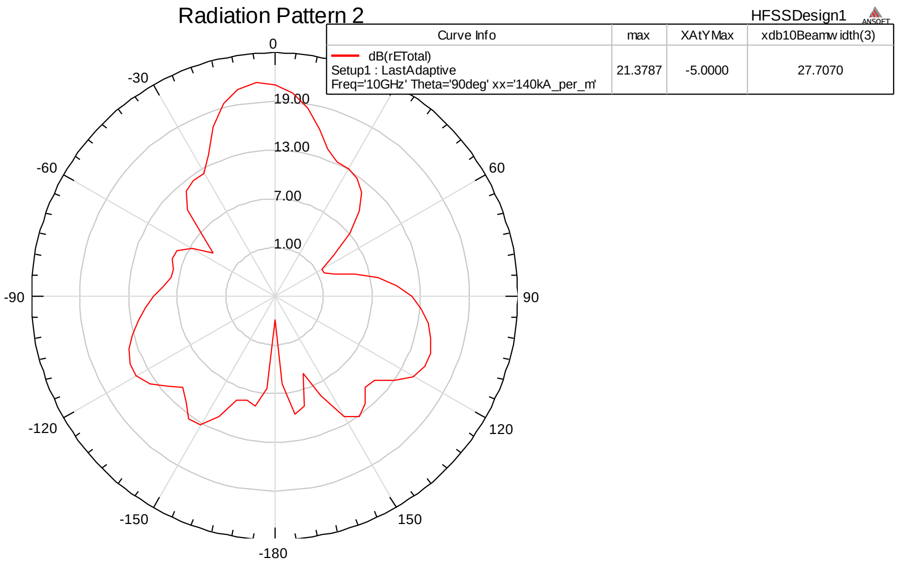

Figure 3.38: Radiation pattern of antenna with superstrate at Hdc = 140 KA/m.

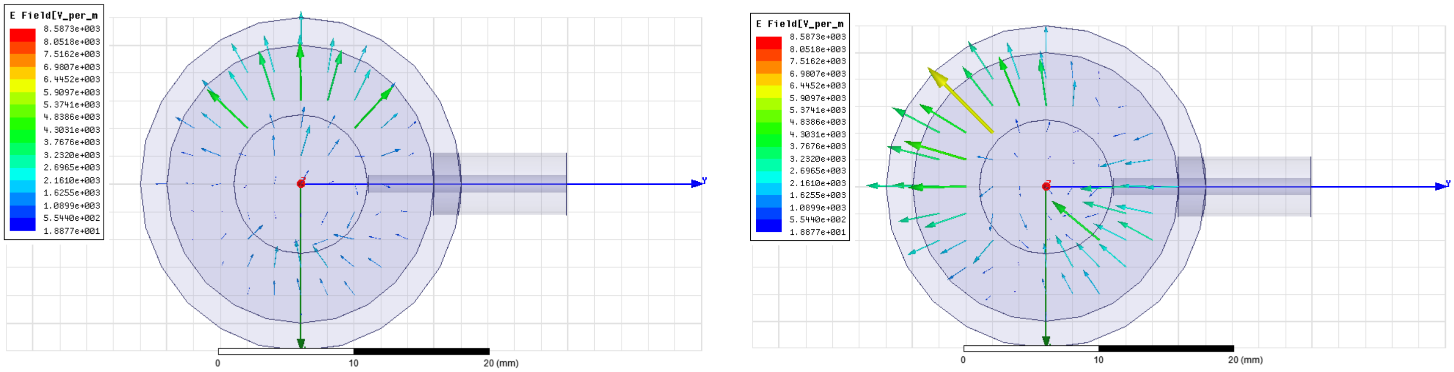

(a) (b)

Figure 3.39: Surface fields distribution for (a) Hdc = 0 KA/m (b)Hdc = 380 KA/m.

Figure 3.39 shows the fields distribution the surface of the antenna where in (a) the external biasing is Hdc = 0 KA/m and in (b) the external biasing is Hdc = 380 KA/m. It is clear from the fields distribution of the different external biasing that the polarization is linear but there will be a shift angle depends on the radiation location.

CHAPTER 4

FABRICATION AND EXPERIMENTAL RESULTS

4.1 Introduction

A brief description of the fabrication process is presented in section 4.2. Section 4.3 represents the antenna measurement setups. In section 4.4, the biasing technique is discussed. Finally, section 4.5 discuss the experimental results of the designed ferrite loaded waveguide antenna to validate the simulated responses of the antenna.

4.2 Fabrication of the Prototype Antenna

The ferrite cylinder was brought from an US company with a specific radius and length “H = 38.8 mm and b = 5 mm” and the ferrite properties **of Ms=800 Guess,ΔH= 10 Oe , εr= 14**.The fabrication process of the waveguide part of the antenna is described here in steps. As a first step, the optimized waveguide antenna was drawn in a paper as per design specification. The drawing had three parts to fabricate separately. The first part is for the waveguide part with two open ends as shown in **Figure 4.1**. Note that the height of the waveguide was ‘H 38.8 mm’ with the inner radius of ‘a = 10 mm’, the outer radius of 12 mm. An aperture or hole was required in one the side of the waveguide to insert the coaxial feeder, needed to excite the waveguide antenna. The location (height from terminated end of the waveguide) was 'h = 4.7 mm' and the radius of hole or aperture was '2.25 mm'. The second part of the design was to fabricate the grounded terminations of one end of the waveguide, which was screwed with the waveguide fabricated in the 1st part. The location of the screws are shown in **Figure 4.2**. Note that the hole in the middle of the waveguide termination was designed to introduced magnetic biasing from the back side of the antenna. The 3rd of the fabrication process was to make the cylindrical conductor, shown in **Figure 4.3,** with radius of 5 mm and designed to provide magnetizing fields to ferrite cylinder.

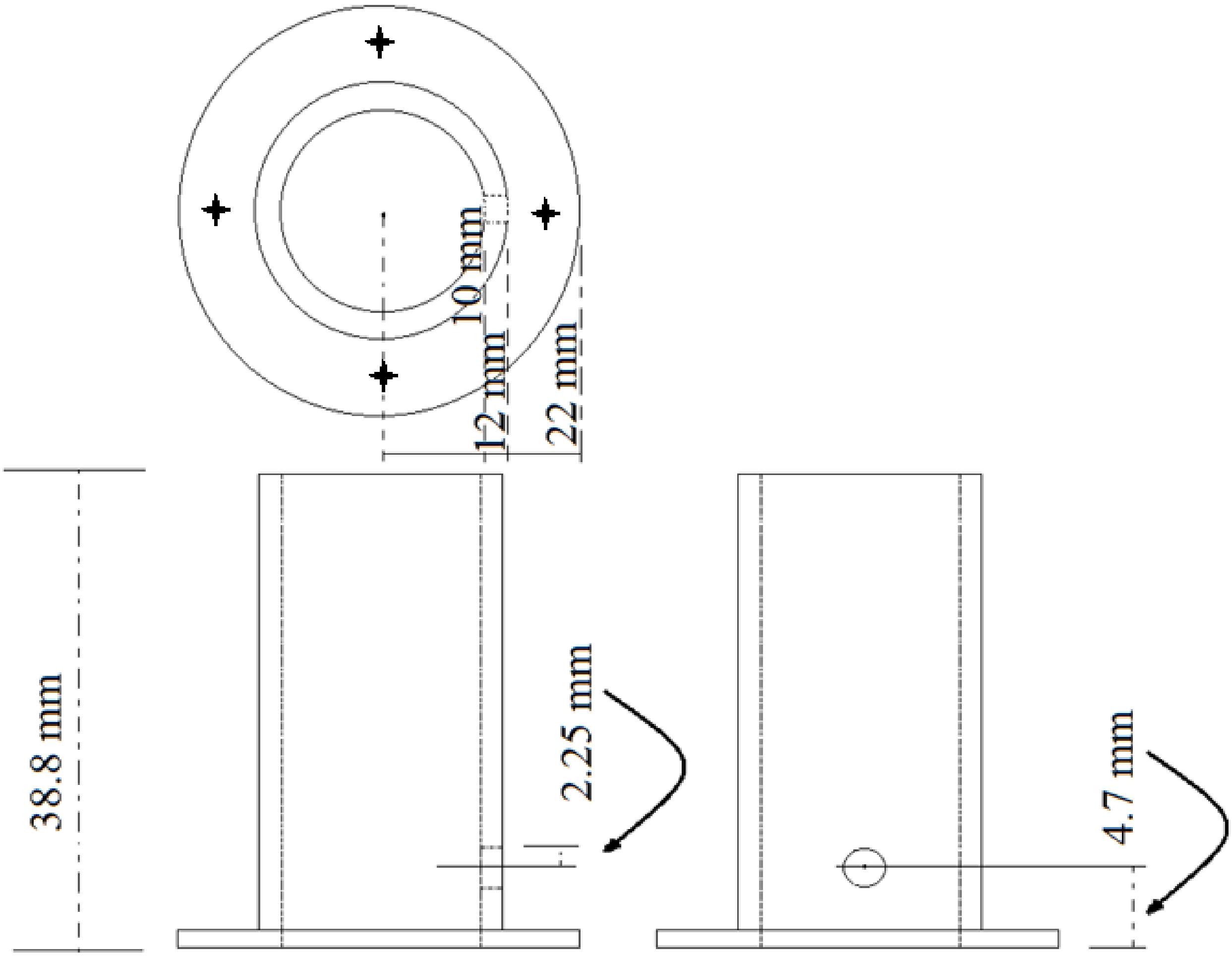

Figure 4.1: Top and sides views of the first part: fabricating the coax feed circular waveguide.

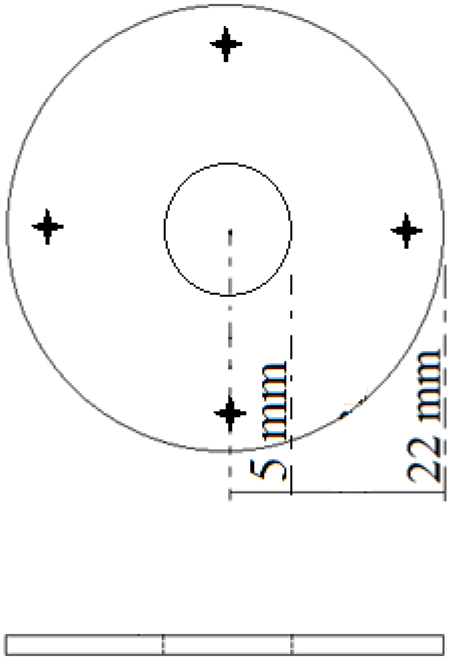

Figure 4.2: Top and sides view of the second part: fabricating the grounded termination of one end of the circular waveguide.

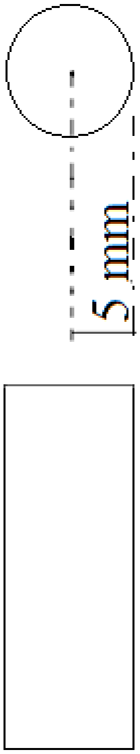

. **Figure 4.3**: Top and sides view of the third part: copper cylinder for providing magnetic biasing field to the ferrite cylinder within the waveguide.

Once the final drawing was complete, the design was given to the lab engineer in the mechanical engineering department (ME) to initiate the fabrication process. Using a filled copper conductor and drill machine, the waveguide with coaxial feed aperture was fabricated with limited accuracy. Then the lab engineer fabricated the terminating copper slab (part 2) and the biasing conductor cylinder (part 3). Upon completion of the fabrication process, the coaxial feeder with a probe length of L = 4.8 mm was integrated with circular waveguide. Then one end of the waveguide was terminated by screwing the terminating copper disk and the ferrite cylinder was inserted in the central part of the waveguide. Using a dielectric material with Er≅1, the ferrite cylinder was positioned in the center of the circular waveguide. The assembled antenna is shown in **Figure 4.4**.

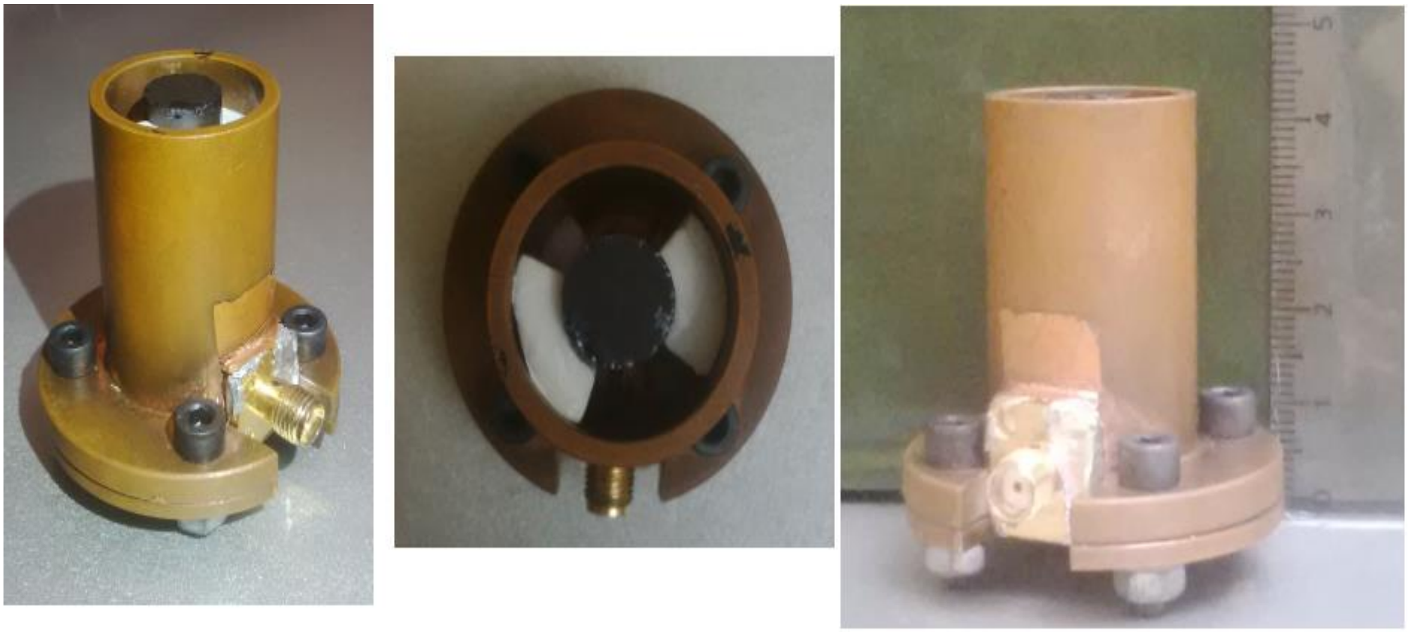

(a) (b) (c)

Figure 4.4: The fabricated antenna (a) 3D view, (b) top view, (c) side view.

4.3 Antenna Measurement Setups

To determine the impedance bandwidth of the designed antenna, S-parameter (S11) measurements were needed. The Vector Network Analyzer is a very common tool to measure the Scattering parameters of active and passive microwave devices. The Vector Network Analyzer, shown in **Figure 4.5**, was used to measures the refection responses (S11) of the antenna in order to determine its impedance bandwidth. But before initiating the measurement, the network analyzer was calibrated to ensure accurate measurements. Calibration is a technique used to compensate the error caused by the

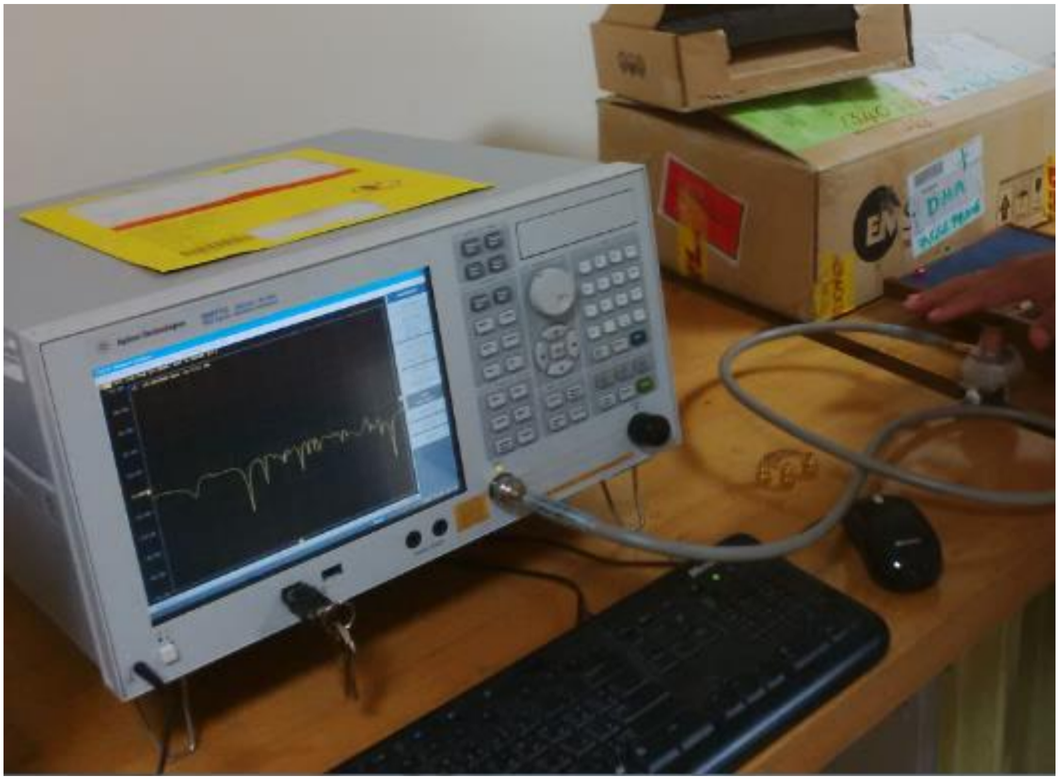

Figure 4.5: Vector Network analyzer used to measure the S_{11} response of the antenna.

characteristic of the cable and connectors. One port calibration is performed by terminating port1 with required loads of short circuit, open circuit and broadband load.

To measure the antenna radiation pattern of the designed antenna, Lab-volt Antenna Measurment System (ATMS) is used, as shown in **Figure 4.5**. It provides the users with a useful tool for hands-on experimentation on antennas in the 1 GHz and 10 GHz bands. ATMS measures the radiation pattern in two planes "E-plane" and "H-plane". It consists of several parts: (a) the acquisition interface, which converts the transmitted and received EM waves to digital signal and supplies to the computer simulator for being plotted; (b) the RF generator that generates the 1 or 10 GHz EM wave and modulates them if needed before transmitting through the transmitter antenna; (c) the antenna positioner, that rotates the receiving antenna to measure the E and H plane of the radiated signals.

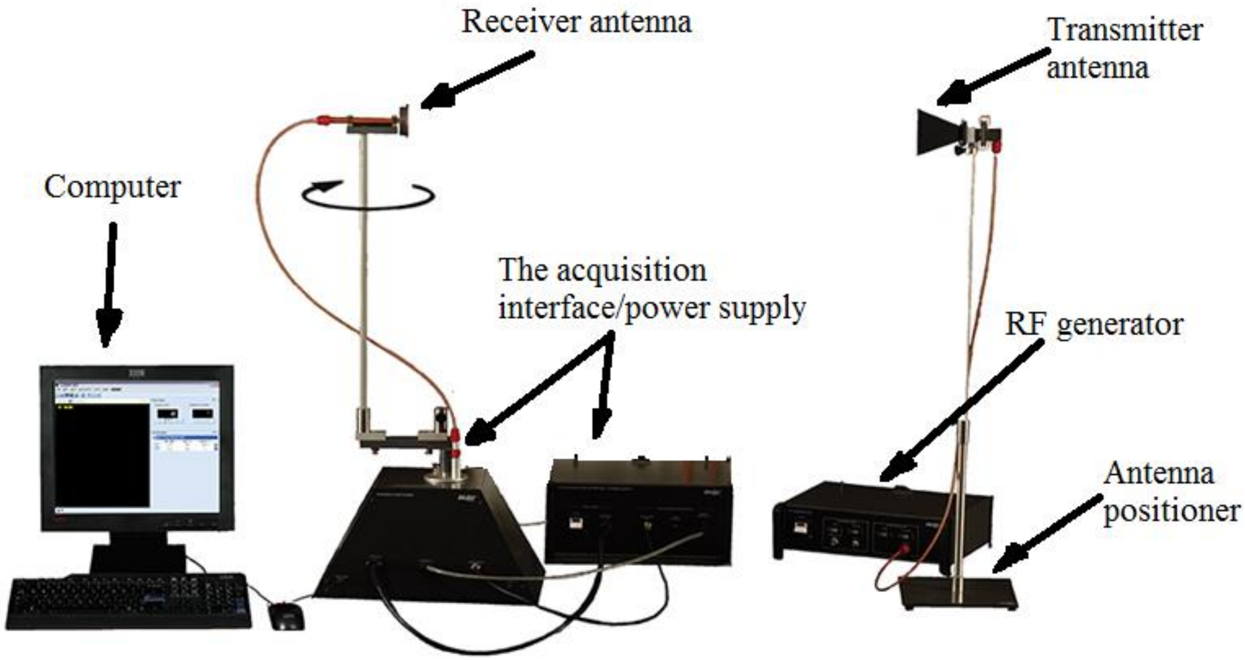

Figure 4.6: The Antenna Training and Measuring System.

4.4 Biasing Technique of the Designed Antenna

Copper wires were used to fabricate pre-calculated biasing coils to introduce externally controllable magnetizing fields to the ferrite cylinders. The wire type was selected to carry a current up to 5-Amp. The equipment required to design the coil as shown in **Figure 4.6** are:

1- Cylindrical plastic with 12 mm inner radius.
2- Cylindrical stick with 5 mm radius.
3- Cutter.
4- Long copper conductors.
5- Sticker tape.

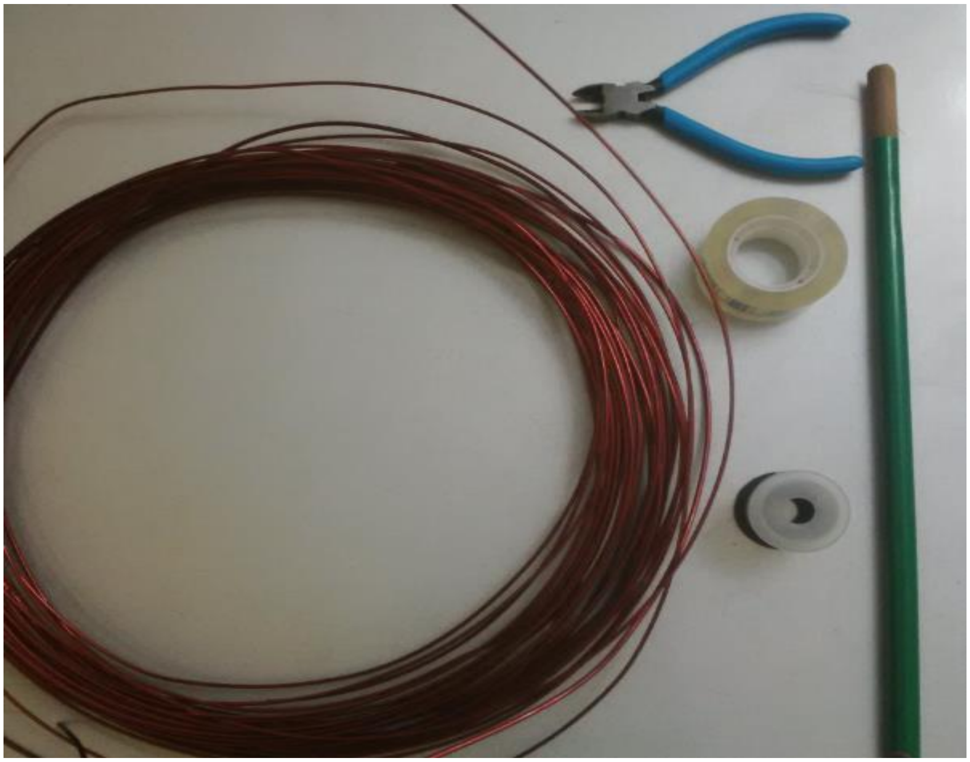

Figure 4.7: The equipment used to fabricate the designed biasing coil for ferrite cylinder.

There were two ways to bias the ferrite. The first way was by putting a coil around the antenna. The second way is by putting the coil from the bottom of the antenna. For the first way, the wire was wound around a cylindrical plastic with R=10mm and after one turn sticker was used to keep the winding in its shape. Then the 2nd and remaining turns of winding are introduced to complete the coil design. Similar steps were followed for the second way, but instead of using plastic core, the copper cylinder was used. **Figure 4.7**shows the first way of the biasing and **Figure 4.8** shows the second way.

Figure 4.8: Biasing the ferrite from the side of the antenna.

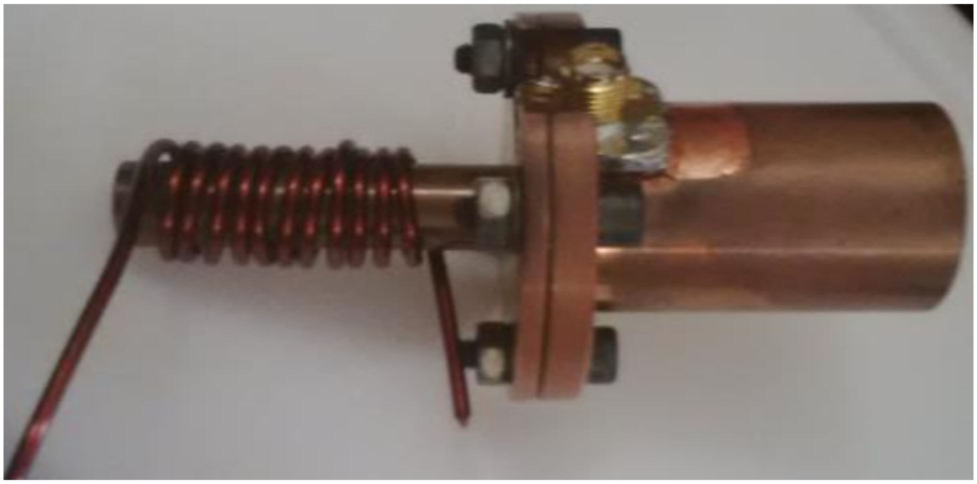

Figure 4.9: Biasing the ferrite from the bottom of the antenna using copper cylinder.

If we are going to compare the two ways in terms of amounts of the magnetic field that can be produced by them, the second way will provide more magnetic field. But when coupled into the ferrite cylinder within the waveguide, the magnetic biasing fields were observed to deteriorate considerably. Thus, the 1st technique was used here, as the maximum magnetic field can be obtained at the center of the coil. So, the coil around the waveguide antenna provided the maximum magnetic biasing field to the centrally located ferrite rod.

4.5 Experimental Results and Analysis

In this section, the experimental process is presented. First step was to measure the magnetizing fields at the center of the biasing coils. This helped to link the magnetizing fields applied to the ferrite cylinder and the supplied currents to the biasing coil. This measurement process is described in section 4.4 and the measured results are shown in **Figure 4.9** and **Figure 4.10**. Note that maximum biasing field measured was 32 mTesla that equivalents to around Hdc=25.5 KA/m.

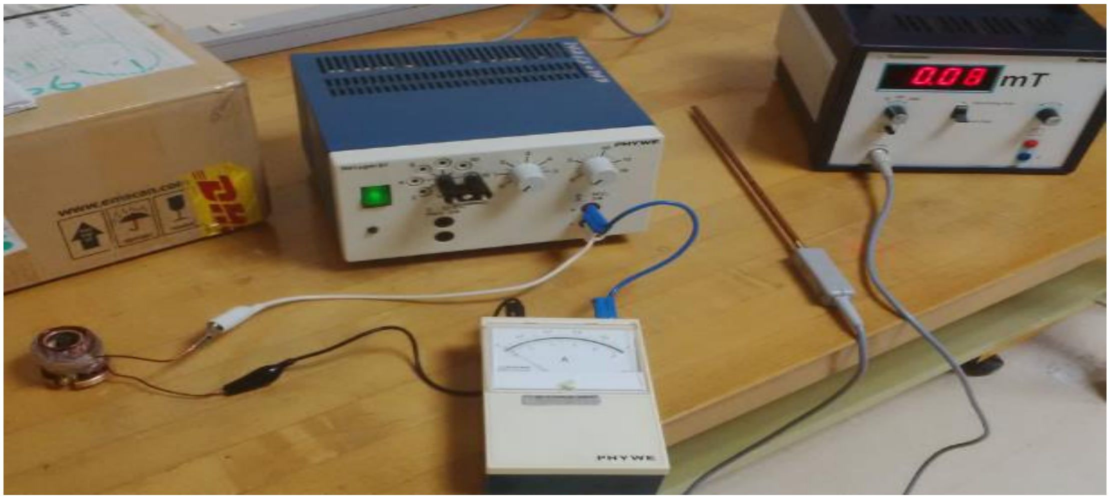

Figure 4.10: Measurement of the magnetizing fields for given currents in the biasing coils.

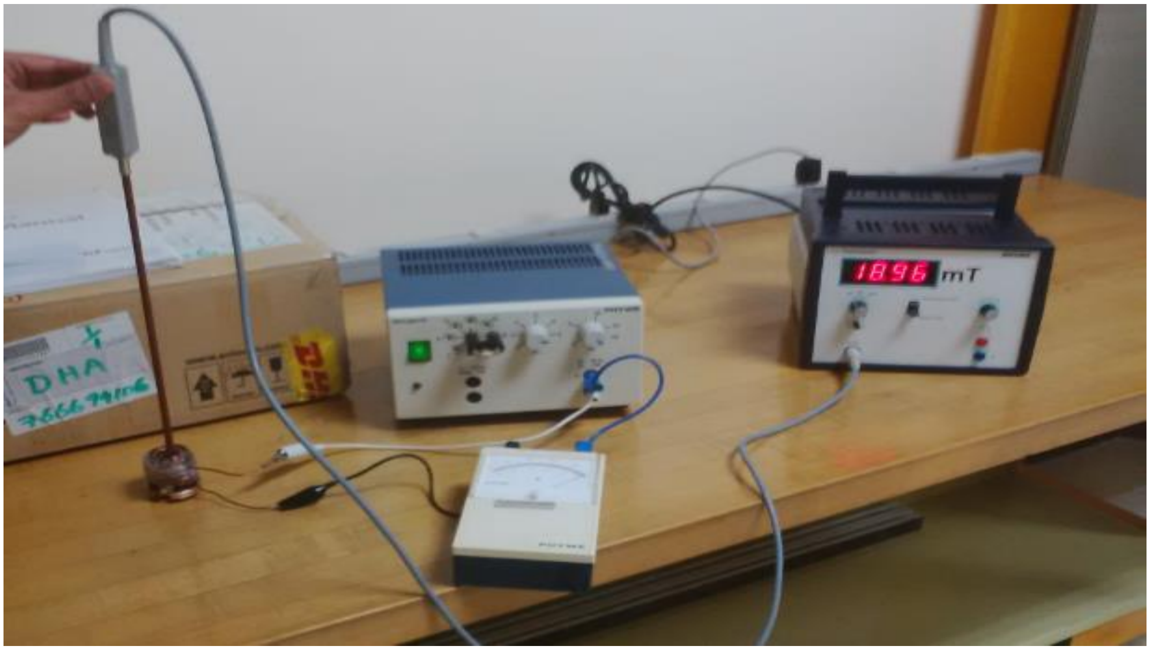

Figure 4.11: Measurement of the external magnetizing fields for given coil currents.

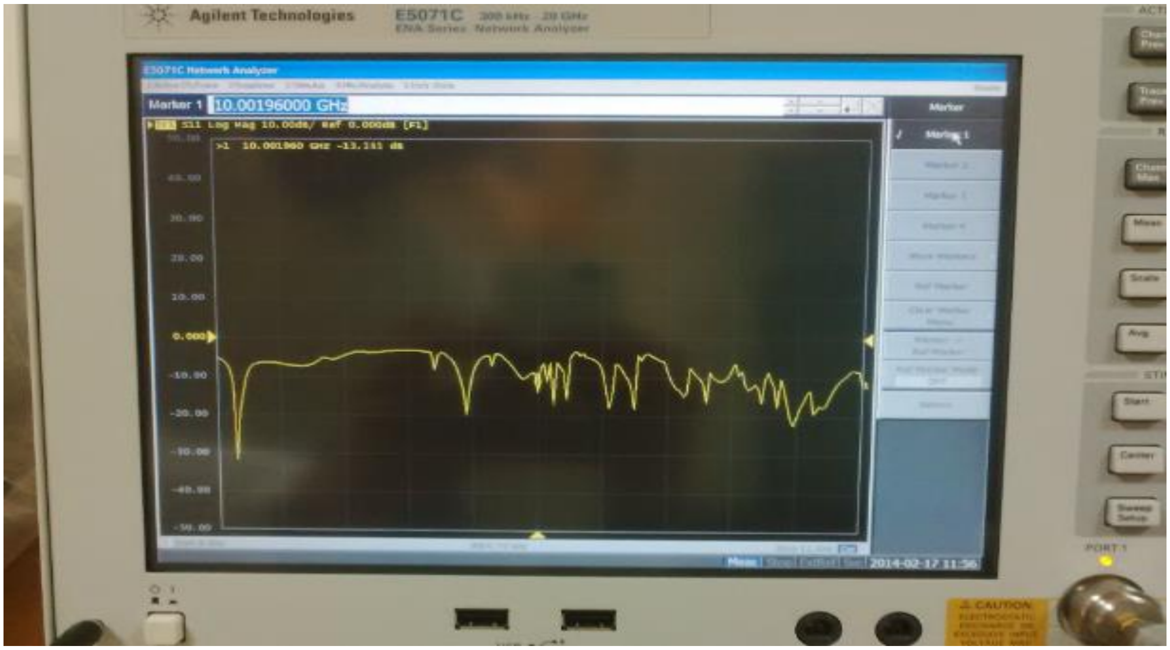

Figure 4.12: The experimental results of the S $_{11}$ measurement as shown in Network Analyzer.

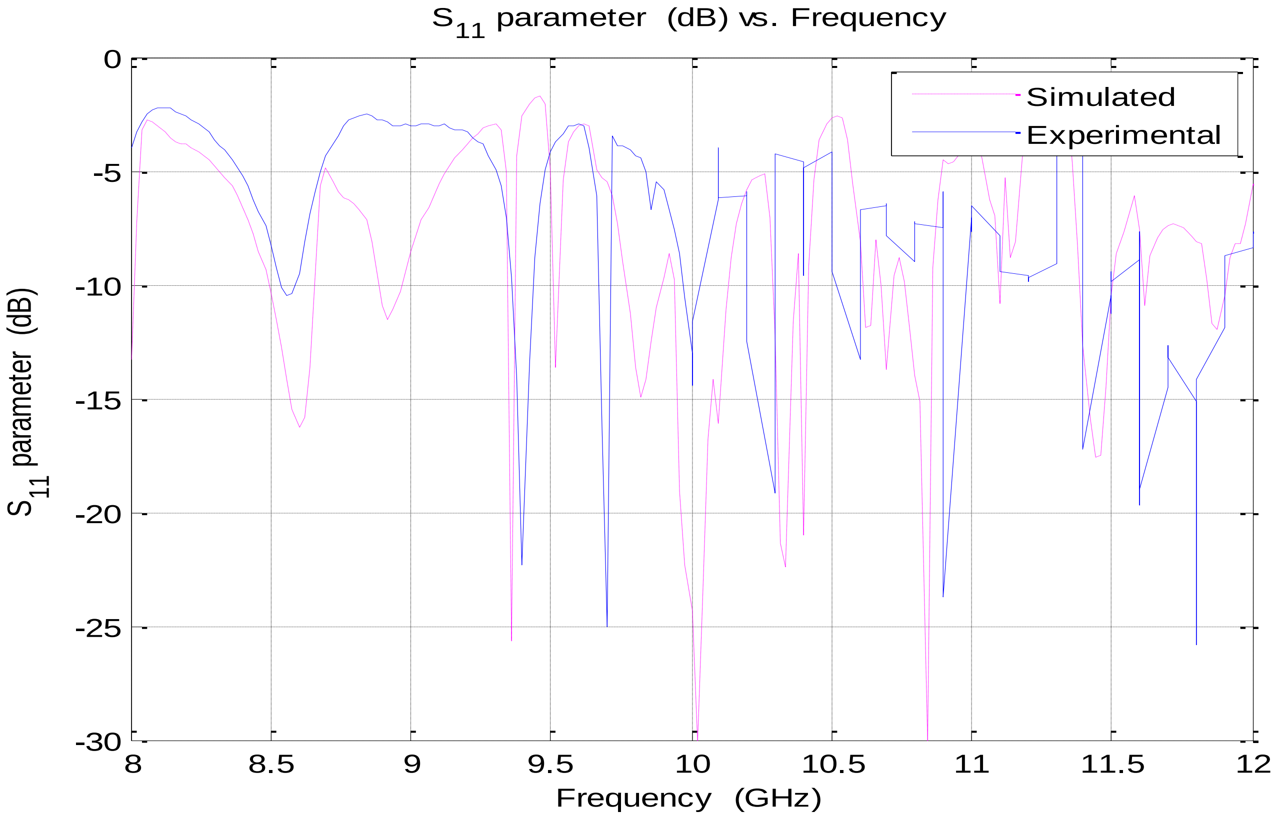

Figure 4.13: The simulated and experimental results of the S $_{11}$ response of the designed antenna

In the first part of the measurement process, the reflection response (S11) of the designed antenna is measured and compared with the simulated responses. The measurement process is discussed in section 4.3. **Figure 4.12** shows the picture of the S11 response, as observed in the network analyzer. **Figure 4.13** superimposes the measured and simulated S11 responses of the designed antenna. Note that at the design frequency of 10 GHz, the simulated S11 responses matches the experimental results. The mismatch between the measured and simulated impedance bandwidth of the antenna are due to the in house fabrication and measurement errors. This point is also clear in earlier chapter, which clearly demonstrates that changing waveguide dimension can alter impedance bandwidth of the antenna.

The last measurement involves monitoring the scan properties of the designed antenna with changing external biasing field. The experimental setup used for this measurement is shown in figures **Figure 4.13** to **4.13**. Detail description of this measurement system was presented in section 4.3. Note that the signal generator, shown in figure **Figure 4.13,** excites the transmitter antenna with the 10 GHz electromagnetic (EM) signal. The

Figure 4.14: The RF generator to excite the transmitter antenna with 10 GHz EM wave.

Figure 4.15: The acquisition interface and power supply.

The data acquisition interface and power supply of the measurement setup is shown in **Figure 4.14**. This acquisition unit interfaces the software with the hardware unit of the measurement setup. The antenna positioner, which rotates the receiving antenna to measure the E and H plane radiation patterns is shown in **Figure 4.15**. The measurement setup with the designed antenna mounted as a receiving antenna is shown in **Figure 4.16**. Note that a standard X-band horn antenna is used as the transmitting antenna in this

Figure 4.16: The antenna is placed in the receiver side.

Figure 4.17: The external magnetic field is applied on the antenna

setup. The biasing coils are also shown in this figure, which is integrated with the antenna to introduce beam scanning properties. To measure the far field patterns, the distance between the receiving antenna and the transmitting horn antenna is selected to be one meter. To measure the E and H-plane radiation patterns, the antenna mounding needed to be changed accordingly. I have created two planes to measure the radiation patterns in the direction between the ‘x’ and ‘y’ axes. **Figure 4.17** show these measurement directions.

Figure 4.18: The measurement axis in between the ‘x and y’ axes.

For the positive biasing or external magnetizing applied in +z-axis, the measured and simulated E-plane radiation patterns are superimposed in **Figure 4.18**. Note that the measured radiation patterns agreed well with the simulated results. In this figure, for an applied biasing field of Hdc= 33 KA/m the main beam points towards 135° in region-4 (of section 3.4).

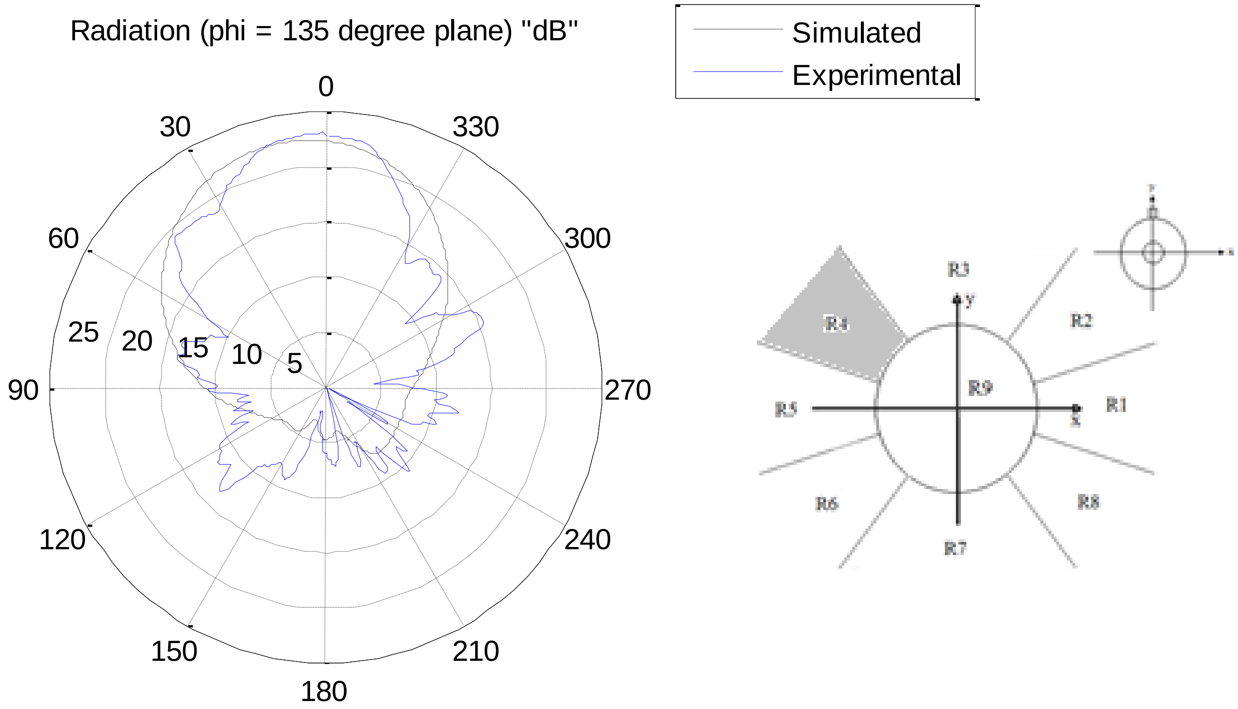

(a) (b)

Figure 4.19: (a) The simulated and experimental radiation patterns for +z-axis biasing of Hdc= 33KA/m. (b) The radiation regions (discussed in section 3.4).

For the negative biasing or external magnetizing applied in -z-axis, the measured and simulated E-plane radiation patterns are superimposed in **Figure 4.19**. Note that the measured radiation patterns also agreed well with the simulated results. This figure demonstrates a beam scan of 45° for an applied biasing field of Hdc= 33 KA/m. Note that this angle belongs to region-2.

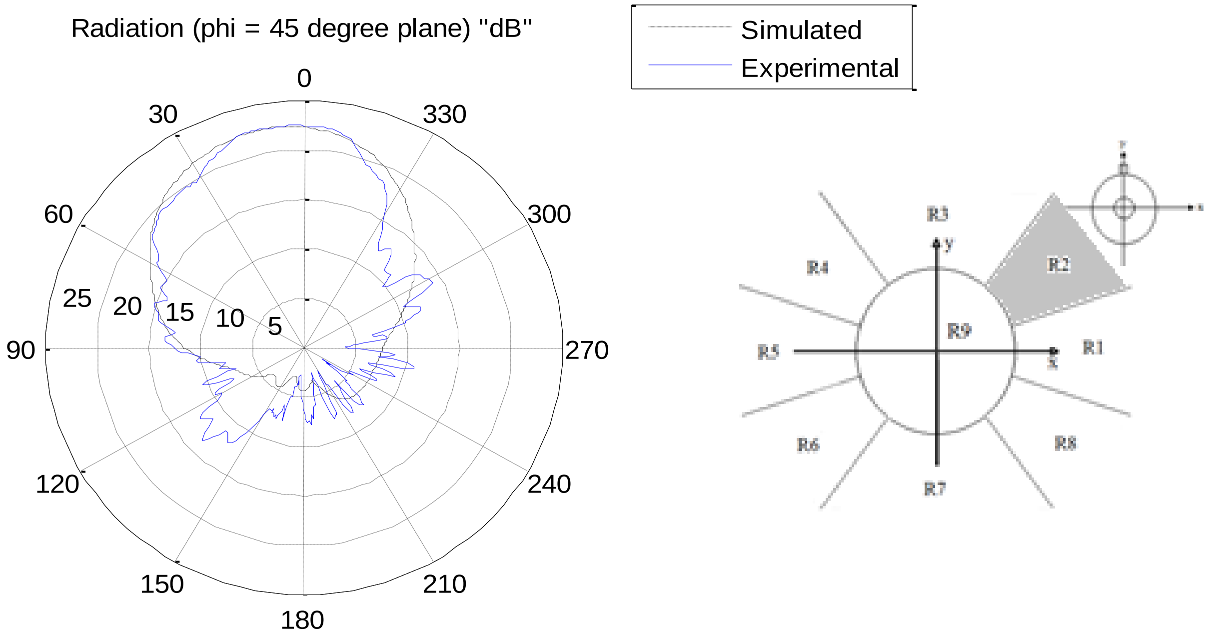

(a) (b)

Figure 4.20: (a) The simulated and experimental radiation pattern of negative biasing (-z-axis). (b) The radiation regions (discussed in section 3.4).

So these figures experimentally demonstrated the beam scanning of the designed ferrite loaded antenna from 135° in region-4 to 45° in region-2. Thus, experimentally verifying some of the simulated responses tabulated in section 3.4. In a similar manner, by designing proper biasing coils, other scan angles tabulated in section 3.4 can be experimentally verified.

CHAPTER 5

CONCLUSION AND FUTURE WORK

5.1 Conclusion

An open ended circular waveguide antenna loaded with concentric ferrite rod is successfully analyzed and proven to provide beam scanning capabilities. In order to achieve this goal an analytical, simulation and experimental works are done. Analytical solutions for the propagation of electromagnetic wave in ferrite cylinder and in a perfectly circular conducting waveguide are developed. The theoretical model obtained is then coded using MATL-LAB to obtain numerical results. In order to check the accuracy of our theoretical results the same results was produced using HFSS. Since the operating frequency suggested for our antenna is 10 GHz, the chart for the ferrite loaded circular conducting waveguide is computed at this frequency. It is found that five modes will propagate in our structure. Mode charts based on theoretical and simulated calculations agreed with each other.

Various antenna parameters, for instance, magnetic field, waveguide radius and height, and feeding probe location have been investigated in this work. There is a resonance region related to the ferrite where range of magnetic field gives bad response. So, this region is removed from the calculation. The reflection coefficient 'S_{11}' is related to the probe location. The radius of the ferrite will effect on the design of the antenna because of the wavelength of the waveguide will be change by changing the radius of the ferrite. The relation between the radius of the ferrite and the modes chart has been found theoretically and by simulated calculation.

The ferrite loaded antenna is designed with the following dimensions, the height of the antenna is 38.8 mm, the radius of the antenna is 10 mm, the radius of the ferrite is 5 mm, operating frequency is 10 GHz, the coaxial feeding is optimized to achieves the S_{11} around -23 dB at the operating frequency with height 4.8 mm and with length inside the antenna 4.7 mm. The antenna characteristics without biasing "$H_{dc} = 0$ A/m" are, the impedance of the bandwidth is 360 MHz, the beam-width for the E-plane and H-plane is around 70^{o}, the gain is around 8.5 dB and the efficiency is 0 dB.

The transverse plane is divided into regions based on the beam-width of the radiation pattern. For each range of external magnetic field, the maximum radiation will be at specific region. There are two ways of biasing the ferrite which are the positive biasing or the negative biasing. There is a relationship between the direction of biasing and the region where they will radiate. Based on the location of the feed which is 'y – axis', the regions that locate along the same axis 'regions 3 and 7' will not be effected by changing the direction of the biasing. While the maximum of the radiations of the regions located in the other axis 'regions 1 and 5' will have 180° beam scan different. For the regions '2 and 4' and regions '6 and 8', there is around 90° beam scan different. By changing the external magnetic field, beam steering can be achieved with around $\theta = \pm 35°$.

The antenna has been fabricated with the specified dimensions. Magnetic coils are designed to bias the ferrite in two directions. The S_{11} and the radiation have be measured experimentally and compared with the HFSS results and they are in good agreement. Various sections of the radiation pattern showed the scanning capabilities were presented.

5.2 Future Recommendation

- Proper biasing coils needed to be designed to experimentally verify the simulated scan angles in all the regions.

- The requirement of large magnetizing field can be reduced by using Low Temperature Co-fired Ceramic LTCC techniques, as discussed in reference [30]. In this work, the biasing fields are reduced by 60% using embedded coil and LTCC fabrication techniques.

- An array of the proposed waveguide antenna can be designed to enhance the antenna directivity.

APPENDIX A

FORMULATION

Ferrite Loaded Circular Waveguide

Consider a circular conducting waveguide of infinite length and radius “*a*” contains a coaxial ferrite rode of radius “*b*” as shown in **Figure A.1**. The space inside the waveguide is denoted as region I inside the ferrite and region II is free space between the ferrite rod and the conducting waveguide.

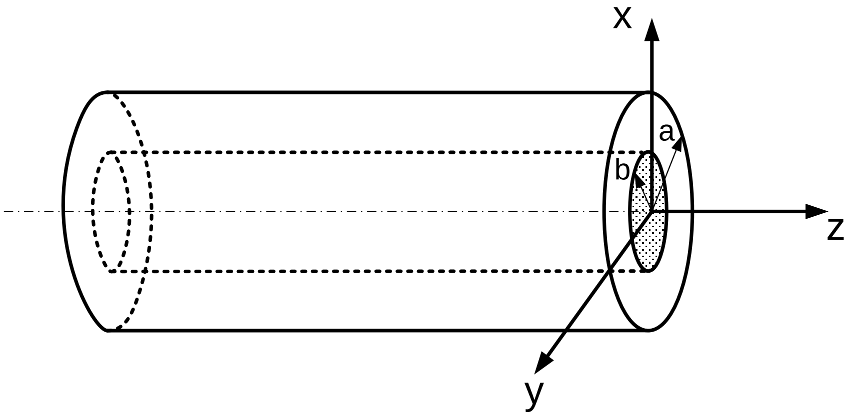

Figure A.1: Geometry of the problem.

The ferrite rode is axially magnetized by a uniform DC magnetic field. We assume that the internal field H_i is equal to the applied field H_a. The ferrite material is characterized at angular frequency ω by their relative permittivity and permeability given by:

$$\varepsilon_f = \varepsilon_f \varepsilon_o \tag{A.1}$$

$$\mu_f = \begin{bmatrix} \mu & -jK & 0 \\ jK & \mu & 0 \\ 0 & 0 & \mu_z \end{bmatrix} \tag{A.2}$$

Where, $$\mu = 1 + \frac{\gamma^2 . H_0 . M}{(\gamma H_0)^2 - f^2} \quad , \mu_z = 1 \tag{A.3}$$

$$K = \frac{\gamma . M . f}{(\gamma H_0)^2 - f^2} \tag{A.4}$$

For demagnetized ferrite

$$\mu_f = \mu_z \text{ and } K = 0 \tag{A.5}$$

The elements μ , K and μ_z of the permeability tensor depend upon the magnetization state of the ferrite.

i- *Coupled wave equations in ferrite materials-Hybrid modes*

Assume the time dependence $e^{j\omega t}$, Maxwell's equations in either region can be written as:

$$\nabla \times \overline{E} = -j\omega \overline{B} \tag{A.6}$$

$$\nabla \times \overline{H} = j\omega\varepsilon \overline{E} \tag{A.7}$$

In which ε in the ferrite is ε_f and μ_f is given by the tensor described in eq. (A.2). *The electric and magnetic fields inside the proposed structure propagates in positive z-direction with propagation constant* $\Gamma = \alpha + j\beta$ *and has z dependence given as:*

$$\overline{E}(x,y,z) = \overline{E}(x,y) e^{-\Gamma z} \tag{A.8}$$

$$\overline{H}(x,y,z) = \overline{H}(x,y) e^{-\Gamma z} \tag{A.9}$$

$$\overline{B}(x,y,z) = \overline{B}(x,y) e^{-\Gamma z} \tag{A.10}$$

Therefore equation (A.6) can be represented as

$$\nabla_T \times \overline{E} - \Gamma \hat{a}_z \times \overline{E} = -j\omega \overline{B} \tag{A.11}$$

$$\nabla_T \times \overline{H} - \Gamma \hat{a}_z \times \overline{H} = j\omega\varepsilon_f \overline{E} \tag{A.12}$$

Where, ∇_T is the Del operator in the *x*-*y* plane and $\hat{a}_z$ is the unit vector in *z*-direction.

From mathematical development one can write:

$$\nabla_T \times \overline{E} = \nabla_T \times \overline{E}_T + \nabla_T E_z \times \hat{a}_z \tag{A.13}$$

$$\nabla_T \times \overline{H} = \nabla_T \times \overline{H}_T + \nabla_T H_z \times \hat{a}_z \tag{A.14}$$

Using equations (A.13) and (A.14) in (A.11) and (A.12), one obtains:

$$\nabla_T \times \overline{E}_T + \hat{a}_z \times (-\Gamma \overline{E}_T - \nabla_T E_z) = -j\omega \overline{B} \tag{A.15}$$

$$\nabla_T \times \overline{H}_T + \hat{a}_z \times (-\Gamma \overline{H}_T - \nabla_T H_z) = j\omega\varepsilon_f \overline{E} \tag{A.16}$$

For the propagation in the ferrite the relation between $\overline{B}$ and $\overline{H}$ is given as:

$$\begin{bmatrix} B_x \\ B_y \\ B_z \end{bmatrix} = \mu \begin{bmatrix} H_x \\ H_y \\ H_z \end{bmatrix} = \begin{bmatrix} \mu & -jK & 0 \\ jK & \mu & 0 \\ 0 & 0 & \mu_z \end{bmatrix} \begin{bmatrix} H_x \\ H_y \\ H_z \end{bmatrix} \tag{A.17}$$

Therefore using (A.17) in (A.15) and equating the longitudinal and transverse components one can get:

$$\nabla_T \times \overline{E}_T = -j\omega\mu_z H_z \hat{a}_z \tag{A.18}$$

$$\nabla_T \times \overline{H}_T = j\omega\varepsilon_f E_z \hat{a}_z \tag{A.19}$$

$$-\hat{a}_z \times \Gamma \overline{E}_T + (j\omega\mu H_x + \omega K H_y)\hat{a}_x + (j\omega\mu H_y - \omega K H_x)\hat{a}_y = \hat{a}_z \times \nabla_T E_z$$

$$-\hat{a}_z \times \Gamma \overline{E}_T + j\omega\mu H_T - \omega K(-H_y \hat{a}_x + H_x \hat{a}_y) = \hat{a}_z \times \nabla_T E_z$$

$$-\hat{a}_z \times \Gamma \overline{E}_T + j\omega\mu H_T - \omega K(\hat{a}_z \times \overline{H}_T) = \hat{a}_z \times \nabla_T E_z \tag{A.20}$$

From (A.16) one can also obtain

$$-\hat{a}_z \times \Gamma \overline{H}_T - j\omega\varepsilon_f \overline{E}_T = \hat{a}_z \times \nabla_T H_z \tag{A.21}$$

From equation (A.21) $\quad -\Gamma(\hat{a}_z \times \overline{H}_T) = j\omega\varepsilon_f \overline{E}_T + \hat{a}_z \times \nabla_T H_z \quad$ substitute in (A.20) after multiplying it by Γ, we get

$$-\hat{a}_z \times \Gamma^2 \overline{E}_T + j\omega\mu\Gamma H_T + j\omega^2\varepsilon_f K\overline{E}_T + \omega K(\hat{a}_z \times \nabla_T H_z) = \Gamma\hat{a}_z \times \nabla_T E_z \tag{A.22}$$

Also (A.21) can be expanded as:

$$-\Gamma H_x = j\omega\varepsilon_f E_y + \frac{\partial H_z}{\partial x} \tag{A.23}$$

$$\Gamma H_y = j\omega\varepsilon_f E_x - \frac{\partial H_z}{\partial y} \tag{A.24}$$

Substitute from (A.23) and (A.24) in (A.22), we get

$$-\hat{a}_z \times \Gamma^2 \overline{E}_T - j\omega\mu((j\omega\varepsilon_f E_y + \frac{\partial H_z}{\partial x})\hat{a}_x - (j\omega\varepsilon_f E_x - \frac{\partial H_z}{\partial y})\hat{a}_y) + j\omega^2\varepsilon_f K\overline{E}_T + \omega K(\hat{a}_z \times \nabla_T H_z) = \Gamma\hat{a}_z \times \nabla_T E_z$$

$$-\hat{a}_z \times \Gamma^2 \overline{E}_T - \omega^2\mu\varepsilon_f(\hat{a}_z \times \overline{E}_T) - j\omega\mu\nabla_T H_z + j\omega^2\varepsilon_f K\overline{E}_T + \omega K(\hat{a}_z \times \nabla_T H_z) = \Gamma\hat{a}_z \times \nabla_T E_z$$

$$-\hat{a}_z \times \Gamma^2 \overline{E}_T - \omega^2\mu\varepsilon_f(\hat{a}_z \times \overline{E}_T) + j\omega^2\varepsilon_f K\overline{E}_T = \Gamma\hat{a}_z \times \nabla_T E_z - \omega K(\hat{a}_z \times \nabla_T H_z) + j\omega\mu\nabla_T H_z$$

$$-(\Gamma^2 + \omega^2\mu\varepsilon_f)(\hat{a}_z \times \overline{E}_T) + j\omega^2\varepsilon_f K\overline{E}_T = \Gamma\hat{a}_z \times \nabla_T E_z - \omega K(\hat{a}_z \times \nabla_T H_z) + j\omega\mu\nabla_T H_z \tag{A.25}$$

Let $\quad \Omega^2 = \Gamma^2 + \omega^2\mu\varepsilon_f\,, \quad k'^2 = \omega^2\varepsilon_f K$

$$-\Omega^2(\hat{a}_z \times \overline{E}_T) + jk'^2\overline{E}_T = \Gamma\hat{a}_z \times \nabla_T E_z - \omega K(\hat{a}_z \times \nabla_T H_z) + j\omega\mu\nabla_T H_z \tag{A.26}$$

Multiply both sides of (A.26) by jk'^2

$$-k'^4\overline{E}_T - jk'^2\Omega^2(\hat{a}_z \times \overline{E}_T) = jk'^2(\Gamma\hat{a}_z \times \nabla_T E_z - \omega K(\hat{a}_z \times \nabla_T H_z) + j\omega\mu\nabla_T H_z) \tag{A.27}$$

Multiplying both sides of (A.26) cross product by $\hat{a}_z$ we obtain:

$$-\Omega^2\hat{a}_z \times (\hat{a}_z \times \overline{E}_T) + jk'^2\hat{a}_z \times \overline{E}_T = \Gamma\hat{a}_z \times (\hat{a}_z \times \nabla_T E_z) - \omega K\hat{a}_z \times (\hat{a}_z \times \nabla_T H_z) + j\omega\mu(\hat{a}_z \times \nabla_T H_z)$$

$$\hat{a}_z \times (\hat{a}_z \times \overline{E}_T) = -\overline{E}_T \quad \hat{a}_z \times (\hat{a}_z \times \nabla_T E_z) = -\nabla_T E_z \quad \hat{a}_z \times (\hat{a}_z \times \nabla_T H_z) = -\nabla_T H_z$$

$$\Omega^2\overline{E}_T + jk'^2\hat{a}_z \times \overline{E}_T = -\Gamma\nabla_T E_z + \omega K\nabla_T H_z + j\omega\mu(\hat{a}_z \times \nabla_T H_z) \tag{A.28}$$

Multiplying both sides Ω^2 one can obtain

$$\Omega^4\overline{E}_T + j\Omega^2 k'^2\hat{a}_z \times \overline{E}_T = \Omega^2(-\Gamma\nabla_T E_z + \omega K\nabla_T H_z + j\omega\mu(\hat{a}_z \times \nabla_T H_z)) \tag{A.29}$$

Adding (A.27) and (A.29):

$$(\Omega^4 - k'^4)\overline{E}_T = \nabla_T(-\Omega^2\Gamma E_z + \Gamma^2\omega K H_z) + j\hat{a}_z \times \nabla_T(\omega(\mu\Omega^2 - k'^2 K)H_z + k'^2\Gamma E_z) \tag{A.30}$$

Equations (A.20) and (A.21) can be manipulated similarly for $\overline{H}_T$ leading to:

$$(\Omega^4 - k'^4)\overline{H}_T = \nabla_T(-\Omega^2\Gamma H_z + k'^2\omega\varepsilon E_z) - j\hat{a}_z \times \nabla_T(\omega\varepsilon\Omega^2 E_z - k'^2\Gamma H_z) \tag{A.31}$$

The other two Maxwell's Divergence equations are:

$$\nabla \cdot \overline{E} = 0 \tag{A.32}$$

$$\nabla \cdot \overline{B} = 0 \tag{A.33}$$

Using (A.8) and (A.10) in (A.32) and (A.33), respectively, one can get:

$$\nabla_T \cdot \overline{E}_T = \Gamma E_z \tag{A.32}$$

$$\nabla_T \cdot \overline{B}_T = \Gamma\mu_z H_z \tag{A.33}$$

Expressing $\overline{B}_T = (\mu H_x + jKH_y)\hat{a}_x + (-jKH_x + \mu H_y)\hat{a}_y = \mu \overline{H}_T + jK\hat{a}_z \times \overline{H}_T$

$$\mu\nabla_T \cdot \overline{H}_T = \Gamma\mu_z H_z - jK\nabla_T \cdot (\hat{a}_z \times \overline{H}_T) \tag{A.34}$$

But $\nabla_T \cdot (\hat{a}_z \times \overline{H}_T) = -\hat{a}_z \cdot (\nabla_T \times \overline{H}_T)$

From (19) $\nabla_T \cdot (\hat{a}_z \times \overline{H}_T) = -\hat{a}_z \cdot (\nabla_T \times \overline{H}_T) = -j\omega\varepsilon_f E_z$

Thus from (34) $\mu\nabla_T \cdot \overline{H}_T = \Gamma\mu_z H_z - K\omega\varepsilon_f E_z$

Or
$$\nabla_T \cdot \overline{H}_T = \Gamma\frac{\mu_z}{\mu} H_z - \omega\varepsilon_f \frac{K}{\mu} E_z \tag{A.35}$$

Taking the divergence of (A.30), leads to

$$(\Omega^4 - k'^4)\nabla_T \cdot \overline{E}_T = \nabla_T \cdot \nabla_T(-\Omega^2\Gamma E_z + \Gamma^2\omega K H_z) + j\nabla_T \cdot (\hat{a}_z \times \nabla_T(\omega(\mu\Omega^2 - k'^2 K)H_z + k'^2\Gamma E_z))$$

$$\Gamma(\Omega^4 - k'^4)E_z = \nabla_T^2(-\Omega^2\Gamma E_z + \Gamma^2\omega K H_z) + j\nabla_T \cdot (\hat{a}_z \times \nabla_T(\omega(\mu\Omega^2 - k'^2 K)H_z + k'^2\Gamma E_z))$$

But $\nabla_T \cdot (\hat{a}_z \times (\nabla_T F)) = -\hat{a}_z \cdot (\nabla_T \times \nabla_T F) = 0$

Thus
$$\Gamma(\Omega^4 - k'^4)E_z = \nabla_T^2(-\Omega^2\Gamma E_z + \Gamma^2\omega K H_z) \tag{A.36}$$

Taking the divergence of (A.31), leads to

$$(\Omega^4 - k'^4)\nabla_T \cdot \overline{H}_T = \nabla_T \cdot \nabla_T(-\Omega^2\Gamma H_z + k'^2\omega\varepsilon_f E_z) - j\nabla_T \cdot (\hat{a}_z \times \nabla_T(\omega\varepsilon_f\Omega^2 E_z - k'^2\Gamma H_z))$$

$$(\Omega^4 - k'^4)\left(\Gamma\frac{\mu_z}{\mu} H_z - \omega\varepsilon_f \frac{K}{\mu} E_z\right) = \nabla_T^2(-\Omega^2\Gamma H_z + k'^2\omega\varepsilon_f E_z) \tag{A.37}$$

Multiplying (A.36) by Ω^2 and (A.37) by $\Gamma\omega K$ and adding

$$-(\Omega^4\Gamma - k'^2\varepsilon_f\omega^2\Gamma K)\nabla_T^2 E_z = -(\omega^2\varepsilon_f \frac{K}{\mu}\Gamma K - \Gamma\Omega^2)(\Omega^4 - k'^4)E_z + (\Omega^4 - k'^4)\omega K\Gamma^2\frac{\mu_z}{\mu} H_z$$

$$-(\Omega^4 - k'^4)\Gamma\nabla_T^2 E_z = -(\frac{K}{\mu}\Gamma k'^2 - \Gamma\Omega^2)(\Omega^4 - k'^4)E_z + (\Omega^4 - k'^4)\omega K\Gamma^2\frac{\mu_z}{\mu} H_z$$

$$\nabla_T^2 E_z = \left(\frac{K}{\mu} k'^2 - \Omega^2\right) E_z - \omega K \Gamma \frac{\mu_z}{\mu} H_z$$

$$\nabla_T^2 E_z + aE_z + bH_z = 0 \tag{A.38}$$

$$a = \Omega^2 - \frac{K}{\mu} k'^2 \quad b = \omega K \Gamma \frac{\mu_z}{\mu} \tag{A.39}$$

Multiplying (A.36) by $k'^2 \omega \varepsilon_f$ and (A.37) by $\Omega^2 \Gamma$ and adding

$$\Gamma k'^2 \omega \varepsilon_f E_z + \Omega^2 \Gamma \left(\Gamma \frac{\mu_z}{\mu} H_z - \omega \varepsilon_f \frac{K}{\mu} E_z \right) = -\Gamma^2 \nabla_T^2 H_z$$

$$\nabla_T^2 H_z + \Omega^2 \frac{\mu_z}{\mu} H_z - \left(\frac{\omega \varepsilon_f K}{\mu} \Gamma \right) E_z = 0$$

$$\nabla_T^2 H_z + cH_z + dE_z = 0 \tag{A.40}$$

$$c = \Omega^2 \frac{\mu_z}{\mu} \quad d = -\frac{\omega \varepsilon_f K}{\mu} \Gamma \tag{A.41}$$

Equations (A.38) and (A.40) are wave equations for wave propagating in the ferrite rode. Solution of these wave equations can be achieved as follows:

For coupled equations (A.38) and (A.40), to obtain a second-order equation, we put

$$E_z = \varphi_1 + \varphi_2 \tag{A.42}$$

$$H_z = r_1 \varphi_1 + r_2 \varphi_2 \text{ with } r_1 \neq r_2 \tag{A.43}$$

The variables φ_1 and φ_2 are two independent variables. Now, substituting from (A.42) and (A.43) into (A.38) and (A.40), we obtain

$$\nabla_T^2 \varphi_1 + (a + br_1)\varphi_1 + \nabla_T^2 \varphi_2 + (a + br_2)\varphi_2 = 0 \tag{A.44}$$

$$r_1 \nabla_T^2 \varphi_1 + (d + cr_1)\varphi_1 + r_2 \nabla_T^2 \varphi_2 + (d + cr_2)\varphi_2 = 0 \tag{A.45}$$

Assume

$$\left.\begin{aligned} a+br_1 &= s_1^2 \\ a+br_2 &= s_2^2 \end{aligned}\right\} \tag{A.46}$$

and $\left.\begin{aligned} d+cr_1 &= r_1 s_1^2 \\ d+cr_2 &= r_2 s_2^2 \end{aligned}\right\}$ (A.47)

Then equations (A.44) and (A.45) can be written as:

$$\nabla_T^2\varphi_1 + s_1^2\varphi_1 + \nabla_T^2\varphi_2 + s_2^2\varphi_2 = 0 \tag{A.48}$$

$$r_1\nabla_T^2\varphi_1 + r_1 s_1^2\varphi_1 + r_2\nabla_T^2\varphi_2 + r_2 s_2^2\varphi_2 = 0 \tag{A.49}$$

Since $r_1 \neq r_2$ therefore φ_1 and φ_2 must satisfy the wave equations

$$\nabla_T^2\varphi_1 + s_1^2\varphi_1 = 0 \tag{A.50}$$

$$\nabla_T^2\varphi_2 + s_2^2\varphi_2 = 0 \tag{A.51}$$

In addition r_1 and r_2 can be obtained from

$$r_{1,2} = \frac{s_{1,2}^2 - a}{b} = \frac{d}{s_{1,2}^2 - c} \tag{A.52}$$

From (A.46) and (A.47), one can get s_1^2 and s_2^2 from the quadratic equation:

$$s^4 - (a+c)s^2 + ca - bd = 0 \tag{A.53}$$

where $ca - bd \neq 0$ in order not to have equal roots.

$$ca - bd = \frac{\mu_z}{\mu}\left(\Omega^4 - \omega^4\varepsilon_f^2 K^2\right) \neq 0$$

That is to say $\Omega^2 \neq \pm\omega^2\varepsilon_f K \Rightarrow \Gamma^2 \neq -\omega^2\varepsilon_f(\mu \pm K)$ (A.54)

The roots of (A.53) can be obtained as:

$$s_{1,2}{}^{2} = \frac{(a+c) \pm \sqrt{(a+c)^2 - 4(ca - bd)}}{2} = \frac{(a+c) \pm \sqrt{(a-c)^2 + 4bd}}{2} \tag{A.55}$$

Equations (A.50) and (A.51) can be developed in cylindrical coordinates as

$$\left(\frac{\partial^2}{\partial \rho^2} + \frac{1}{\rho} \frac{\partial}{\partial \rho} + \frac{1}{\rho^2} \frac{\partial^2}{\partial \theta^2} \right) \varphi_{1,2} + s_{1,2}^2 \varphi_{1,2} = 0$$

Using separation of variables:

$$\varphi_{1,2}(\rho, \theta, z) = \varphi_{1,2}(\rho) \varphi_{1,2}(\theta) \varphi_{1,2}(z)$$

$$\varphi_{1,2}(r) = J_n(s_{1,2}\rho)$$

$$\varphi_{1,2}(\theta) = e^{jm\theta}$$

$$\varphi_{1,2}(z) = e^{-\Gamma z}$$

Where *n* is an integer positive or negative and m are the radial wave number.

$$\varphi_{1,2}(\rho, \theta, z) = A \times J_n(s_{1,2}\rho) e^{jn\theta} e^{-\Gamma z}$$

Therefore the general expression of the complex longitudinal component in ferrite is of the following form:

$$\varphi_f(\rho, \theta, z) = [A_1 * J_n(s_1\rho) + A_2 * J_n(s_2\rho)] e^{jn\theta} e^{-\Gamma z} \tag{A.56}$$

ii- *wave equations in dielectric material*

the wave equation for the dielectric material can be obtained from Maxwell's equations (6) and (7), as:

$$\nabla^2 E_z + k_d^2 E_z = 0$$

$$\nabla^2 H_z + k_d^2 H_z = 0$$

The solution of either wave equation in cylindrical coordinates in can be represented as:

$$\varphi_d(\rho,\theta,z) = [A_3 * J_n(k_d\rho) + A_4 * Y_n(k_d\rho)]e^{jn\theta}e^{-\Gamma z} \qquad \text{(A.57)}$$

where φ_d can represent either E_z or H_z while $k_d^2 = \omega^2\mu_d\varepsilon_d + \Gamma^2$ and J_n , Y_n are Bessel functions of first and second kind.

The electric and magnetic fields in the ferrite and dielectric must be hybrid, accordingly

- For TM to z

$$E_\rho = \frac{1}{j\omega\varepsilon}\frac{\partial^2\psi}{\partial\rho\partial z} \quad H_\rho = \frac{1}{\rho}\frac{\partial\psi}{\partial\phi}$$

$$E_\phi = \frac{1}{j\omega\varepsilon\rho}\frac{\partial^2\psi}{\partial\phi\partial z} \quad H_\phi = -\frac{\partial\psi}{\partial\rho}$$

$$E_z = \frac{1}{j\omega\varepsilon}\left(\frac{\partial^2}{\partial z^2} + k^2\right)\psi \quad H_z = 0$$

- For TE to z

$$E_\rho = \frac{-1}{\rho}\frac{\partial\psi}{\partial\phi} \quad H_\rho = \frac{1}{j\omega\mu}\frac{\partial^2\psi}{\partial\rho\partial z}$$

$$E_\phi = \frac{\partial\psi}{\partial\rho} \quad H_\phi = \frac{1}{j\omega\mu\rho}\frac{\partial^2\psi}{\partial\phi\partial z}$$

$$E_z = 0 \quad H_z = \frac{1}{j\omega\mu}\left(\frac{\partial^2}{\partial z^2} + k^2\right)\psi$$

Waves in our structure are of hybrid mode type, therefore

$$E_\rho = \frac{1}{j\omega\varepsilon}\frac{\partial^2\psi_m}{\partial\rho\partial z} - \frac{1}{\rho}\frac{\partial\psi_e}{\partial\phi} \quad H_\rho = \frac{1}{\rho}\frac{\partial\psi_m}{\partial\phi} + \frac{1}{j\omega\mu}\frac{\partial^2\psi_e}{\partial\rho\partial z}$$

$$E_\phi = \frac{1}{j\omega\varepsilon\rho}\frac{\partial^2\psi_m}{\partial\phi\partial z} + \frac{\partial\psi_e}{\partial\rho} \quad H_\phi = -\frac{\partial\psi_m}{\partial\rho} + \frac{1}{j\omega\mu\rho}\frac{\partial^2\psi_e}{\partial\phi\partial z}$$

$$E_z = \frac{1}{j\omega\varepsilon}\left(\frac{\partial^2}{\partial z^2} + k^2\right)\psi_m \quad H_z = \frac{1}{j\omega\mu}\left(\frac{\partial^2}{\partial z^2} + k^2\right)\psi_e$$

For dielectric region

$$E_z = \frac{k_d^2}{j\omega\varepsilon}\psi_m = \varphi_d \Rightarrow \psi_m = \frac{j\omega\varepsilon}{k_d^2}E_z$$

$$H_z = \frac{k_d^2}{j\omega\mu}\psi_e = \varphi_d \Rightarrow \psi_e = \frac{j\omega\mu}{k_d^2}H_z$$

Accordingly $$E_z = [A_3 J_n(k_d\rho) + A_4 Y_n(k_d\rho)]\,e^{jn\phi}e^{-\Gamma z} \tag{A.58}$$

$$H_z = [A_5 J_n(k_d\rho) + A_6 Y_n(k_d\rho)]\,e^{jn\phi}e^{-\Gamma z} \tag{A.59}$$

$$E_\rho = \frac{1}{k_d^2}\frac{\partial^2 E_z}{\partial\rho\partial z} - \frac{j\omega\mu}{\rho k_d^2}\frac{\partial H_z}{\partial\phi}$$

$$E_\rho = \frac{-\Gamma}{k_d^2}\frac{\partial E_z}{\partial\rho} + \frac{n\omega\mu}{\rho k_d^2}H_z = \frac{-1}{k_d^2}\left(\Gamma\frac{\partial E_z}{\partial\rho} - \frac{n\omega\mu}{\rho}H_z\right) \tag{A.60}$$

$$H_\rho = \frac{1}{\rho}\frac{\partial \psi_m}{\partial \phi} + \frac{1}{j\omega\mu}\frac{\partial^2 \psi_e}{\partial \rho \partial z}$$

$$H_\rho = \frac{1}{\rho}\frac{j\omega\varepsilon}{k_d^2}\frac{\partial E_z}{\partial \phi} + \frac{1}{k_d^2}\frac{\partial^2 H_z}{\partial \rho \partial z}$$

$$H_\rho = \frac{-n\omega\varepsilon}{\rho k_d^2} E_z - \frac{\Gamma}{k_d^2}\frac{\partial H_z}{\partial \rho} = \frac{-1}{k_d^2}\left(\frac{n\omega\varepsilon}{\rho} E_z + \Gamma \frac{\partial H_z}{\partial \rho}\right) \tag{A.61}$$

$$E_\phi = \frac{1}{j\omega\varepsilon\rho}\frac{\partial^2 \psi_m}{\partial \phi \partial z} + \frac{\partial \psi_e}{\partial \rho}$$

$$E_\phi = \frac{-jn\Gamma}{k_d^2 \rho} E_z + \frac{j\omega\mu}{k_d^2}\frac{\partial H_z}{\partial \rho} = \frac{j}{k_d^2}\left(\omega\mu \frac{\partial H_z}{\partial \rho} - \frac{n\Gamma}{\rho} E_z\right) \tag{A.62}$$

$$H_\phi = -\frac{\partial \psi_m}{\partial \rho} + \frac{1}{j\omega\mu\rho}\frac{\partial^2 \psi_e}{\partial \phi \partial z}$$

$$H_\phi = -\frac{j\omega\varepsilon}{k_d^2}\frac{\partial E_z}{\partial \rho} + \frac{1}{k_d^2}\frac{1}{\rho}\frac{\partial^2 H_z}{\partial \phi \partial z} = \frac{-j}{k_d^2}\left(\omega\varepsilon \frac{\partial E_z}{\partial \rho} + \frac{n\Gamma}{\rho} H_z\right) \tag{A.63}$$

iii- *wave equations in ferrite material*

Equation (A.30)

$$(\Omega^4 - k'^4)\overline{E}_T = \nabla_T(-\Omega^2\Gamma E_z + \Gamma^2\omega K H_z) + j\hat{a}_z \times \nabla_T(\omega(\mu\Omega^2 - k'^2 K)H_z + k'^2\Gamma E_z)$$

Equation (A.31):

$$(\Omega^4 - k'^4)\overline{H}_T = \nabla_T(-\Omega^2\Gamma H_z + k'^2\omega\varepsilon E_z) - j\hat{a}_z \times \nabla_T(\omega\varepsilon\Omega^2 E_z - k'^2\Gamma H_z)$$

$$\nabla_T = \frac{\partial}{\partial\rho}\hat{a}_\rho + \frac{1}{\rho}\frac{\partial}{\partial\phi}\hat{a}_\phi$$

$$(\Omega^4 - k'^4)\overline{E}_\rho = \frac{\partial}{\partial\rho}(-\Omega^2\Gamma E_z + \Gamma^2\omega K H_z) - j\frac{1}{\rho}\frac{\partial}{\partial\phi}(\omega(\mu\Omega^2 - k'^2 K)H_z + k'^2\Gamma E_z)$$

$$(\Omega^4 - k'^4)\overline{E}_\rho = -\Omega^2\Gamma\frac{\partial E_z}{\partial\rho} - j\frac{1}{\rho}k'^2\Gamma\frac{\partial E_z}{\partial\phi} + \Gamma^2\omega K\frac{\partial H_z}{\partial\rho} - j\frac{1}{\rho}\omega(\mu\Omega^2 - k'^2 K)\frac{\partial H_z}{\partial\phi}$$

$$(\Omega^4 - k'^4)\overline{E}_\rho = -\Omega^2\Gamma\frac{\partial E_z}{\partial\rho} - j\frac{1}{\rho}k'^2\Gamma\frac{\partial E_z}{\partial\phi} + \Gamma^2\omega K\frac{\partial H_z}{\partial\rho} - j\frac{1}{\rho}\omega(\mu\Omega^2 - k'^2 K)\frac{\partial H_z}{\partial\phi}$$

$$\Omega^2 = \Gamma^2 + \omega^2\mu\varepsilon_f\,, \quad k'^2 = \omega^2\varepsilon_f K$$

$$(\Omega^4 - k'^4)\overline{E}_\rho = \Gamma\left(-\Omega^2\frac{\partial E_z}{\partial\rho} - j\frac{1}{\rho}k'^2\frac{\partial E_z}{\partial\phi}\right) + \Gamma^2\omega K\frac{\partial H_z}{\partial\rho} - j\frac{1}{\rho}\omega(\mu\Omega^2 - k'^2 K)\frac{\partial H_z}{\partial\phi}$$

$$(\Omega^4 - k'^4)\overline{E}_\rho = \Gamma\left(-\Omega^2\frac{\partial E_z}{\partial\rho} + \frac{n}{\rho}k'^2 E_z\right) + \Gamma^2\omega K\frac{\partial H_z}{\partial\rho} + \frac{n}{\rho}\omega(\mu\Omega^2 - k'^2 K)H_z$$

$$\overline{E}_\rho = \frac{1}{(\Omega^4 - k'^4)}\left[\Gamma\left(-\Omega^2\frac{\partial E_z}{\partial\rho} + \frac{n}{\rho}k'^2 E_z\right) + \Gamma^2\omega K\frac{\partial H_z}{\partial\rho} + \frac{n}{\rho}\omega(\mu\Omega^2 - k'^2 K)H_z\right]$$

Remark:

$$\overline{\nabla}_T = \frac{\partial}{\partial \rho}\hat{a}_\rho + \frac{1}{\rho}\frac{\partial}{\partial \phi}\hat{a}_\phi$$

$$\hat{a}_\rho \times \overline{\nabla}_T = -\frac{1}{\rho}\frac{\partial}{\partial \phi}\hat{a}_\rho + \frac{\partial}{\partial \rho}\hat{a}_\phi$$

Based on the remark and equations (A.30) and (A.31):

$$\overline{E}_\rho = \frac{1}{(\Omega^4 - k'^4)}\left[\Gamma\left(-\Omega^2\frac{\partial E_z}{\partial \rho} + \frac{n}{\rho}k'^2 E_z\right) + \Gamma^2 \omega K\frac{\partial H_z}{\partial \rho} + \frac{n}{\rho}\omega(\mu\Omega^2 - k'^2 K)H_z\right]$$

$$\overline{E}_\rho = \frac{1}{(\Omega^4 - k'^4)}\left[\begin{array}{l}\Gamma\left(-\Omega^2\{s_1 J_n'(s_1\rho) + s_2 J_n'(s_2\rho)\} + \frac{n}{\rho}k'^2\{J_n(s_1\rho) + J_n(s_2\rho)\}\right) \\ + \Gamma^2 \omega K\{s_1 r_1 J_n'(s_1\rho) + s_2 r_2 J_n'(s_2\rho)\} + \frac{n}{\rho}\omega(\mu\Omega^2 - k'^2 K)\{r_1 J_n(s_1\rho) + r_2 J_n(s_2\rho)\}\end{array}\right]$$

$$\overline{E}_\rho = \frac{1}{(\Omega^4 - k'^4)}\left[\begin{array}{l}s_1 J_n'(s_1\rho)\{-\Omega^2\Gamma + r_1\Gamma^2\omega K\} + s_2 J_n'(s_2\rho)\{-\Omega^2\Gamma + r_2\Gamma^2\omega K\} \\ + J_n(s_1\rho)\{\frac{\Gamma n k'^2}{\rho} + \frac{r_1 n\omega}{\rho}(\mu\Omega^2 - k'^2 K)\} + J_n(s_2\rho)\{\frac{\Gamma n k'^2}{\rho} + \frac{r_2 n\omega}{\rho}(\mu\Omega^2 - k'^2 K)\}\end{array}\right]$$

$$\begin{aligned}\overline{E}_\rho &= \frac{A_1 s_1 J_n'(s_1\rho)}{(\Omega^4 - k'^4)}(-\Omega^2\Gamma + r_1\Gamma^2\omega K) + \frac{A_1 n J_n(s_1\rho)}{\rho(\Omega^4 - k'^4)}(\Gamma k'^2 + r_1\omega(\mu\Omega^2 - k'^2 K)) \\ &+ \frac{A_2 s_2 J_n'(s_2\rho)}{(\Omega^4 - k'^4)}\{-\Omega^2\Gamma + r_2\Gamma^2\omega K\} + \frac{A_2 n J_n(s_2\rho)}{\rho(\Omega^4 - k'^4)}(\Gamma k'^2 + r_2\omega(\mu\Omega^2 - k'^2 K))\end{aligned} \qquad \text{(A.64)}$$

$$(\Omega^4 - k'^4)\overline{H}_\rho = \frac{\partial}{\partial\rho}(-\Omega^2\Gamma H_z + k'^2\omega\varepsilon E_z) + j\frac{1}{\rho}\frac{\partial}{\partial\phi}(\omega\varepsilon\Omega^2 E_z - k'^2\Gamma H_z)$$

$$(\Omega^4 - k'^4)\overline{H}_\rho = \frac{\partial}{\partial\rho}(-\Omega^2\Gamma H_z + k'^2\omega\varepsilon E_z) - \frac{n}{\rho}(\omega\varepsilon\Omega^2 E_z - k'^2\Gamma H_z)$$

$$\overline{H}_\rho = \frac{1}{(\Omega^4 - k'^4)}\left[\left(-\Omega^2\Gamma\frac{\partial H_z}{\partial\rho} + k'^2\omega\varepsilon\frac{\partial E_z}{\partial\rho} - \frac{n}{\rho}\omega\varepsilon\Omega^2 E_z + \frac{n}{\rho}k'^2\Gamma H_z)\right)\right]$$

$$\overline{H}_\rho = \frac{1}{(\Omega^4 - k'^4)}\left[\left(\begin{matrix} -\Omega^2\Gamma\{s_1 r_1 J'_n(s_1\rho) + s_2 r_2 J'_n(s_2\rho)\} + k'^2\omega\varepsilon\{s_1 J'_n(s_1\rho) + s_2 J'_n(s_2\rho)\} \\ -\dfrac{n}{\rho}\omega\varepsilon\Omega^2\{J_n(s_1\rho) + J_n(s_2\rho)\} + \dfrac{n}{\rho}k'^2\Gamma\{r_1 J_n(s_1\rho) + r_2 J_n(s_2\rho)\}) \end{matrix}\right)\right]$$

$$\begin{aligned}\overline{H}_\rho = {} & \frac{A_1 s_1 J'_n(s_1\rho)}{(\Omega^4 - k'^4)}(-r_1\Omega^2\Gamma + k'^2\omega\varepsilon) + \frac{A_1 n J_n(s_1\rho)}{\rho(\Omega^4 - k'^4)}(-\omega\varepsilon\Omega^2 + r_1 k'^2\Gamma) \\ & + \frac{A_2 s_2 J'_n(s_2\rho)}{(\Omega^4 - k'^4)}(-r_2\Omega^2\Gamma + k'^2\omega\varepsilon) + \frac{A_2 n J_n(s_2\rho)}{\rho(\Omega^4 - k'^4)}(-\omega\varepsilon\Omega^2 + r_2 k'^2\Gamma)\end{aligned} \qquad \text{(A.65)}$$

$$(\Omega^4 - k'^4)\overline{E}_\phi = \frac{1}{\rho}\frac{\partial}{\partial\phi}(-\Omega^2\Gamma E_z + \Gamma^2\omega K H_z) + j\frac{\partial}{\partial\rho}(\omega(\mu\Omega^2 - k'^2 K)H_z + k'^2\Gamma E_z)$$

$$(\Omega^4 - k'^4)\overline{E}_\phi = \frac{jn}{\rho}(-\Omega^2\Gamma E_z + \Gamma^2\omega K H_z) + j\frac{\partial}{\partial\rho}(\omega(\mu\Omega^2 - k'^2 K)H_z + k'^2\Gamma E_z)$$

$$\overline{E}_\phi = \frac{j}{(\Omega^4 - k'^4)}\left[-\frac{n}{\rho}\Omega^2\Gamma E_z + \frac{n}{\rho}\Gamma^2\omega K H_z + \omega(\mu\Omega^2 - k'^2 K)\frac{\partial H_z}{\partial\rho} + k'^2\Gamma\frac{\partial E_z}{\partial\rho}\right]$$

$$\overline{E}_\phi = \frac{j}{(\Omega^4 - k'^4)}\left[\begin{array}{l} -\dfrac{n}{\rho}\Omega^2\Gamma\{J_n(s_1\rho) + J_n(s_2\rho)\} + \dfrac{n}{\rho}\Gamma^2\omega K\{r_1 J_n(s_1\rho) + r_2 J_n(s_2\rho)\} \\ + \omega(\mu\Omega^2 - k'^2 K)\{s_1 r_1 J'_n(s_1\rho) + s_2 r_2 J'_n(s_2\rho)\} + k'^2\Gamma\{s_1 J'_n(s_1\rho) + s_2 J'_n(s_2\rho)\} \end{array}\right]$$

$$\begin{aligned} \overline{E}_\phi &= \frac{jA_1 n J_n(s_1\rho)}{\rho(\Omega^4 - k'^4)}(-\Omega^2\Gamma + r_1\Gamma^2\omega K) + \frac{jA_1 s_1 J'_n(s_1\rho)}{(\Omega^4 - k'^4)}(r_1\omega(\mu\Omega^2 - k'^2 K) + k'^2\Gamma) \\ &+ \frac{jA_2 n J_n(s_2\rho)}{\rho(\Omega^4 - k'^4)}(-\Omega^2\Gamma + r_2\Gamma^2\omega K) + \frac{jA_2 s_2 J'_n(s_2\rho)}{(\Omega^4 - k'^4)}(r_2\omega(\mu\Omega^2 - k'^2 K) + k'^2\Gamma) \end{aligned} \tag{A.66}$$

$$(\Omega^4 - k'^4)\overline{H}_\phi = \frac{1}{\rho}\frac{\partial}{\partial\phi}(-\Omega^2\Gamma H_z + k'^2\omega\varepsilon E_z) - j\frac{\partial}{\partial\rho}(\omega\varepsilon\Omega^2 E_z - k'^2\Gamma H_z)$$

$$(\Omega^4 - k'^4)\overline{H}_\phi = j\frac{n}{\rho}(-\Omega^2\Gamma H_z + k'^2\omega\varepsilon E_z) - j\frac{\partial}{\partial\rho}(\omega\varepsilon\Omega^2 E_z - k'^2\Gamma H_z)$$

$$\overline{H}_\phi = \frac{-j}{(\Omega^4 - k'^4)}\left[\left(\Omega^2\Gamma\frac{n}{\rho}H_z - k'^2\omega\varepsilon\frac{n}{\rho}E_z + \omega\varepsilon\Omega^2\frac{\partial E_z}{\partial\rho} - k'^2\Gamma\frac{\partial H_z}{\partial\rho}\right)\right]$$

$$\overline{H}_\phi = \frac{-j}{(\Omega^4 - k'^4)}\left[\left(\begin{array}{l} +\Omega^2\Gamma\frac{n}{\rho}\{r_1 J_n(s_1\rho) + r_2 J_n(s_2\rho)\} - k'^2\omega\varepsilon\frac{n}{\rho}\{J_n(s_1\rho) + J_n(s_2\rho)\} \\ +\omega\varepsilon\Omega^2\{s_1 J'_n(s_1\rho) + s_2 J'_n(s_2\rho)\} - k'^2\Gamma\{s_1 r_1 J'_n(s_1\rho) + s_2 r_2 J'_n(s_2\rho)\} \end{array}\right)\right]$$

$$\begin{aligned}\overline{H}_\phi = &-\frac{jA_1 s_1 J'_n(s_1\rho)}{(\Omega^4 - k'^4)}(\omega\varepsilon\Omega^2 - r_1 k'^2\Gamma) - \frac{jA_1 n J_n(s_1\rho)}{\rho(\Omega^4 - k'^4)}(\Omega^2\Gamma r_1 - k'^2\omega\varepsilon) \\ &-\frac{jA_2 s_2 J'_n(s_2\rho)}{(\Omega^4 - k'^4)}(\omega\varepsilon\Omega^2 - r_2 k'^2\Gamma) - \frac{jA_2 n J_n(s_2\rho)}{\rho(\Omega^4 - k'^4)}(\Omega^2\Gamma r_2 - k'^2\omega\varepsilon)\end{aligned} \qquad (A.67)$$

- The field components in the dielectric region are:

$$E_z = A_3 J_n(k_d\rho) + A_4 Y_n(k_d\rho)$$

$$H_z = A_5 J_n(k_d\rho) + A_6 Y_n(k_d\rho)$$

$$E_\rho = -A_3 \frac{\Gamma}{k_d} J'_n(k_d\rho) - A_4 \frac{\Gamma}{k_d} Y'_n(k_d\rho) + A_5 \frac{n\omega\mu}{\rho k_d^2} J_n(k_d\rho) + A_6 \frac{n\omega\mu}{\rho k_d^2} Y_n(k_d\rho)$$

$$H_\rho = -A_3 \frac{n\omega\varepsilon}{\rho k_d^2} J_n(k_d\rho) - A_4 \frac{n\omega\varepsilon}{\rho k_d^2} Y'_n(k_d\rho) - A_5 \frac{\Gamma}{k_d} J'_n(k_d\rho) - A_6 \frac{\Gamma}{k_d} Y'_n(k_d\rho)$$

$$E_\phi = -jA_3 \frac{n\Gamma}{\rho k_d^2} J_n(k_d\rho) - jA_4 \frac{n\Gamma}{\rho k_d^2} Y_n(k_d\rho) + jA_5 \frac{\omega\mu}{k_d} J'_n(k_d\rho) + jA_6 \frac{\omega\mu}{k_d} Y'_n(k_d\rho)$$

$$H_\phi = -jA_3 \frac{\omega\varepsilon}{k_d} J'_n(k_d\rho) - jA_4 \frac{\omega\varepsilon}{k_d} Y'_n(k_d\rho) - jA_5 \frac{n\Gamma}{\rho k_d^2} J_n(k_d\rho) - jA_6 \frac{n\Gamma}{\rho k_d^2} Y_n(k_d\rho)$$

- The field components in the ferrite region are:

$$E_z = A_1 J_n(s_1\rho) + A_2 J_n(s_2\rho)$$

$$H_z = A_1 r_1 J_n(s_1\rho) + A_2 r_2 J_n(s_2\rho)$$

$$\begin{aligned}\overline{E}_\rho &= \frac{A_1 s_1 J_n'(s_1\rho)}{(\Omega^4 - k'^4)}(-\Omega^2\Gamma + r_1\Gamma^2\omega K) + \frac{A_1 n J_n(s_1\rho)}{\rho(\Omega^4 - k'^4)}(\Gamma k'^2 + r_1\omega(\mu\Omega^2 - k'^2 K)) \\ &+ \frac{A_2 s_2 J_n'(s_2\rho)}{(\Omega^4 - k'^4)}\{-\Omega^2\Gamma + r_2\Gamma^2\omega K\} + \frac{A_2 n J_n(s_2\rho)}{\rho(\Omega^4 - k'^4)}(\Gamma k'^2 + r_2\omega(\mu\Omega^2 - k'^2 K))\end{aligned}$$

$$\begin{aligned}\overline{H}_\rho &= \frac{A_1 s_1 J_n'(s_1\rho)}{(\Omega^4 - k'^4)}(-r_1\Omega^2\Gamma + k'^2\omega\varepsilon) + \frac{A_1 n J_n(s_1\rho)}{\rho(\Omega^4 - k'^4)}(-\omega\varepsilon\Omega^2 + r_1 k'^2\Gamma) \\ &+ \frac{A_2 s_2 J_n'(s_2\rho)}{(\Omega^4 - k'^4)}(-r_2\Omega^2\Gamma + k'^2\omega\varepsilon) + \frac{A_2 n J_n(s_2\rho)}{\rho(\Omega^4 - k'^4)}(-\omega\varepsilon\Omega^2 + r_2 k'^2\Gamma)\end{aligned}$$

$$\begin{aligned}\overline{E}_\phi &= \frac{jA_1 n J_n(s_1\rho)}{\rho(\Omega^4 - k'^4)}(-\Omega^2\Gamma + r_1\Gamma^2\omega K) + \frac{jA_1 s_1 J_n'(s_1\rho)}{(\Omega^4 - k'^4)}(r_1\omega(\mu\Omega^2 - k'^2 K) + k'^2\Gamma) \\ &+ \frac{jA_2 n J_n(s_2\rho)}{\rho(\Omega^4 - k'^4)}(-\Omega^2\Gamma + r_2\Gamma^2\omega K) + \frac{jA_2 s_2 J_n'(s_2\rho)}{(\Omega^4 - k'^4)}(r_2\omega(\mu\Omega^2 - k'^2 K) + k'^2\Gamma)\end{aligned}$$

$$\begin{aligned}\overline{H}_\phi &= -\frac{jA_1 s_1 J_n'(s_1\rho)}{(\Omega^4 - k'^4)}(\omega\varepsilon\Omega^2 - r_1 k'^2\Gamma) - \frac{jA_1 n J_n(s_1\rho)}{\rho(\Omega^4 - k'^4)}(\Omega^2\Gamma r_1 - k'^2\omega\varepsilon) \\ &- \frac{jA_2 s_2 J_n'(s_2\rho)}{(\Omega^4 - k'^4)}(\omega\varepsilon\Omega^2 - r_2 k'^2\Gamma) - \frac{jA_2 n J_n(s_2\rho)}{\rho(\Omega^4 - k'^4)}(\Omega^2\Gamma r_2 - k'^2\omega\varepsilon)\end{aligned}$$

iii. boundary conditions and characteristic equation

At ρ = a;

$E_{t\_D} = 0 \rightarrow\rightarrow E_{z\_D} = 0 \quad (\mathrm{Ac}.1)$ and $E_{\varphi\_D} = 0 \quad (\mathrm{Ac}.2)$

So, the tangential electric components of the dialectic region is zero at ρ = a

At ρ = b;

$E_{t_D} = E_{t_D} \rightarrow\rightarrow E_{z_D} = E_{z_F} (\mathrm{Ac}.3)$and $E_{\varphi\_D} = E_{\varphi\_F} (\mathrm{Ac}.4)$

$\mathrm{Ht_D} = \mathrm{Ht}_{_F} \rightarrow\rightarrow H_{z_D} = H_{z_F} (\mathrm{Ac}.5)$and $H_{\varphi\_D} = H_{\varphi\_F} (\mathrm{Ac}.6)$

So, the tangential electric components of the dialectic region equals to the tangential electric components of the ferrite region at ρ = b

$$A_3 J_n(k_d a) + A_4 Y_n(k_d a) = 0$$

$$A_5 J_n'(k_d a) + A_6 Y_n'(k_d a) = 0$$

$$A_1 J_n(s_1 b) + A_2 J_n(s_2 b) - A_3 J_n(k_d b) - A_4 Y_n(k_d b) = 0$$

$$A_1 r_1 J_n(s_1 b) + A_2 r_2 J_n(s_2 b) - A_5 J_n(k_d b) - A_6 Y_n(k_d b) = 0$$

$$\begin{aligned}
&\frac{A_1 n J_n(s_1 b)}{b(\Omega^4 - k'^4)}(-\Omega^2\Gamma + r_1\Gamma^2\omega K) + \frac{A_1 s_1 J_n'(s_1 b)}{(\Omega^4 - k'^4)}(r_1\omega(\mu\Omega^2 - k'^2 K) + k'^2\Gamma) \\
&+ \frac{A_2 n J_n(s_2 b)}{b(\Omega^4 - k'^4)}(-\Omega^2\Gamma + r_2\Gamma^2\omega K) + \frac{A_2 s_2 J_n'(s_2 b)}{(\Omega^4 - k'^4)}(r_2\omega(\mu\Omega^2 - k'^2 K) + k'^2\Gamma) \\
&+ A_3 \frac{n\Gamma}{b k_d^2} J_n(k_d b) + A_4 \frac{n\Gamma}{b k_d^2} Y_n(k_d b) - A_5 \frac{\omega\mu}{k_d} J_n'(k_d b) - A_6 \frac{\omega\mu}{k_d} Y_n'(k_d b) = 0
\end{aligned}$$

$$\begin{aligned}
&\frac{A_1 s_1 J_n'(s_1 b)}{(\Omega^4 - k'^4)}(\omega\varepsilon\Omega^2 - r_1 k'^2\Gamma) + \frac{A_1 n J_n(s_1 b)}{b(\Omega^4 - k'^4)}(\Omega^2\Gamma r_1 - k'^2\omega\varepsilon) \\
&+ \frac{A_2 s_2 J_n'(s_2 b)}{(\Omega^4 - k'^4)}(\omega\varepsilon\Omega^2 - r_2 k'^2\Gamma) + \frac{A_2 n J_n(s_2 b)}{b(\Omega^4 - k'^4)}(\Omega^2\Gamma r_2 - k'^2\omega\varepsilon) \\
&- A_3 \frac{\omega\varepsilon}{k_d} J_n'(k_d b) - A_4 \frac{\omega\varepsilon}{k_d} Y_n'(k_d b) - A_5 \frac{n\Gamma}{b k_d^2} J_n(k_d b) - A_6 \frac{n\Gamma}{b k_d^2} Y_n(k_d b) = 0
\end{aligned}$$

APPENDIX B

HFSS

High Frequency Simulation Software (HFSS v13.0) has been used for the designing and simulating the antenna model. It is a software package for electromagnetic modeling and analysis of passive, three dimensional structures. The finite element method (FEM) is employed in HFSS to calculate the full three-dimensional field inside a structure and the corresponding S-parameters [28]. FEM is a powerful tool for solving complex engineering problems, the mathematical formulation of which is not only challenging but also uninteresting. The structure is divided into smaller sections of finite dimensions connected to each other via nodes where each small section is solved independently of the others to reduce the solution complexity. The final solution is then computed by reconnecting all the sections and combining their solutions [29].

HFSS divides the geometric model into a large number of tetrahedral elements where each element is composed of four equilateral triangles and the collection of tetrahedron forms what is known as the finite element mesh. Each vertex of the tetrahedron is the place where the field components tangentially to the three edges meeting at the vertex are stored as a component which is a vector field at the midpoint of the selected edges. The H-field and the E-field can be estimated by using these stored values. The interpolation is performed by the first-order tangential element basis function. Maxwell's equations are then formulated from the field quantities and transformed into matrix equations that can be solved using the traditional numerical techniques [29].

The first step is to draw the geometric model of the structure that is to be realized. The materials selection is the next step for various drawn objects are mode of. The next step is to define an accurate definition of boundaries for the structure, such as perfect electric, radiation etc. A port or a voltage source has to be defined to excite the structure where this is part of the excitation definition. After complete the model of the structure, the solution is set up where the definition of various parameters such as the frequency at which the adaptive mesh refinement takes place and the convergence criterion. Finally, the solution data is post that may include display of far-field plots, plots and tables of S-parameters etc. **Figure B.1**is summarized flow-chart depiction of the above mentioned theory.

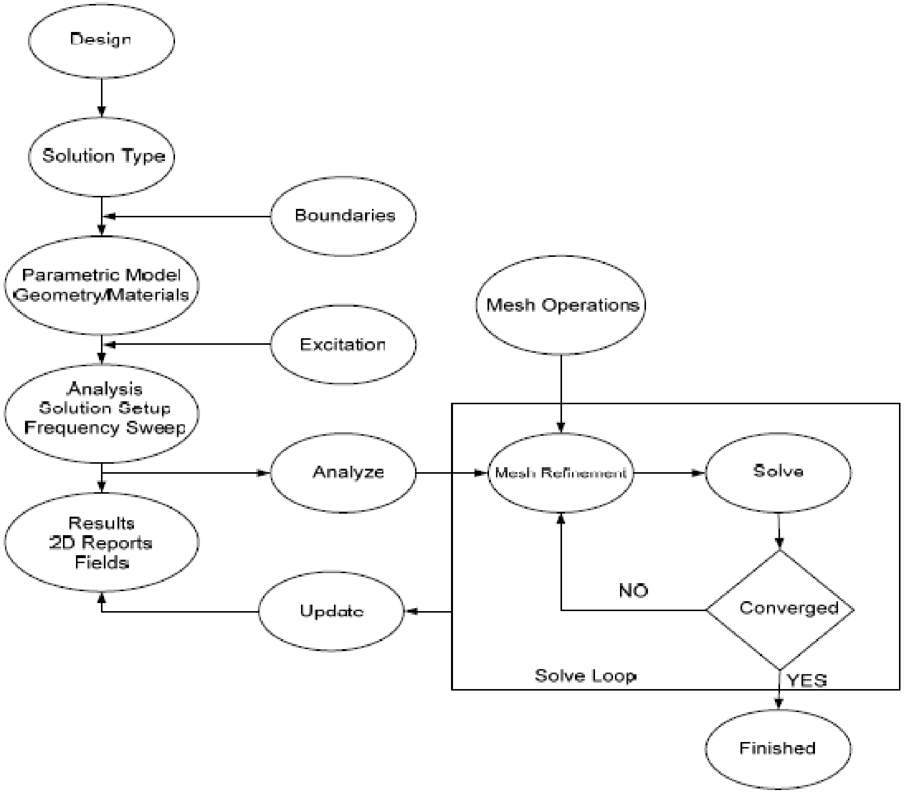

Figure B.1: Process overview flow chart of the HFSS simulation module.

REFERENCES

[1] Pour, Z.A.; Shafai, L.”A novel dual mode circular waveguide horn antenna” 14th International Symposium on Antenna Technology and Applied Electromagnetics Conference (ANTEM), pp.1-4, 2010

[2] Sun-Jie Tzun; Tzu-Liang Lin; Yun Wan; Ming-Chieh Lin; , “Output Analysis of a Circular Horn Antenna: Higher Order Modes”, IEEE International Vacuum Electronics Conference, pp. 369 – 370, August 2006.

[3] Olver A.D., Clarricoats P.J.B., A.A. Kishk and L. Shafai, Microwave horns and feeds. IEE Electromagnetic Waves Series 39, 1994.

[4] Teniente, J., Gonzalo, R., and del Rio, C., “Low Sidelobe Corrugated Horn Antennas for Radio Telescopes to Maximize G/Ts”, IEEE Transactions on Antennas and Propagation, Vol. 59, No. 6, pp. 1886 – 1893, June 2011.

[5] Teniente J., R. Gonzalo and C. del Ro "Modern corrugated horn antenna design for extremely low sidelobe level", 26th ESA Antenna Technology Workshop on Satellite Antenna Modelling and Design Tools, 2003.

[6] Gue-Hua Z., Yun-Qi F., Chang Z., Dun-Bao N., and Nai-Chang Y., “A Circular Waveguide Antenna Using High-Impedance Ground Plane”, IEEE Antenna and Wireless Propagation Letters, Vol. 2, pp 86-88 2003

[7] Henderson A., J. R. James, A. Fray and G. D. Evans, "New Ideas For Beam Scanning Using Magnetised Ferrite", Electronically Scanned Antennas, IEE Colloquium on, 21, Jan. 1988, pp1-4

[8] H. Shimasaki, T. Itoh, "Experimental study on the radiation beam scan of a waveguide slot array antenna filled with a ferrite", Microwave Conference, 2006. APMC 2006. Asia-Pacific, 12-15, Dec. 2006, pp2118-2121.

[9] Robert S. Elliott “Mechanical And Electrical Tolerances For Two-Dimensional Scanning Antenna Arrays”, Ire Trans. Of Antenna And Propagation, Pp. 114-120, January 1958.

[10] Sheikh S. I. M. and Mir Riyaz Ali, “Beam Squint using Integrated Gyrotropic Phase Shifter", Applied Computational Electromagnetic Society (ACES) Journal, ISSN: 1054-4887, Vol. 23, No.2, June, 2008

[11] Allahgholi Pour Z. and Shafai L., “Novel Dual Mode Circular Waveguide Horn Antenna”, 2010 14th International Symposium on Antenna Technology and Applied Electromagnetics [ANTEM], 2010

[12] Li Bin, Wu Bian, Liang Chang-hong, “High Gain Circular Waveguide Array Antenna Using Electromagnetic Band-gap Structure”, Asia-Pacific microwave Conference Proceedings (APMC), December 2005.

[13] Ragheb H. A., “ Radiation from Annular Waveguide”, International URSI/IEEE- AP-S Meeting, Montreal, Canada, July 13-18, 1997

[14] Sheikh S.I., Gibson A.P. and Dillon B.M., "Bias-field/frequency Design Charts for Composite Gyrotropic Resonators", IEEE MTT Symposium, USA, pp 1663-1666, June 16-21, 1996.

[15] BorjakA. M. and Davis L. E., “On Planar Y -Ring Circulators Ieee Transactions On Microwave Theory And Techniques, Vol 42. No. 2, February 1994

[16]A. Henderson, J. R. James, A. Fray and G. D. Evans, "New Ideas For Beam Scanning Using Magnetised Ferrite", Electronically Scanned Antennas, IEE Colloquium on, 21, Jan. 1988, pp1-4.

[17]H. Shimasaki, T. Itoh, "Experimental study on the radiation beam scan of a waveguide slot array antenna filled with a ferrite", Microwave Conference, 2006. APMC 2006. Asia- Pacific, 12-15, Dec. 2006, pp2118-2121.

[18]Sheikh S. I. M. and Mir Riyaz Ali, “Beam Squint using Integrated Gyrotropic Phase Shifter", Applied Computational Electromagnetic Society (ACES) Journal, ISSN: 1054-4887, Vol. 23, No.2, June, 2008.

[19]David M.P. Microwave Engineering, John Wiley & Sons Inc. 2012, pages 215-221.

[20]M. R. Ali, "Design of microstrip linear phased array antenna using integrated array feeder," King Fahd University of Petroleum and Minerals, 2005.

[21] J. C. Batchelor, "Scanned microstrip arrays using simple integrated ferrite phase shifters," IEEE Microwave Antennas and Propagation, vol. 147, no. 3, pp. 237-241, 2000.

[22]Balanis C. A. “Antenna Theory analysis and Design”, John Wiley & Sons Inc., pp 28-64.

[23]Balanis C. A. “Advanced Engineering Electromagnetics”, John Wiley & Sons Inc., pp 470-481.

[24]]Helszajn J. “Ferrite Phase Shifters and Control Devices”, McGRAW-HILL Book Company pp 130-138, 169-194.

[25]Sergei P.S and Per-Simon K., “Performance of an Array of Circular Waveguides with Strip-Loaded Dielectric Hard Walls", IEEE TAP, vol. 48, No.7 pp 1106-1114, July 2000.

[26]Li Bin, Wu Bian, and Liang Chang-hong, “A Study on High Gain Circular Waveguide Array Antenna Using Metamaterial Structure", IEEE 2006.

[27] Hamid M., TowaijS. and Martens G., " A dielectric-loaded circular waveguide antenna", Antennas and Propagation, IEEE Transactions on, Vol. 20, No. 1, pp 96-97 Jan. 1972.

[28] Ansoft HFSS version 9: Overview, 2003.

[29] Felippa, C. A., “Introduction to finite element method”. _http:// caswww.colorado.edu.sa/courses.d/IFEM.d/Ch01.d/ IFEM.Ch01.pdf.

[30] Shamim, A., “Ferrite LTCC-Based Antenna for Tunable SoP Applications”, IEEE Transactions on component, packaging and manufacturing technology, Vol.1, No.7, PP.999- 1006, July 2011.

Vitae

- Abdullah Mohammed AlGarni

- Nationality: Saudi

- Address: P. O. Box 1772, K.F.U.P.M., Dhahran 31261, Saudi Arabia

- Telephone: (+966) 503962770

- Email: algarnia@kfupm.edu.sa

- Born in SabtAlAlyia, Saudi Arabia on July 26, 1986

- Received Bachelor of Engineering in Electrical Engineering from King Fahd University of Petroleum and Minerals, Dhahran 31261, Saudi Arabia in 2010

- Joined King Fahd University of Petroleum and Minerals as a Graduate Assistance in 2010

- Completed Master of Science (M.Sc.) in Electrical Engineering in May 2014